Electronic Properties in Nanowire-based Complex Oxide Devices

by

Yuhe Tang

B.S., Wuhan University, 2014

M.S., University of Pittsburgh, 2015

Submitted to the Graduate Faculty of

the Dietrich School of Arts and Sciences in partial fulfillment

of the requirements for the degree of

Doctor of Philosophy

University of Pittsburgh

2021

UNIVERSITY OF PITTSBURGH

DIETRICH SCHOOL OF ARTS AND SCIENCES

This dissertation was presented

by

Yuhe Tang

It was defended on

April 14, 2021

and approved by

Dr. Jeremy Levy, Department of Physics and Astronomy, University of Pittsburgh

Dr. Hrvoje Petek, Department of Physics and Astronomy, University of Pittsburgh

Dr. Roger Mong, Department of Physics and Astronomy, University of Pittsburgh

Dr. Tao Han, Department of Physics and Astronomy, University of Pittsburgh

Dr. Paul Leu, Department of Industrial Engineering, University of Pittsburgh

Dissertation Director: Dr. Jeremy Levy, Department of Physics and Astronomy, University of Pittsburgh

Copyright © by Yuhe Tang
2021

Electronic Properties in Nanowire-based Complex Oxide Devices

Yuhe Tang, PhD

University of Pittsburgh, 2021

A wide range of novel electronic properties have been observed in nanodevices with a reduced dimension at the $LaAlO_3/SrTiO_3$ interface thanks to c-AFM lithography. In this dissertation, electronic properties at the $LaAlO_3/SrTiO_3$ interface are studied with nanowire-based devices. Frictional drag between coupled nanowires is studied at the high magnetic field and superconducting regimes. In both high magnetic field and superconducting regimes, the drag resistance is insensitive to the separation between nanowires, which suggests the dominant electron-electron interaction is non-Coulombic in nature. The frictional drag in the superconducting regime suggests a reduced dimension in the superconducting nanowire due to the 1D nature of the superconductivity at the $LaAlO_3/SrTiO_3$ interface. Frictional drag involving one electron waveguide is studied and shows a correlation with the subband structure of the electron waveguide when the electron waveguide is used as the drag wire. We discuss possible directions for the frictional drag with electron waveguides. Thermal transport experiments can provide additional insights into electronic properties at the interface. We measure the thermopower in the electron waveguide which exhibits quantized ballistic transport and the Pascal liquid phase. The thermopower can be described by the Mott relation and exhibits a different temperature dependence when the electron waveguide is at a conductance plateau. Our thermopower experiment paves the way for quantized thermal transport studies of emergent electron liquid phases in which transport is governed by quasiparticles with charges that are integer multiples or fractions of an electron.

Table of Contents

List of Tables

List of Figures

Preface

This thesis is a summary of my Ph.D. work. It would not be possible without the support and help from many people.

First, I would like to thank my research advisor, Jeremy Levy, for his support and mentorship. His passion for science and research inspires me in many ways. He is always thinking actively about the research and constantly coming up with great ideas for experiments. His high standards and guidance help me make breakthroughs in my research and life. Besides research, I am grateful that he emphasizes the importance of communication and presentation, gives us advice, and creates opportunities for us to practice public speaking and networking skills.

Next, I would like to thank Michelle Tomczyk for her assistance. The first experiment can be challenging due to the high volume of work involved. She trained me to use the dilution refrigerator, plan the experiment, and perform data analysis down to every detail.

I want to thank all my labmates for the shared good times and frustrations during my graduate study and research. In particular, Patrick Irvin, Guanglei Chen, Mengchen Huang, Anthony Tylan-Tyler, Megan Briggemann, Arthur Li, Lucy Chen, Qing Guo, Yun-Yi Pai, Dengyu Yang, Aditi Nethwewala, Muqing Yu, Xinyi Wu, Erin Sheridan, as well as the new batch of students.

My experiments can not be done without samples. I want to thank Prof. Chang-Beom Eom's research group for providing us with high-quality samples. I also want to thank my dissertation committee members, Hrvoje Petek, Roger Mong, Tao Han, and Paul Leu, for their guidance and feedback. Their questions and suggestions help me a lot.

Finally, I want to thank all my friends and family for their unconditional love, support, and encouragement. These guide me through difficulties during my Ph.D. journey.

1.0 Introduction

The invention of silicon-based semiconductor technology has lead to one of the most exciting revolutions in human history. As technology develops, the requirement for materials with novel physical properties shows up, where silicon-based technology reaches the fundamental limit. This calls for the new generation of material platforms. One of the most promising material systems is the complex oxide due to its wide variety of physical properties. Engineering the composition and atom arrangement of the complex oxide can give rise to diverse emerging phases such as high-temperature superconductivity, ferroelectricity, and ferromagnetism.

Additional dimensional confinement can bring more exotic phases to the complex oxide system. Since the discovery of 2D electron gas at the interface between $LaAlO_3$ and $SrTiO_3$, a lot of interesting properties have been discovered in the system such as metal-insulator transition [149], superconductivity [124, 21], magnetism [17, 113], and spin–orbit coupling [135, 20]. This makes the complex oxide, in particular the $LaAlO_3/SrTiO_3$ heterostructure, an emerging research field. Not restricted to 2D physics, 1D physics can also be studied thanks to the advancement of the technology to control metal-insulator transition with a nanometer-scale resolution at the $LaAlO_3/SrTiO_3$ interface. Novel electronic properties have been observed in devices with a reduced dimension and experimental results suggest a lot of physical phenomena in the system may have a 1D nature. Therefore, it is important to study 1D electronic properties in $LaAlO_3/SrTiO_3$ heterostructures, which can help to understand the emergent physical properties in the system and lead to better control of the interface with more advanced functionalities.

In this dissertation, electronic properties at the $LaAlO_3/SrTiO_3$ interface are studied with nanowire-based devices. The dissertation is organized as follows: Chapter 1 reviews the material system and knowledge essential to the research. Chapter 2 introduces major experimental techniques used in experiments. Chapters 3 to 5 present frictional drag experiments performed with various nanowire-based devices in the high-magnetic field regime (Chapter 3), superconducting regime (Chapter 4), and with electron waveguides (Chapter 5).

Chapter 6 presents the thermopower experiment in the electron waveguide at $LaAlO_3/SrTiO_3$ systems.

1.1 $LaAlO_3/SrTiO_3$ Heterostructures

1.1.1 Properties of $SrTiO_3$

Properties of $LaAlO_3/SrTiO_3$ heterostructures inherit largely from the substrate $SrTiO_3$. $SrTiO_3$ has a perovskite crystal structure [41]. It is cubic at room temperature with a lattice parameter of $a = 3.905$ Å. As shown in Figure 1 (a), eight Sr atoms are located at the vertices of the cube and six O atoms sit at the center of each face of the cube. Sr and O atoms form an octahedral cage. At the center of the cage, there is a Ti atom. This cubic structure is most energetically favorable at high temperatures.

As the temperature decreases, $SrTiO_3$ undergoes symmetry-breaking structural transitions. At $T = 105$ K, the cubic structure undergoes an anti-ferrodistortive transition, where the oxygen octahedra rotate in opposite directions (Figure 1 (b)). As a result, the cubic structure changes to a tetragonal lattice structure [41], where two of the lattice vectors contract and the third one is elongated along the axis of the rotation. Domains with different tetragonal orientations (x-, y- or z-axis) of the tetragonal unit cells can form [19] in the bulk $SrTiO_3$ and between these domains ferroelastic domain walls are created (Figure 1 (b)). Domain structures vary between different samples. And even in the same sample, these domains form a different pattern after temperature cycling [72, 19]. Previously the significance of these ferroelastic domain structures has been neglected. However, recent researches have found that these domains and domain walls could be associated with spatially inhomogeneous transport properties [72, 61, 112, 108] and shift the critical temperature for superconductivity [108] of $SrTiO_3$ and $SrTiO_3$ based heterostructures. Domains can be controlled and moved by gating [7, 96]. This may be due to dielectric and elastic moduli differences between domains of different orientations [129], leading to anisotropic electrostriction [34]. Domain walls are found to be more conducting than domains [47]. They may be charged, polarized

[61, 164, 134], and coupled to the ferroelectric [155] or magnetic degree of freedom [107]. One natural coupling mechanism between electrons at the interface and domain structures is that the interfacial lattice distortion is correlated with the carrier density [64, 159, 130]. For a conducting interface, while the in-plane lattice constant is constrained by the substrate, the out-of-plane lattice constant is not, which results in a distortion along the z-axis.

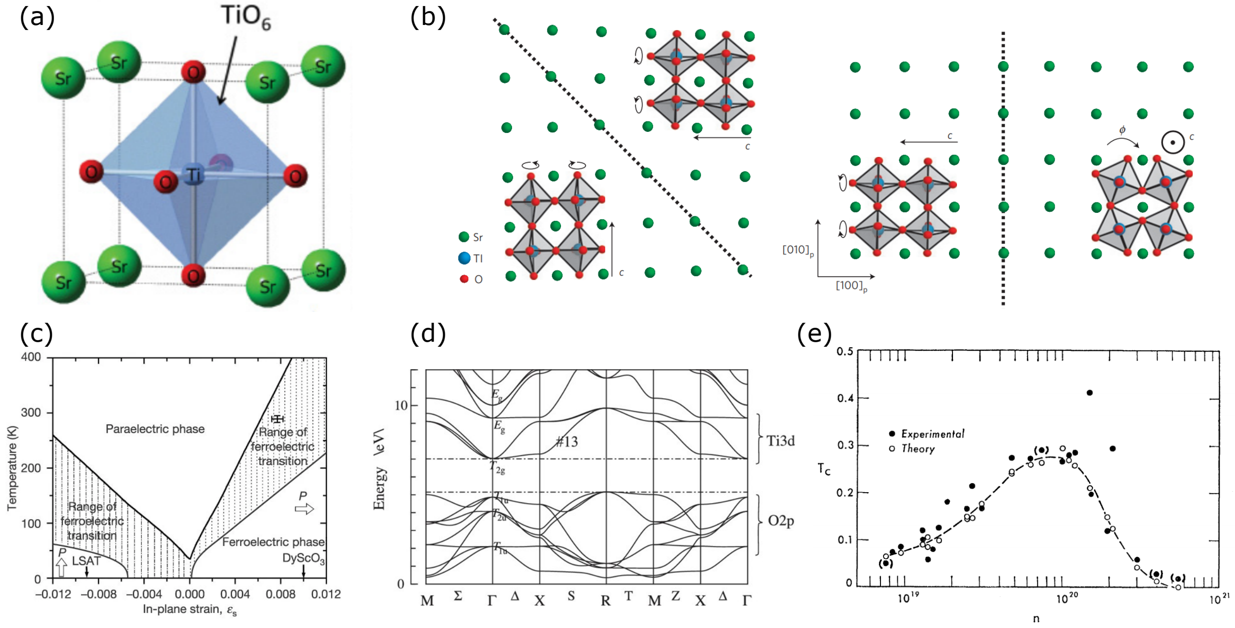

Figure 1: $SrTiO_3$ properties. (a) Perovskite crystal structure of $SrTiO_3$ at room temperature. Adapted from [41]. (b) Below 105 K, $SrTiO_3$ goes through cubic-to-tetragonal phase transition where nearby oxygen octahedra rotate in opposite directions. Different rotation axes lead to different domains, between which structural domain walls show up. Adapted from [72]. (c) $SrTiO_3$ starts a paraelectric to ferroelectric transition below 38 K. It never reaches a ferroelectric state due to quantum fluctuations unless the in-plane strain is applied. Adapted from [56]. (d) Density function theory calculation of cubic $SrTiO_3$'s band structure. Adapted from [137]. (e) The superconducting critical temperature T_c as a function of carrier density shows a dome-shape similar to high-T_c superconductors. Adapted from [79].

At $T < 38$ K, a second transition to the ferroelectric state shows up in $SrTiO_3$ [100] (Figure 1 (c)). However, it never reaches the ferroelectric state and remains paraelectric at low temperatures because of quantum fluctuations. The static dielectric constant for $SrTiO_3$ is $\epsilon \approx 300$ at room temperature. But because of the incipient ferroelectric behavior of $SrTiO_3$ at low temperatures, ϵ increases to around 20000 and stabilizes at $T < 4$ K in the quantum paraelectric regime [100, 128, 129]. Due to the large dielectric constant, $SrTiO_3$ is a good substrate candidate for samples requiring backgating. The ferroelectric state in $SrTiO_3$ can be reached by controlling experimental conditions such as electric field [59] and strain [56].

Understanding the electronic structure of $SrTiO_3$ is important for understanding the physical phenomena observed in $SrTiO_3$ and related complex oxide heterostructures. $SrTiO_3$ is a band insulator with an indirect bandgap of 3.25 eV and a direct bandgap of 3.75 eV [156] according to valence electron-energy loss spectroscopy (VEELS) [156]. Figure 1 (d) shows density function theory calculation of the band structure of cubic $SrTiO_3$. The main contribution of the valence band comes from O $2p$ orbitals and that of the conduction band comes mainly from Ti $3d$ orbitals [137, 156]. The five-fold degeneracy of $3d$ orbitals of Ti atoms is lifted by surrounding O atoms, resulting in a high-energy doublet (e_g states) and a low-energy triplet (t_{2g} states) [94]. t_{2g} band further splits into d_{xy}, d_{yz} and d_{xz} orbitals. Three orbitals are degenerate at the conduction band minimum Γ [137]. The indirect bandgap corresponds to excitation from R to Γ and the direct bandgap corresponds to excitation from Γ to Γ [156]. Other factors such as stress, strain, or dimensional confinement can further modify the band structure [77, 1, 24]. For example, t_{2g} bands are expected to further split due to the anti-ferrodistortive transition and spin-orbit coupling [58, 99].

In 1964, superconductivity was discovered in $SrTiO_3$ by Schooley at $T_c \sim 300$ mK [133], which makes it the first complex oxide to be superconducting. The superconductivity shows up at a carrier density as low as 10^{17} cm^{-3} [90]. This suggests it has a small Fermi surface. The critical magnetic field B_c is around 0.2 T [133] and the critical temperature T_c is around 300 mK [90]. According to the previous electrical transport experiment, T_c as a function of carrier density has a dome-shape phase diagram peaked at $T_c \sim 450$ mK [79], which is similar to other unconventional superconductors (Figure 1 (e)). The unconventional superconductivity in $SrTiO_3$ is hard to be explained by the conventional Bardeen-Cooper-Schrieffer (BCS) theory [6, 49]. In 1969, Eagles proposed that superconductivity in low-density Zr-doped $SrTiO_3$ may be explained by Bose-Einstein Condensation (BEC) of strongly paired electrons [39], in contrast to BCS theory where electrons are weakly coupled to each other and the electron pair size is much larger than the inter-electron separation. This theory predicts a novel electronic phase where at temperatures above T_c, even though electrons are not condensed into a superconducting state, they remain bonded due to strong electron-electron attraction. The existence of a robust electronic phase where electrons pair without forming superconductivity is demonstrated by transport experiments with nanowire-based single-electron transistors at the $LaAlO_3/SrTiO_3$ interface [28]. However, after more than 50 years, the mechanism of $SrTiO_3$'s superconductivity is still an open question that requires more investigation to understand its nature and pairing mechanism.

1.1.2 Emergent properties at the $LaAlO_3/SrTiO_3$ interface

The most well-known $SrTiO_3$-based complex oxide heterostructure is the $LaAlO_3/SrTiO_3$ system [111] (Figure 2 (a)). $LaAlO_3$ also has a perovskite crystal structure with a lattice constant of 3.789 Å. Since it is closely lattice-matched to $SrTiO_3$, it allows a clean epitaxial heterostructure growth. Both $LaAlO_3$ and $SrTiO_3$ are band insulators. But when $LaAlO_3$ is deposited on top of (001) TiO_2 terminated $SrTiO_3$ with a thickness larger than 4 unit cells (Figure 3 (a)), the interface between $LaAlO_3$ and $SrTiO_3$ can become conducting [149]. The typical carrier density for this conducting interface is $\sim 5 \times 10^{13}$ cm^{-2} and the mobility is at the order of 10 $cm^2/(Vs)$ at room temperature [111, 135]. Enhanced mobility larger than 10^4 $cm^2/(Vs)$ has been reported in systems with reduced dimensions at low temperatures [67].

The origin of the conducting 2D interface is still not fully understood. The most widely cited explanation is the polar catastrophe [101]. $LaAlO_3$ consists of alternating layers of LaO^+ and AlO_2^- with alternating charges of +1 and −1. Thus it is polar. $SrTiO_3$ consists of alternating layers of SrO and TiO_2 layers with both layers neutral. Thus it is nonpolar. This polar discontinuity leads to a built-in electric field and the electric field results in a diverging potential as the thickness of $LaAlO_3$ increases (Figure 2 (b) top panel). To avoid the diverging potential, so-called "polar catastrophe", the system undergoes electronic reconstruction, transferring 1/2 electrons from the surface to the interface per 2D unit cell so that the electric

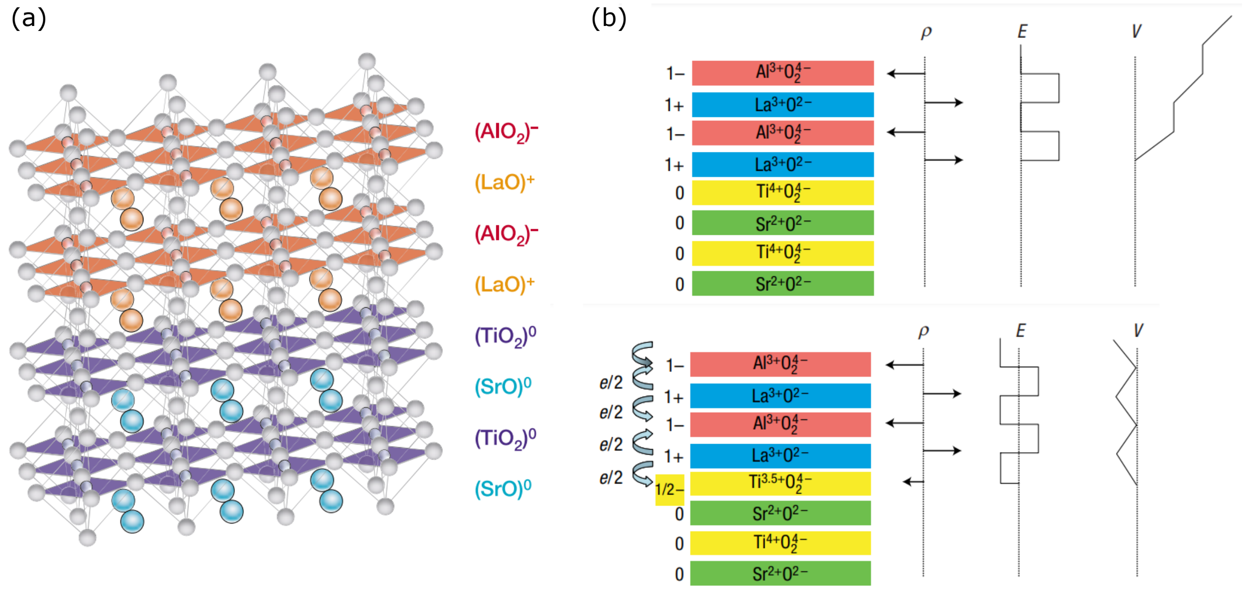

Figure 2: $LaAlO_3/SrTiO_3$ lattice structure and polar catastrophe mechanism. (a) Schematic of the $LaAlO_3/SrTiO_3$ heterostructure showing the composition and the ionic charge state of each layer. Adapted from [111]. (b) The polar catastrophe model for conducting $LaAlO_3/SrTiO_3$ interfaces. Top panel: $LaAlO_3$ has alternating net charges in LaO and AlO_2 layers, which leads to a non-negative electric field and an electric potential that diverges with thickness. Bottom panel: The divergence of the electric potential can be avoided if half an electron is transferred from the surface to the interface, which causes the electric field to oscillate around zero and the potential remains finite. This produces a conducting 2D interface. Adapted from [101].

field oscillates around zero and the potential remains finite (Figure 2 (b) bottom panel). This electronic reconstruction creates a 2D electron system (2DES) at the interface between $LaAlO_3$ and $SrTiO_3$. While polar catastrophe theory successfully explains the formation of 2DES at the interface and $LaAlO_3$'s critical thickness, the carrier density (3×10^{14} cm^{-2}) at the interface according to the theory fails to match the experimentally measured value. The experimentally measured result is an order of magnitude smaller [135, 20]. Other mechanisms such as oxygen vacancies [71] and cation intermixing [161] have also been proposed to explain the formation of a 2D electron gas. But until now, the mechanism of the 2D conducting interface remains an open question.

As discussed above, the conductivity of the interface can be tuned with $LaAlO_3$ thickness. It is found that when the thickness of $LaAlO_3$ is just below the critical value, the interface becomes electrically tunable [149]. By applying a +100 V back gate voltage to $SrTiO_3$ substrate, the interface undergoes a metal-insulator transition and becomes conducting (Figure 3 (b)). The interface stays conducting after the voltage is removed. Later by applying a −100 V back gate voltage, the interface restores an insulating state. This cycle can be performed multiple times without degradation of the system. Inspired by this phenomenon, instead of using a back gate to globally tune the conducting interface, a conductive atomic force microscope (c-AFM) lithography technique [22, 25] is developed where a conductive AFM tip acts as a top gate to change the conductivity state at the interface with a nanometer precision. This technique will be discussed in Chapter 2.

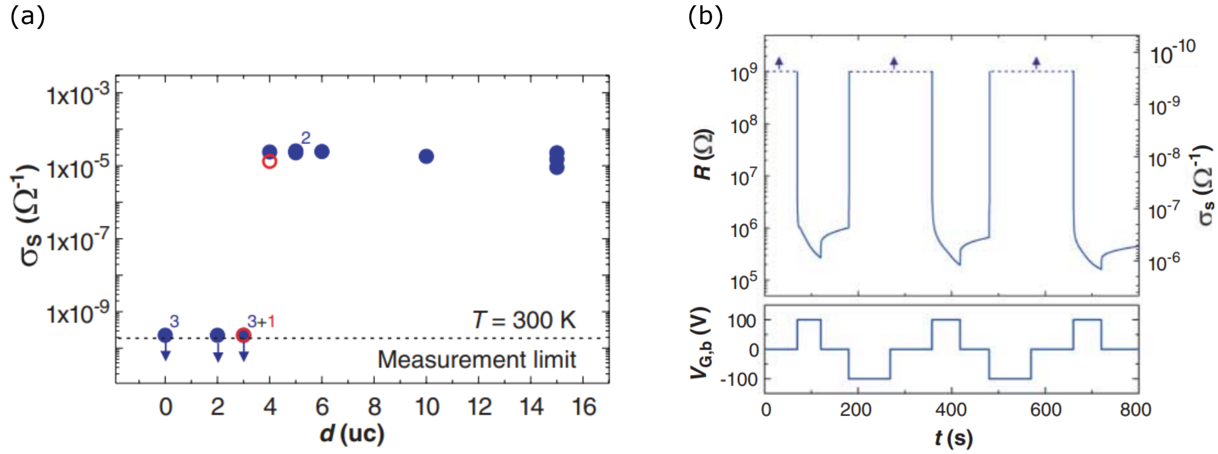

Figure 3: Metal-insulator transition at the $LaAlO_3/SrTiO_3$ interface. (a) Sheet conductance as a function of the number of $LaAlO_3$ unit cells. Adapted from [149]. (b) Sheet resistance (top panel) and the corresponding applied back gate voltage (bottom panel) as a function of time show the metal-insulator transition can be reversibly tuned by an electric field. Adapted from [149].

Apart from the metal-insulator transition, other interesting properties have also been observed at the $LaAlO_3/SrTiO_3$ interface such as ferromagnetism [17, 10, 9, 131], Rashba spin-orbit coupling [20, 135] and superconductivity [124, 21, 125]. The superconductivity at the $LaAlO_3/SrTiO_3$ interface largely inherits from $SrTiO_3$. It shows a T_c around 200 mK and a dome-shaped phase diagram similar to high-T_c superconductors. Transport at the $LaAlO_3/SrTiO_3$ interface is found to be highly inhomogeneous. According to low-temperature scanning-probe measurements, the inhomogeneous transport is affected by ferroelastic domain structures [72, 61]. Domain walls between ferroelastic domains with different orientations are highly conductive [72], and the superconductivity at the interface is 1D in nature situated at domain walls [112]. The thermoelectric effect is studied at the $LaAlO_3/SrTiO_3$ interface to understand the electronic properties. Due to the confinement of 2DES at the interface, an enhanced thermopower is observed, which is attributed to the electron-phonon coupling. These properties make the $LaAlO_3/SrTiO_3$ interface rich in physics.

1.1.3 $LaAlO_3/SrTiO_3$ nanostructures

Electron properties at the interface can be studied with the transport experiment. Transport experiments are performed with various nanostructures fabricated at $LaAlO_3/SrTiO_3$ interfaces. There are different methods to fabricate devices and these methods bring additional dimension confinement to electrons at the $LaAlO_3/SrTiO_3$ interface. Taking advantage of $LaAlO_3$ thickness dependence of the interface metal-insulator transition, conventional photo- or electron-beam lithography can be used to define structures (Figure 4 (a)) [132, 145]. Conducting channels with a typical dimension of 1 μm can be created by UV lithography. Electron-beam lithography can make conducting channels a few hundred nanometers wide [132, 145]. Ion beam irradiation technique (Figure 4 (b)) can further narrow down conducting structures to 50 nm [114]. These techniques are usually used with a resist such as PMMA or amorphous $LaAlO_3$ as an additive or subtractive lithography step and can cause irreversible damage to the material. One way to overcome these is to use c-AFM lithography (Figure 4 (c)). Using the reversible metal-insulator transition when $LaAlO_3$ is at the critical thickness, c-AFM lithography can create nanowires with a width as small as 2 nm [22, 23]. It is fast and straightforward in terms of device fabrication parameters exploration. Experimenting with

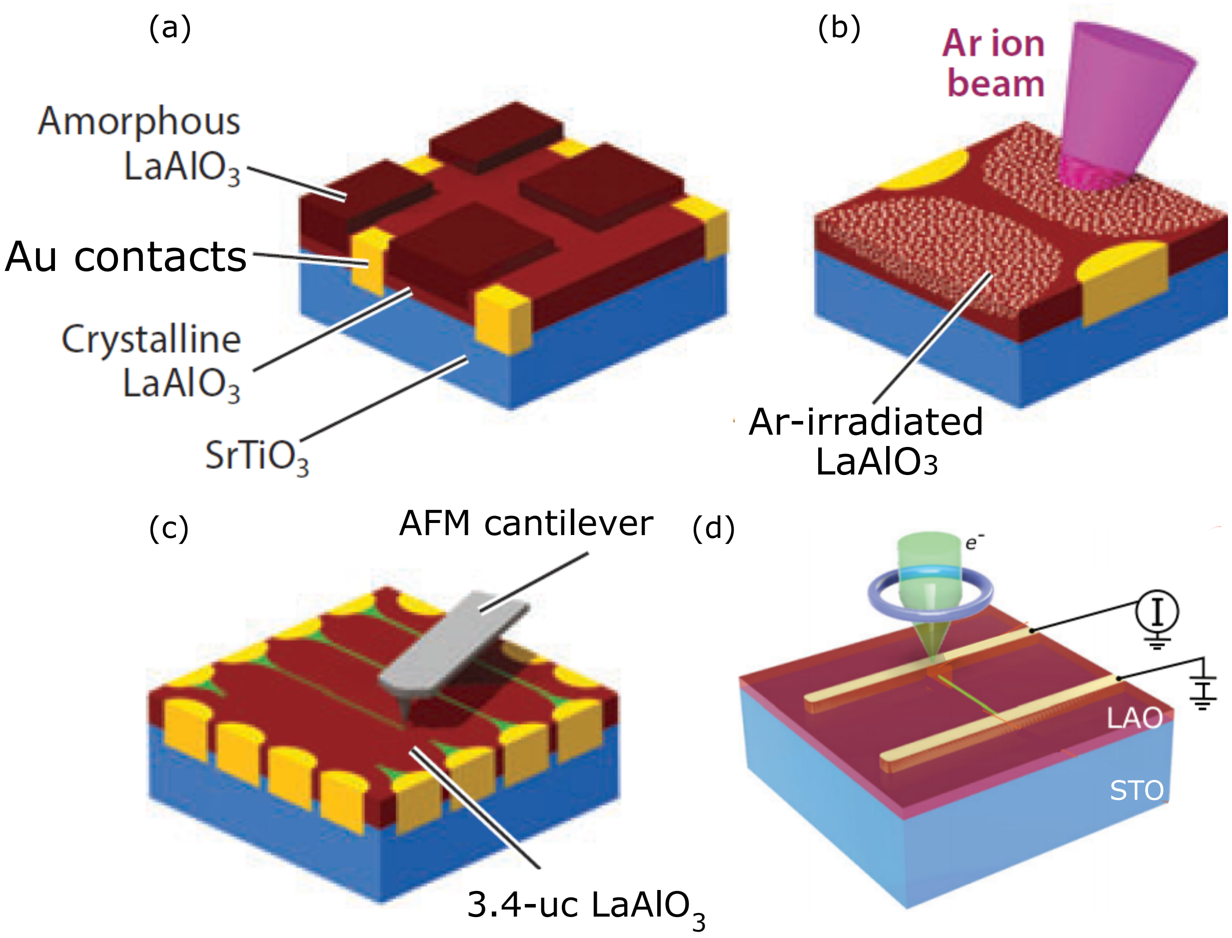

Figure 4: Nanostructure fabrication at the $LaAlO_3/SrTiO_3$ interface. (a) Conventional UV or e-beam lithography technique. The 2 unit cells thick crystalline $LaAlO_3$ region covered by amorphous $LaAlO_3$ is insulating. The uncovered region with a thickness greater than 3 unit cells are conducting. Adapted from [146] (b) Argon ion beam irradiation. Argon ions can transform the conducting $LaAlO_3/SrTiO_3$ interface to an insulating state. Adapted from [146] (c) C-AFM lithography which creates devices with a biased conductive AFM tip. Adapted from [146] (d) ULV-EBL technique which works without resists and provides a ~ 10 nm resolution on a large scale. Adapted from [163]

a new set of parameters typically only takes ~ 5 minutes and involves removing the former device and creating a new one by applying negative and positive voltages. Since the sample does not degrade during this process, the parameter exploration cycle can be repeated multiple times. Varying device design, tip moving speed, and tip voltages, even more complex nanostructures such as single-electron transistors [28, 29], electron waveguides [1, 16] and artificial 1D or 2D superlattices can be created. Another method is the ultra-low-voltage electron-beam lithography (ULV-EBL) technique (Figure 4 (d)) [163]. This technique works without resists and can rapidly create devices on a large scale with a spatial resolution of $\sim$ 10 nm. It is non-destructive to the sample and the conducting state at the interface is reversible through the prolonged exposure to air.

Experiments in nanostructures at $LaAlO_3/SrTiO_3$ interfaces have been fruitful and provide lots of important insights into the system's electronic properties. A single-electron transistor (SET) (Figure 5 (a)) is a powerful probe of mesoscopic physics. By performing experiments on SET, a new electronic phase has been discovered where electrons remain paired outside of the superconducting regime (Figure 5 (b)) [28]. Later on, the transition from diamonds to loops in differential conductance of SET is observed. This is explained by a gate-tunable transition from a pair tunneling regime to a single-electron tunneling regime where the electron-electron interaction in the system changes from being attractive to repulsive (Figure 5 (c)) [29].

One-dimensional wire is the most fundamental nanostructure. It has evolved from regular nanowires dominated by scattering [157, 145] to electron waveguides where quantized conductance in steps of e^2/h can be observed [1, 16]. The nanowire is found to be superconducting with a slightly lower critical temperature. It has a broader transition and non-zero residual resistance [157]. The non-zero residual resistance may come from local hot spots and thermally activated phase slips. Another study of the critical current value as a function of the nanowire's width (Figure 5 (g)) suggests the 1D nature of superconductivity at $LaAlO_3/SrTiO_3$ interfaces. The critical current value is independent of the nanowire's width, which indicates the superconductivity is situated at the boundary between the conducting nanowire and nearby insulating area [112].

Dimensional confinement in the transverse direction of a nanowire can increase the energy spacing between subbands. When the elastic mean-free path is much larger than the nanowire's length and width, the transport through the nanowire is considered ballistic.

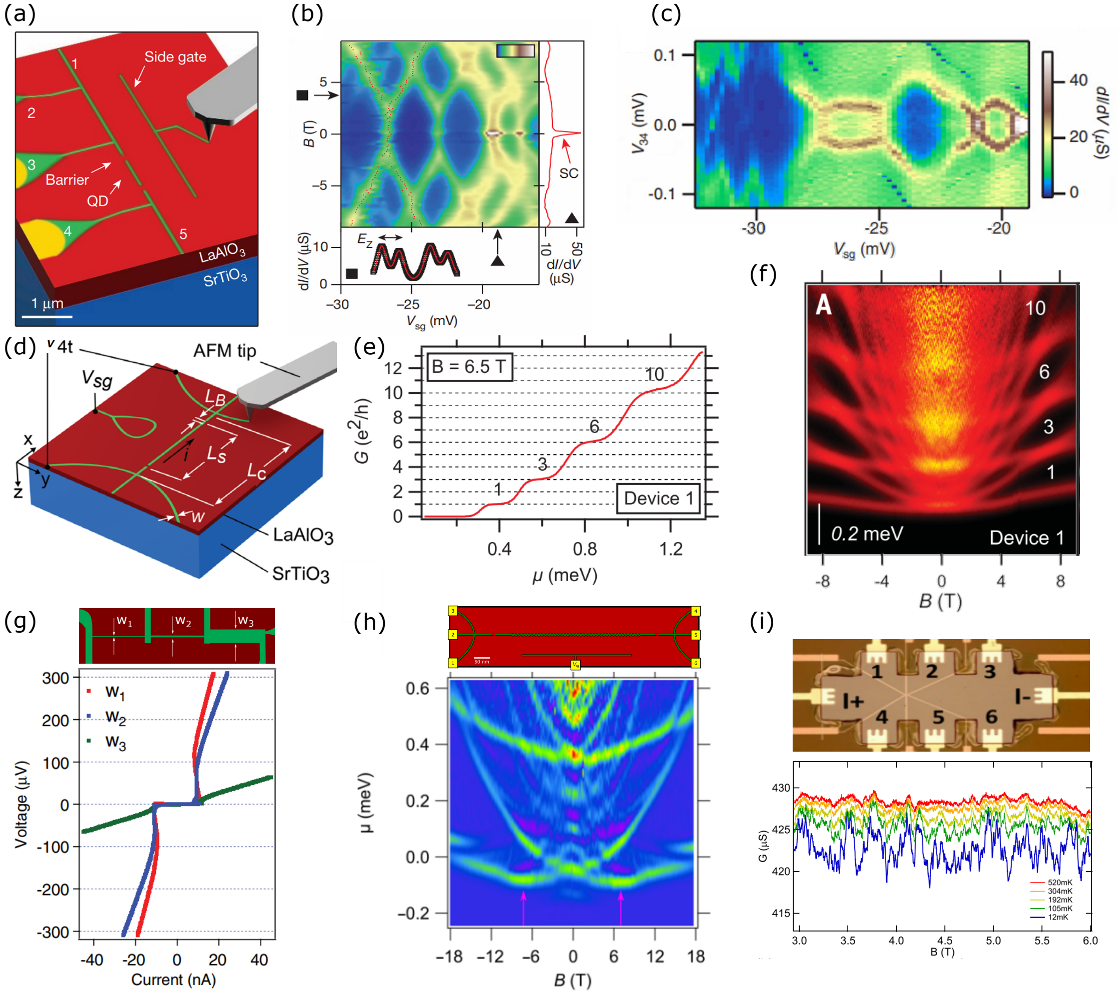

Figure 5: Nanostructures at the $LaAlO_3/SrTiO_3$ interface. (a) Single-electron transistor. (b) Electrons pair without forming superconductivity. Adapted from [28]. (c) Tunable electron-electron interactions. Adapted from [29] (d) Electron waveguide. (e) Pascal liquid phase exhibits quantized conductance plateaus at (1, 3, 6, 10 ...)$\cdot$ e^2/h. Adapted from [16] (f) The transconductance of an electron waveguide. Adapted from [16] (g) IV properties of superconducting $LaAlO_3/SrTiO_3$ nanowires with different widths. Adapted from [112] (h) The transconductance of an electron waveguide with spatial modulation. Adapted from [15] (i) Universal conductance fluctuation measured from a $LaAlO_3/SrTiO_3$ Hall bar structure. Adapted from [144]

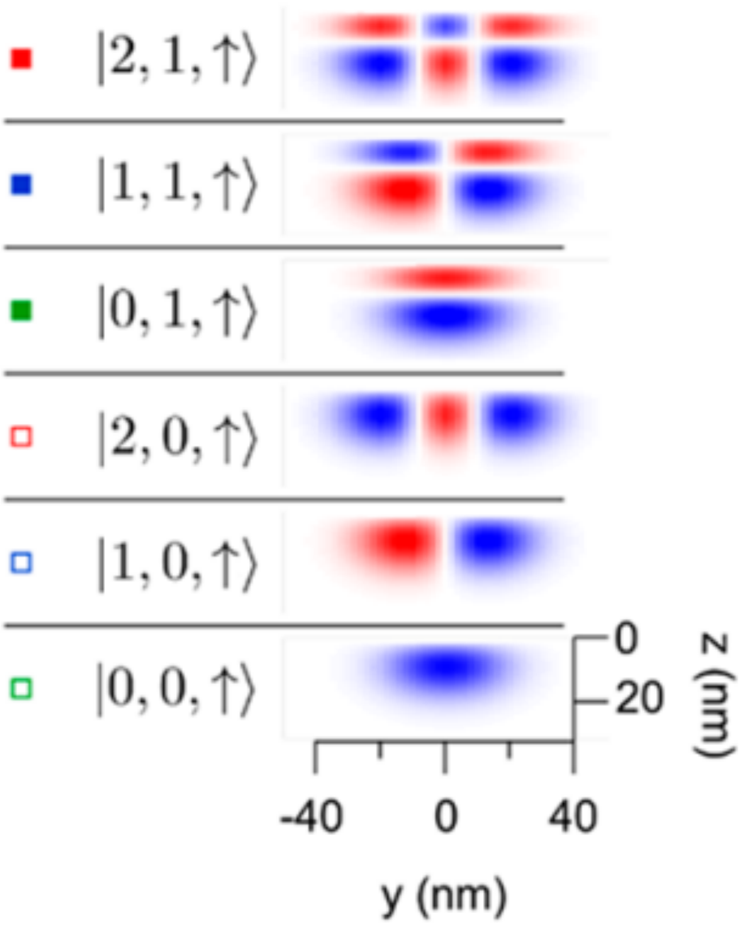

Figure 6: Spatial modes of the electron waveguide. The electron waveguide is along the x-direction with y and z being the transverse directions. Adapted from [1]

This is realized in the electron waveguide, which can be fabricated by bracketing a regular nanowire with two highly transparent tunnel barriers (Figure 5 (d)). The conductance in the electron waveguide shows quantized plateaus at the integer values of e^2/h as expected from the ballistic transport (Figure 5 (e)). The band structure is revealed by taking the derivative of the conductance with the chemical potential (Figure 5 (f)) and can be described by the lateral and vertical spatial quantum numbers analogous to the electromagnetic wave in a regular electromagnetic waveguide (Figure 6). The electron waveguide as long as 1 μm has been successfully fabricated and the band structure suggests an attractive electron-electron interaction [1] within the electron waveguide. A novel Pascal liquid phase has been discovered in electron waveguides where conductance follows a characteristic sequence within Pascal's triangle: (1, 3, 6, 10, 15 ...) e^2/h (Figure 5 (e)). This suggests the existence of bound states with more than 2 electrons [16].

Other more complex nanostructures have also been fabricated at $LaAlO_3/SrTiO_3$ interfaces. Through voltage or spatial modulation in electron waveguide fabrication, more exotic features appear in the original band structure, which may be attributed to the engineering of spin-orbit coupling at $LaAlO_3/SrTiO_3$ interfaces (Figure 5 (h)) [14, 15]. Nanocross, the cross-shaped electron waveguide, exhibits inhomogeneities in the electronic band structure of the four arms [106]. This inhomogeneity suggests the ferroelastic domain structure of $SrTiO_3$ can reproducibly affect the transport property of $LaAlO_3/SrTiO_3$ interfaces. Hall bar is a powerful platform for transport experiments. Universal conductance fluctuation (UCF) phenomenon is observed in the Hall bar structure (Figure 5 (i)) which suggests the phase-coherent transport at $LaAlO_3/SrTiO_3$ interface [123, 144]. Non-local transport is reported in the Hall bar structure [158, 30]. Although the origin of non-local transport is not well understood, it may arise from spin-dependent excitations. Graphene can be placed on top of $LaAlO_3/SrTiO_3$ interfaces. The charge neutrality point of graphene can be reversibly controlled with proximal $LaAlO_3/SrTiO_3$ nanostructures created by c-AFM lithography. This effect can be used to create reconfigurable edge states in graphene. [89].

1.2 Frictional Drag

Coulomb drag, or more generally frictional drag, is first proposed by Pogrebinskii [116] which involves two closely spaced but electrically isolated conductors. Driving current through one conductor (drive conductor), a voltage or current can be induced in the other conductor (drag conductor) depending on whether it forms an open or closed circuit (Figure 7). It is a more direct way to study electronic interactions since without interactions, charge carriers in different conductors are insensitive to each other and frictional drag does not exist. Frictional drag can typically be understood as scattering between charge carriers in different conductors. The scattering, accompanied by momentum or energy transfer between charge carriers in different conductors, depends on the nature of charge carriers, interlayer electronic interactions, and the microscopic structure of the electronic system. Therefore, frictional drag is a powerful technique to study electronic properties of interacting many-body systems.

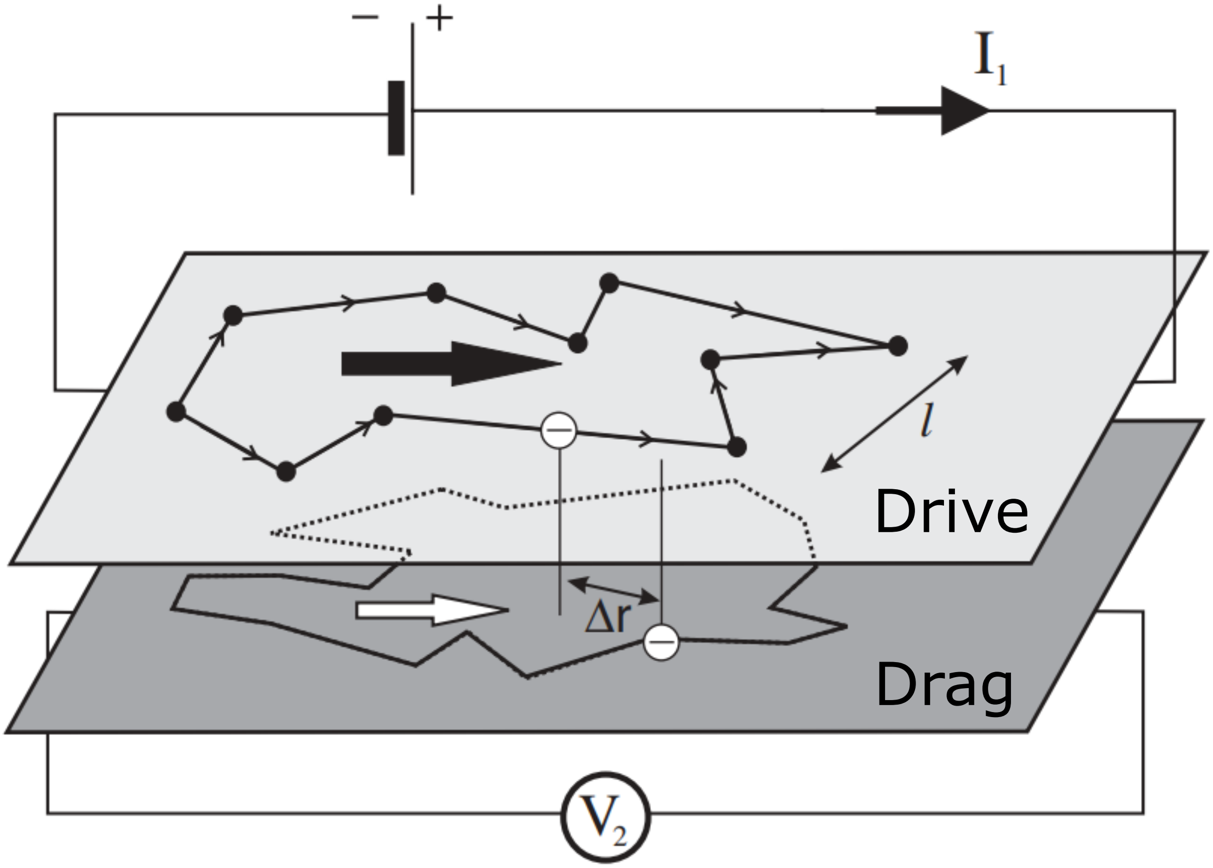

Figure 7: The schematic of frictional drag. Current is driven in the top drive conductor and the induced voltage is measured from the bottom drag conductor. Adapted from [119]

1.2.1 2D frictional drag

A lot of earlier works on frictional drag were done on semiconductor 2D electronic systems. The transport in each layer can be captured by generic Boltzmann equation:

$$\frac{\partial f_i}{\partial t} + v_i \nabla f_i + (eE_i + \frac{e}{c}[v_i \times B])\frac{\partial f_i}{\partial p} = -\frac{\delta f_i}{\tau} + I_{ij} \tag{1}$$

where f_i is the distribution function in each layer, τ stands for the transport impurity scattering time [80, 68], I_{ij} is the collision integral due to interlayer Coulomb interaction and δf_i is the non-equilibrium correction to the distribution in each layer. Consider the degenerate electron systems [50] and use the standard perturbative calculation [68, 80, 13]. Suppose E_1 is the electric field in the drive layer and j_2 is the induced current in the drag layer. j_2 is defined by:

$$j_2 = e \sum v \delta f_2 \tag{2}$$

The coefficient between j_{2x} and E_{1x} defines the drag conductivity σ_D. Therefore the drag coefficient ρ_D is given by

$$\rho_D = \frac{\sigma_D}{\sigma_1 \sigma_2 - \sigma_D^2} \approx \frac{\sigma_D}{\sigma_1 \sigma_2} \tag{3}$$

where σ_i is the longitudinal conductivity in layer i. The latter approximation comes from the smallness of the effect:

$$\sigma_D \ll \sigma_i \tag{4}$$

The phenomenological drag rate [104, 68] is given by:

$$\tau_D^{-1} = \frac{m_1}{16\pi e^2 \tau^2 n_2 T} \int_{-\infty}^{\infty} \frac{d\omega}{\sinh^2[\omega/2T]} \times \int \frac{d^2 q}{(2\pi)^2} |D_{12}(\omega, q)|^2 \Gamma_1(\omega, q) \Gamma_2(\omega, q) \tag{5}$$

$\Gamma_1(\omega, q)$ is the non-linear susceptibility that relates an AC voltage to a DC current it induces. It is also known as the rectification function. The rectification function demonstrates the importance of the electron-hole asymmetry in the drag effect. In a typical electron gas system, there are electron-like and hole-like excitations depending on whether the energy of electrons is larger or smaller than the Fermi energy. Without electron-hole asymmetry, the drive layer displays a zero total momentum. Therefore no momentum can be transferred to the drag layer. Similarly, momentum is transferred equally to electrons and holes in the drag layer and the drag layer requires the electron-hole asymmetry to display a non-zero net current. The electron-hole asymmetry is characterized by the band curvature in conventional semiconductors [73] and $\partial\sigma/\partial\mu$ in the Fermi liquid theory [103, 102] where σ and μ are the conductivity and chemical potential in each layer. The above physics picture can also be applied to the frictional drag between charge carriers with opposite signs. One instance is the frictional drag between coupled graphene layers where the electric current is carried by electrons in one layer and holes in the other layer. The frictional drag due to the electron-hole asymmetry is described by the leading-order perturbation theory where the scattering process involves the momentum transfer from the drive layer to the drag layer. However, it is not universal. Other higher-order processes can also contribute which are less sensitive to the electron-hole asymmetry.

Earlier 2D frictional drag focus on measuring the strength of interactions between separate layers in semiconductor devices such as p-doped GaAs quantum wells [63, 62], coupled 2D-3D or 2D-2D electron systems in AlGaAs/GaAs quantum wells [140, 139, 50, 51, 53, 40] and electron-hole bilayers [138]. The temperature or separation dependences have been studied and results suggest the frictional drag can be attributed to the momentum transfer due to Coulomb coupling between two layers (Figure 8 (a)). Other mechanisms also contribute. For example, the frictional drag at large separations between two layers is attributed to phonon-mediated interactions [52, 110, 127]. The enhancement or the sign change of frictional drag at lower temperatures is attributed to the plasmon [60, 109] or thermoelectric effects [139].

On graphene-based systems, more exotic frictional drag phenomena have been observed which depends both on the interaction between graphene layers and electronic states in each layer [75, 48, 76, 151, 54]. The electrical tunability and the advent of graphene-boron-nitride heterostructures [151, 117] make graphene more flexible and powerful for frictional drag researches compared to semiconductor systems. When $B = 0$ T and the chemical potential is away from the charge neutrality point, the frictional drag is consistent with the behavior expected for Fermi liquid regime [48, 87, 76]. The carrier density in each layer can be independently tuned which allows studying electron-electron, electron-hole, and hole-hole interactions (Figure 8 (b)). Drag signals of electron-electron or hole-hole and electron-hole have opposite signs as expected. Surprisingly, when both layers are near the charge neutrality

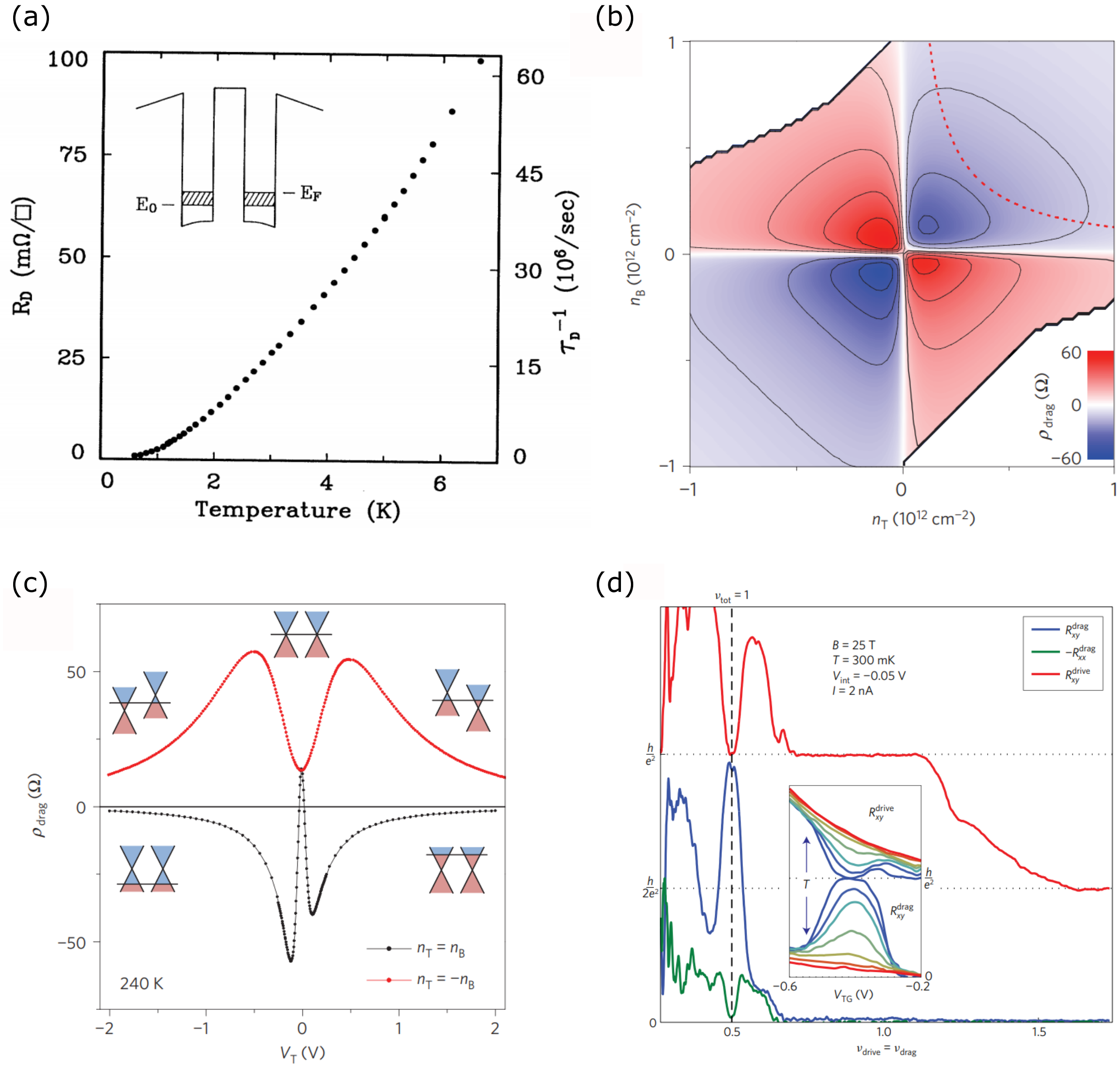

Figure 8: 2D frictional drag. (a) Frictional drag as a function of temperature in GaAs/AlGaAs double quantum well systems. Adapted from [50] (b) Graphene frictional drag in Fermi liquid regime as a function of carrier densities in two graphene layers. (c) Graphene frictional drag shows a non-zero value at the charge neutrality point. Adapted from [48] (d) Quantum Hall frictional drag. Adapted from [93]

point [48, 151, 87, 84], an enhanced non-zero frictional drag is observed which is sensitive to the magnetic field (Figure 8 (c)). This phenomenon is proposed to have an energy transfer or thermoelectric origin [142, 84, 141, 143]. Analogous to the Hall measurement, Hall drag [92, 93, 143, 91] where drag voltage is perpendicular to the drive current is also studied (Figure 8 (d)). Quantum Hall drag has been observed in coupled graphene layers. The result suggests a new correlated state where coupled graphene layers form an interlayer exciton condensate [93, 91].

Frictional drag has also been performed between normal metals and superconducting films [46, 65]. A drag signal is observed only in the vicinity of the superconducting-normal transition of the superconducting film. The phenomenon is explained by the local electric field fluctuation induced by mobile vortices [136] or the supercurrent drag effect due to Coulomb coupling [73, 37].

1.2.2 1D frictional drag

1D frictional drag attracts a lot of interest since electrons confined in 1D are expected to show strong electronic correlations. A purely 1D electronic system is known as a Luttinger liquid [152, 95, 57] and shows different behaviors compared to a Fermi liquid. Confined in 1D, the elementary excitations of Luttinger liquids are charge and spin density waves. Charge and spin density waves propagate independently from each other, which is known as spin-charge separation [4, 69]. Most theories of 1D frictional drag study the interaction between Luttinger liquids under circumstances of different temperatures [78, 118, 121, 42, 36], quantum wire lengths [78], electron densities [44], separations [78, 122, 36], and scattering mechanisms between quantum wires [43, 105, 42, 55]. It is predicted that below a crossover temperature T^*, electrons in two infinitely long quantum wires of equal carrier densities form a zigzag-ordered interlocked charge density wave. This results in an exponentially increasing drag resistivity with decreasing temperatures [78, 44]. The drag resistance is predicted to be exponentially suppressed when the separation increases [78] or there is an electron density mismatch between nanowires [44]. For shorter nanowires, the charge density wave in one nanowire may slip relative to the charge density wave in the other nanowire, resulting in a finite but exponentially large value as the temperature decreases [78].

Experimentally, 1D frictional drag has mostly been conducted on semiconductor systems with either horizontal [148, 147, 162, 33] or vertical geometry [82, 81], as shown in Figure 9 (a) and (b), respectively. The negative drag phenomenon where electrons flow in opposite directions in the drive and drag nanowire is observed and explained by Wigner crystallization (Figure 9 (c)) [162]. Experiments performed with coupled ballistic quantum wires show drag resistance peaks concomitant with the opening of 1D subbands [81, 32]. The phenomenon can be understood as the effect of an enhanced electron-hole asymmetry as the Fermi level in the nanowire approaches the subband bottom (Figure 9 (d)). The geometry where two nanowires are vertically integrated can reduce the interwire separation. When both nanowires are occupied by less than one subbands, the temperature dependence of frictional drag shows an upturn below a crossover temperature. The phenomenon is interpreted as the Luttinger liquid effect although it is hard to compare experimental results and theory quantitatively (Figure 9 (e)) [82].

Frictional drag has also been studied between $LaAlO_3/SrTiO_3$ nanowires. The result suggests the dominating coupling mechanism is non-Coulombic in nature since the drag resistance is independent of the interwire separation [148]. Besides, frictional drag between superconducting $LaAlO_3/SrTiO_3$ nanowires also implies the 1D nature of superconductivity at the $LaAlO_3/SrTiO_3$ interface [147]. These will be discussed in detail in Chapters 3 and 4.

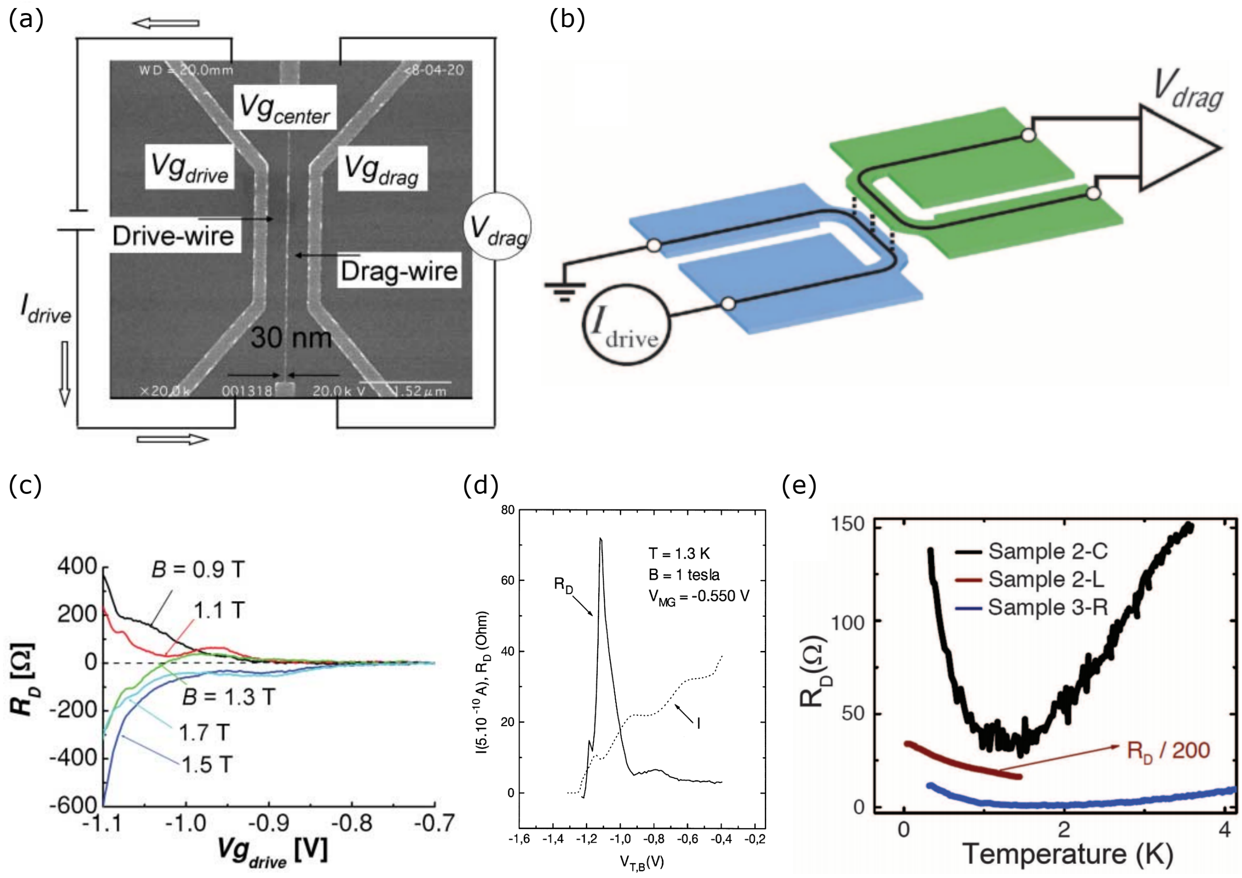

Figure 9: 1D frictional drag in semiconductor systems. (a) Typical horizontal frictional drag device geometry. Adapted from [162] (b) Typical vertical geometry. Adapted from [82] (c) Negative drag resistance suggests the Wigner crystallization in the nanowire. Adapted from [162] (d) Peaks in drag resistance are concomitant with the opening of 1D subbands. Adapted from [32] (e) The upturn in the temperature dependence of frictional drag is consistent with the Luttinger liquid model. Adapted from [82]

2.0 Experimental Techniques

2.1 $LaAlO_3/SrTiO_3$ Sample Preparation

2.1.1 Sample growth

The $LaAlO_3/SrTiO_3$ samples used in the experiment are grown with pulsed laser deposition (PLD) [160] onto (001) $SrTiO_3$ substrates by our collaborators Jung-Woo Lee and Hyungwoo Lee in Prof. Chang-Beom Eom's research group at the University of Wisconsin-Madison. Single-crystal $SrTiO_3$ (001) substrates with a low miscut ($< 0.1°$) angle are etched by buffered hydrofluoric acid for 60 s to get a TiO_2-terminated surface. To make an atomically smooth surface with single unit cell height steps, substrates are annealed at 1000 °C for 6 hours. A thin (3.4 unit cell) $LaAlO_3$ film is grown epitaxially on top of $SrTiO_3$ by PLD at a growth temperature of 550 °C and background oxygen pressure of 10^{-3} mbar. Then the sample is slowly cooled down to room temperature after the growth finishes. As shown in Figure 10 (a), the thickness of the $LaAlO_3$ film is monitored using reflection high-energy electron diffraction (RHEED) [126]. The RHEED signal intensity oscillates as the material is grown on top of the substrate and each cycle of the oscillation indicates the completion of one unit cell. AFM image of the $LaAlO_3$ surface after growth shows atomically flat terraces (Figure 10 (b)).

2.1.2 Sample processing

After samples are grown by our collaborators and delivered to our lab in Pittsburgh, they are processed by lab member Mengchen Huang to pattern electrical contacts to the $LaAlO_3/SrTiO_3$ interface [86]. As shown in Figure 11 (a), the configuration of electrical contacts is designed so that each 5 mm × 5 mm sample consists of 16 canvases where devices for experiments are created. Each canvas is a 30 μm × 30 μm area surrounded by 16 interface contacts (Figure 11 (c)). Standard photolithography techniques are used to create the canvas. First, the photoresist is spun onto samples (Figure 12 (a)). The thickness of

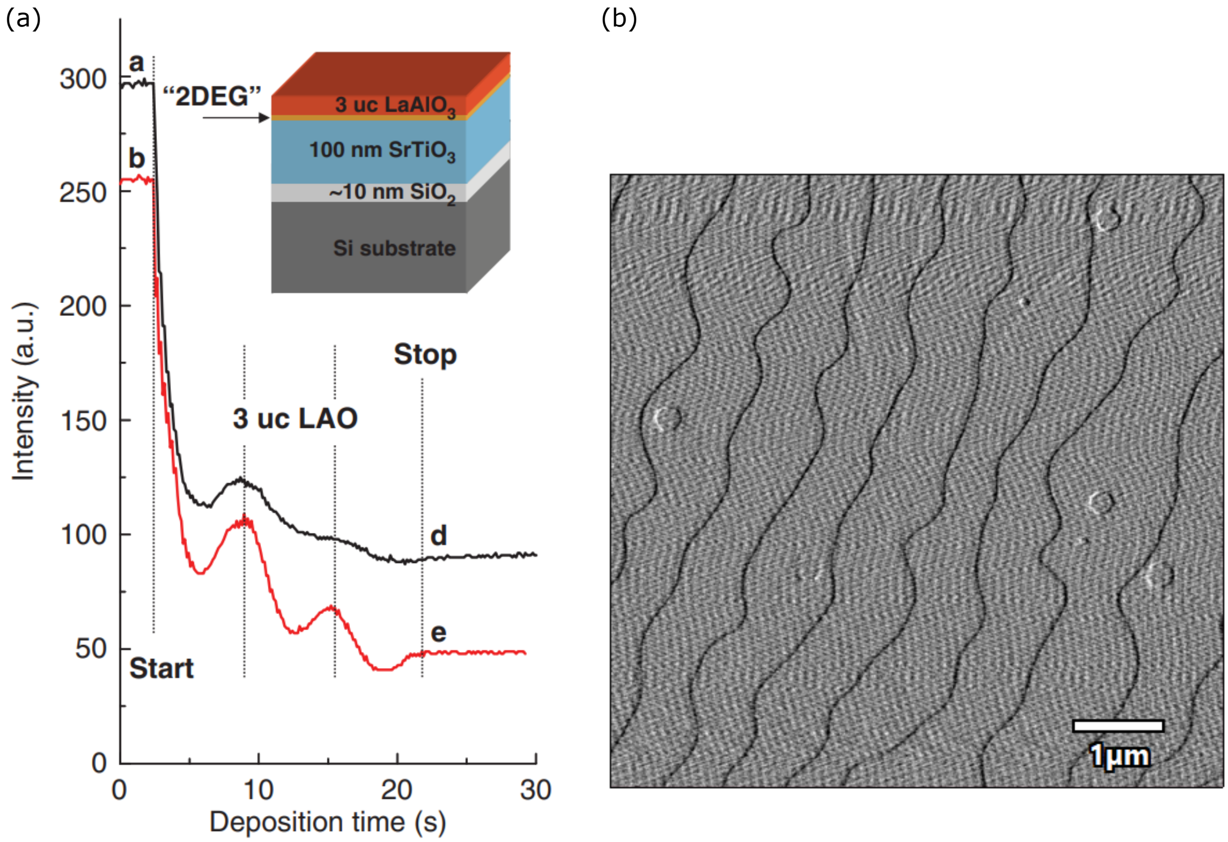

Figure 10: $LaAlO_3/SrTiO_3$ heterostructures growth. (a) RHEED intensity oscillation during the $LaAlO_3$ film growth on top of the $SrTiO_3$ substrate. Each oscillation cycle indicates the completion of one unit cell. Adapted from [115] (b) AFM image of the $LaAlO_3$ surface showing atomically flat terraces.

the photoresist is approximately 2 μm. After the sample is baked at 95 °C for 1 minute, the photoresist is first exposed using a mask aligner (Figure 12 (b)) and then developed for 1 minute (Figure 12 (c)). An Ar^+ ion mill is used to etch the sample area not covered by the photoresist down to the interface (Figure 12 (d)). Next, DC sputtering is performed to make interface electrical contacts. 4 nm Ti serving as an adhesion layer is deposited and then 25 nm Au is deposited on top of the Ti layer so that Au electrically contacts the $LaAlO_3/SrTiO_3$ interface (Figure 12 (e)). The photoresist is removed by the lift-off process afterward (Figure 12 (f)). After the deposition of interface electrodes, the photolithography and sputtering are

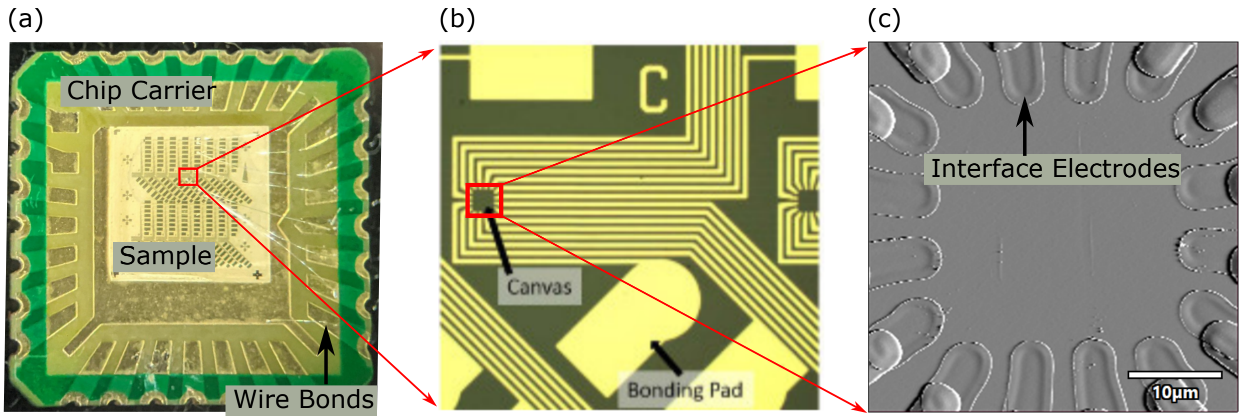

Figure 11: Processed $LaAlO_3/SrTiO_3$ samples. (a) Processed $LaAlO_3/SrTiO_3$ samples with 16 canvases on a chip carrier. Bonding pads leading to interface electrodes are wire bonded to the chip carrier to allow for transport experiments. (b) Zoom-in picture of a canvas surrounded by gold traces from interface electrodes to bonding pads. Adapted from [86] (c) AFM image of a canvas surrounded by 16 interface electrodes.

repeated a second time (Figure 12 (g)) to deposit gold electrical contacts on the $LaAlO_3$ surface, which is used to trace interface contacts to larger bonding pads (Figure 11 (b)). These bonding pads can be wire bonded to the chip carrier holding the sample to make electrical connections between the sample and instruments. Finally, any photoresist residue left on the sample surface is removed by plasma cleaning (Figure 12 (h)).

2.2 C-AFM Lithography

C-AFM lithography [22, 23] is developed in our lab to create nanostructures at interfaces and devices in all of the experiments described here are fabricated by this technique. In contrast to globally tuning the conductivity state at the interface by back gate voltages, c-AFM lithography is able to locally change the conductivity state at the nanometer scale with the help of a conductive AFM tip as a top gate. A positively biased AFM tip in contact with

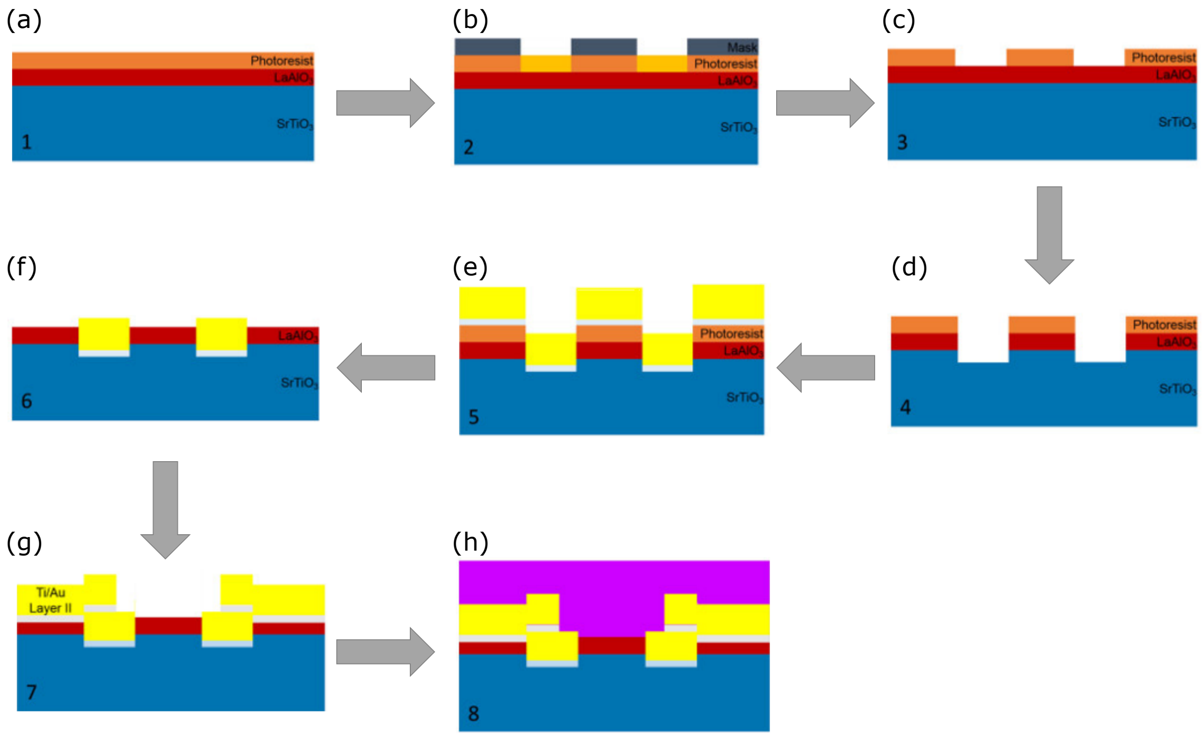

Figure 12: $LaAlO_3/SrTiO_3$ sample processing steps. (a) Spin photoresist on the $LaAlO_3$ surface. (b) The photoresist is exposed using a mask aligner. (c) Develop photoresist. (d) Ion milling to etch the sample down to the interface. (e) DC sputtering to deposit Ti and Au. (f) Lift-off (g) Second layer of Ti and Au is deposited to create gold traces from interface electrodes to bonding pads (h) Plasma cleaning. Adapted from [86]

the $LaAlO_3$ surface locally induces the metal-insulator transition and switches the interface from the insulating to conducting state ("write"). Reversibly, a negatively biased AFM tip switches the interface back to the insulating state ("erase"). In this way, as shown in Figure 13 (a), when a positively biased AFM tip moves between two interface electrodes, it writes a conducting nanowire and the monitored conductance will show a jump once two electrodes are connected through the nanowire (Figure 13 (b)). The nanowire can be erased by moving a negatively biased AFM tip across it (Figure 13 (c)) and the conductance monitored between electrodes will drop. The width of the nanowire at room temperature can be estimated by fitting to the conductance drop profile during the cutting (Figure 13 (d)). The mechanism for the writing/erasing process can be explained by surface protonation/deprotonation [18, 8] which will be discussed in detail later. The width of the nanowire depends on the writing voltage and a thinner nanowire can be created with a smaller tip voltage. The typical width of the nanowire is around 10 nm created by commonly used $+10-15$ V tip voltages. The width can be further reduced to $2-3$ nm by using a $+3$ V tip voltage. Combining capabilities to write and erase, c-AFM lithography can create more complicated nanostructures with various functionalities such as field-effect transistors [23], electrical rectifiers [12], single-electron transistors [27], electron waveguides [1, 16], 1D or 2D superlattices [14], and photodetectors [66]. The capability to create various nanostructures is important for studying electronic properties at $LaAlO_3/SrTiO_3$ systems and future applications.

2.2.1 AFM operation

C-AFM lithography relies on the usage of an atomic force microscope (AFM). AFM [11] is a type of scanning probe microscope with a sub-nanometer resolution. It was invented in the early 1980s as a by-product of the scanning tunneling microscope (STM). Different from the optical or electron microscope, AFM uses a mechanical probe to "touch" or "feel" the surface to obtain the topography information. Therefore it does not suffer from the limited spatial resolution because of the diffraction or aberration. AFM can be used for imaging, characterization and manipulation at the nanoscale.

As shown in Figure 14, AFM consists of a cantilever with a sharp tip at its end to scan the sample surface. The tip's radius of curvature is on the order of 10 nm which is necessary to obtain high-resolution topography. The sample is placed on top of a piezo stage. Piezoelectric materials change shapes in response to an applied electric field. The sample is moved by the piezo stage. During the process, the sample surface is raster scanned by the tip and the topography of the sample can be constructed. When the tip gets close to the sample surface, the cantilever bends because of the atomic force between atoms at the end of the tip and atoms on the surface. The deflection of the cantilever can be detected and converted to the height information of the surface topography. The deflection of the cantilever is detected

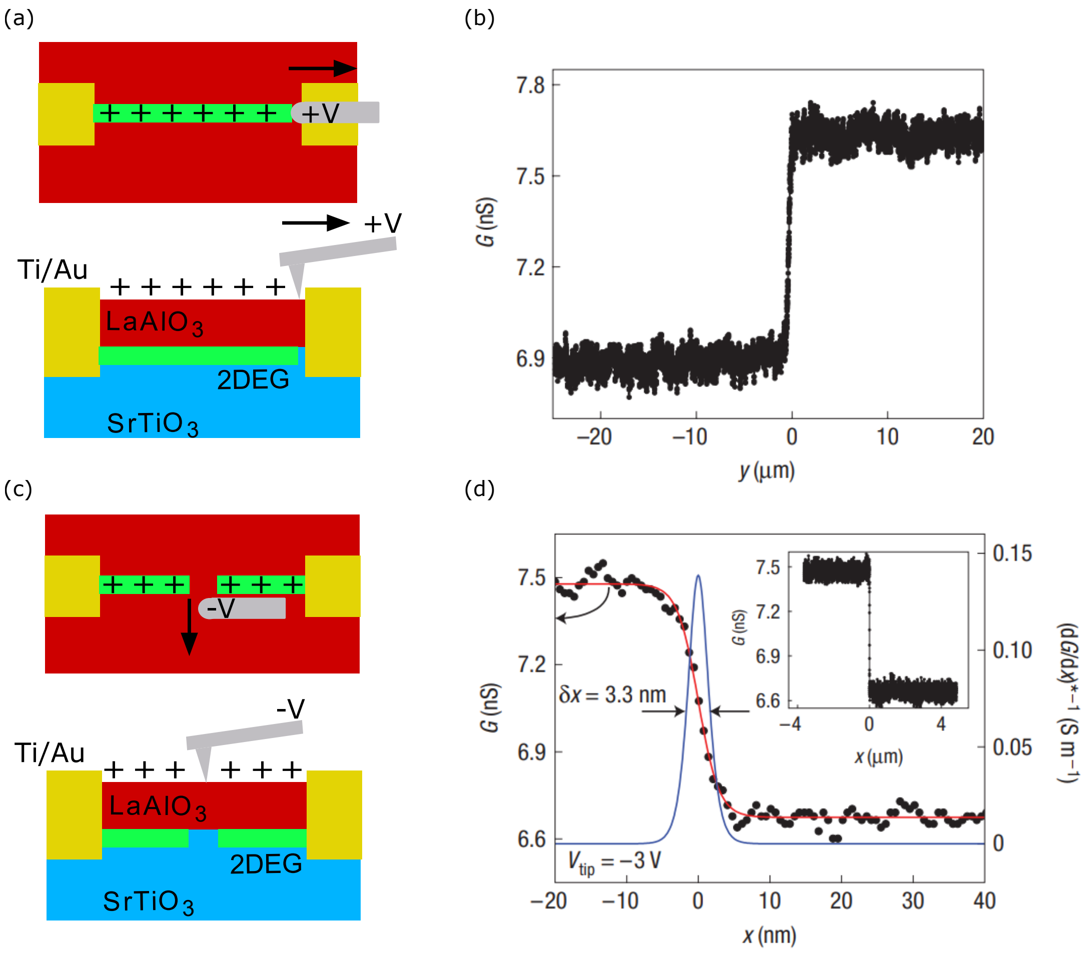

Figure 13: C-AFM lithography. (a) Writing process. As a positively biased AFM tip in contact with the $LaAlO_3$ surface moves between two interface electrodes, it leaves a trace of protons on the path. 2DEG is formed underneath protons and a nanowire is created between two electrodes (b) Conductance is monitored and increases when a nanowire is written between two interface electrodes. Adapted from [22] (c) Erasing process. As a negatively biased AFM tip in contact with the $LaAlO_3$ surface moves across the nanowire, it removes protons and the nanowire is “cut” or “erased” (d) A conductance drop is observed once the wire is cut and the nanowire width can be estimated by fitting to the conductance drop profile. Adapted from [22]

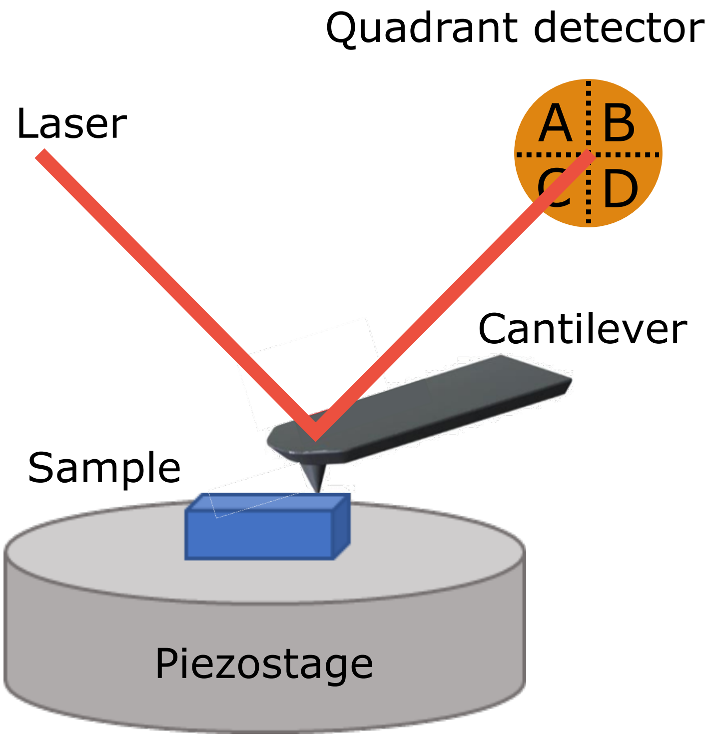

Figure 14: AFM schematic. A sample is placed on top of a piezo stage, which moves the sample so that the tip at the end of the cantilever can scan the sample surface. The laser reflected from the top surface of the cantilever is collected by the quadrant detector, which gives information about the tip's deformation.

by shining a laser onto the cantilever which has a highly-reflective coating. The reflected laser spot is detected by a quadrant photodetector. Intensities of the reflected laser spot on four quadrants of the detector are V_A, V_B, V_C and V_D. Sum value measures how well the light source is aligned on the cantilever:

$$Sum = V_A + V_B + V_C + V_D \tag{6}$$

The vertical bending or deflection of the cantilever is given by:

$$Deflection = (V_A + V_B) - (V_C + V_D) \tag{7}$$

The lateral twisting of the cantilever is given by:

$$Lateral = (V_A + V_C) - (V_B + V_D) \tag{8}$$

Depending on the applications, AFM can operate in three different modes: contact, AC, and non-contact mode.

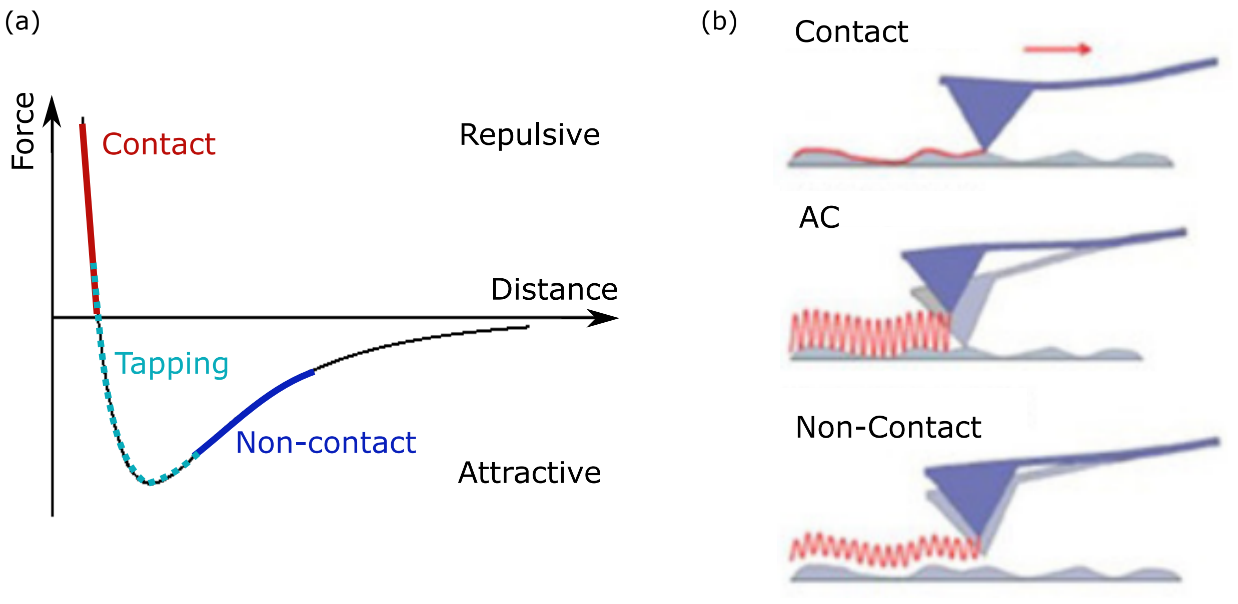

Figure 15: AFM operation modes. (a) The interaction as a function of the distance between the tip and the sample. Corresponding AFM operation modes are shown with different colors along the force curve. As the distance between the tip and the sample becomes smaller, the force changes from the attractive to the repulsive force. (b) Schematic of different AFM operation modes. Top panel: Contact mode. The tip is in contact with the sample surface. Middle panel: AC mode. The tip touches the sample surface intermittently. Bottom panel: Non-contact mode. The tip never touches the surface. Adapted from [3]

2.2.1.1 Contact mode

In contact mode, the tip is in close contact with the sample surface (Figure 15 (b) Top panel) and the atomic force is repulsive (Figure 15 (a)). The interaction between the sample and tip obeys Hooke's Law:

$$F = -k \times D \tag{9}$$

where k is the spring constant of the cantilever and D is the deflection of the tip. As the tip scans over the sample surface with a feedback loop on, D is kept constant by adjusting the height of the cantilever which is controlled by the Z piezo. The sample surface topography image can be constructed as the Z piezo height over the scanned surface area. Since the tip is "dragged" across the sample surface in contact mode, both the tip and the sample can degrade during the contact mode scanning.

2.2.1.2 AC mode

In AC mode, a small piezo in the cantilever holder controls the cantilever to oscillate near or below the resonant frequency. This oscillation results in the oscillation of the deflection signal, which can be demodulated to get the corresponding amplitude and phase. The amplitude of the deflection signal changes when the tip moves over surface features of different heights. Similar to the mechanism described in contact mode, through a feedback loop, Z piezo adjusts the height of the cantilever to keep the amplitude constant at the setpoint value and Z piezo height over the scanned surface area is mapped to obtain the sample surface topography.

Unlike the contact mode where the tip constantly touches the sample surface, it strikes against the sample surface intermittently (Figure 15 (b) middle panel) in AC mode, which helps to reduce frictional forces and causes less damage to both the sample and the tip. In addition to the amplitude of the cantilever's oscillation, the phase signal can be detected as well. This signal channel provides additional information about the sample such as stiffness and adhesion properties which are not visible in surface topography.

2.2.1.3 Non-contact mode

In non-contact mode the tip of the cantilever does not touch the sample surface at all (Figure 15 (b) bottom panel) and the interaction is long-range and attractive (Figure 15 (a)). Therefore neither the tip nor the sample is damaged. The cantilever oscillates at or just above the resonant frequency with a few nanometers amplitude. Either amplitude or frequency modulation can be used to provide the feedback signal for imaging.

2.2.2 Water-cycle mechanism

C-AFM lithography process can be attributed to the "water-cycle" mechanism [18, 8]. $LaAlO_3$ surface absorbs H_2O molecules in the atmosphere, which dissociates into H^+ and OH^- (Figure 16 (a)). During the writing process, the positively biased AFM tip removes some of the OH^- ions, making the surface locally charged with an excess of H^+ ions (Figure 16 (b)). H^+ ions attract electrons to the interface underneath the protonated surface and the $LaAlO_3/SrTiO_3$ interface locally switches from the insulating to conducting state, which is similar to modulation doping [35]. During the erasing process, the negatively biased AFM tip removes extra H^+ ions and the interface switches back to the insulating state (Figure 16 (c)). The "water-cycle" mechanism is supported by the fact that c-AFM lithography is unsuccessful in dry air or vacuum environments. Another evidence is that the conductance of the written structure decays in an ambient environment since H_2O molecules are absorbed onto the $LaAlO_3$ surface continuously and higher humidity can lead to a faster decay rate of the written device. But when placed under a vacuum or in a dry environment, the lifetime of the written device can significantly increase [8]. Typically the humidity level for c-AFM lithography is kept between 30% and 40%.

2.2.3 C-AFM lithography details

The AFM used for device fabrication in experiments described here is an Asylum MFP-3D AFM. The tip in use is a conductive doped silicon tip with a force constant of 3 N/m and tip radius curvature of 8 nm. The AFM contact mode is used for c-AFM lithography with

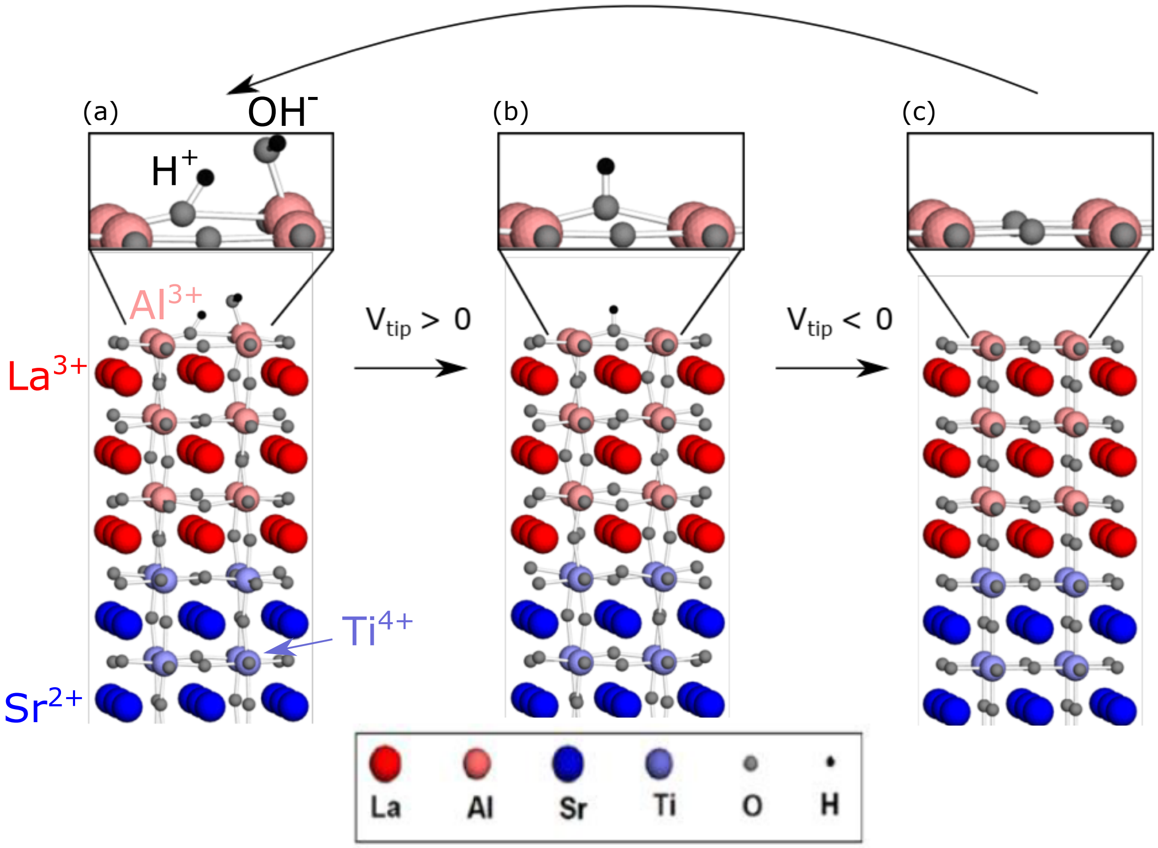

Figure 16: Water-cycle mechanism. (a) H_2O absorbed on $LaAlO_3$ surfaces dissociates into H^+ and OH^-. (b) Writing with a positive tip voltage removes OH^-, leaving an excess of H^+ ions. (c) Erasing with a negative tip voltage removes H^+ and restores ionic balance on the surface.

a 0.1 V deflection setpoint corresponding to a force of 80 nN. To limit the current flowing through the sample, especially when writing over gold electrodes, a 1 GΩ resistor is used for protection purposes. Otherwise, a current that is too large can melt electrodes and damage the canvas. The $LaAlO_3/SrTiO_3$ sample is photosensitive and the interface can become conducting when exposed to light. To avoid random conducting regions at the interface, the writing process should be performed in darkness.

The design of a device is created in Inkscape which is a vector graphics software. The

Inkscape device design file and the scanned AFM image of the canvas are loaded into a homemade LabVIEW lithography program which allows users to set writing parameters such as writing speeds, directions, and writing voltages. The LabVIEW lithography program then communicates with the AFM controller which moves and applies voltages to the conductive AFM tip according to the device design and writing parameters.

During the writing process, the two-terminal and four-terminal conductances of the device can be monitored simultaneously. Electrical contact between interface electrodes and a chip carrier is established through wire bonding and all interface electrodes are either used to measure the voltage, source current through the device, or grounded. Conductance is measured by a standard low frequency (< 15 Hz) lockin-in technique. A 100 mV excitation voltage is applied at the source electrode. Once a nanowire is written between two interface electrodes, a jump of conductance can be observed. The typical two-terminal conductance for a nanowire of ~ 10 μm is between 500 nS and 1 μS and four-terminal resistance is ~ 100 kΩ/μm.

2.2.3.1 Cleaning the canvas

A clean canvas is crucial for device fabrication, especially for the electron waveguide [1, 16] which will be discussed in the later section. The definition of "clean" is not about the surface of the canvas. Instead, since the device exists at the interface between $LaAlO_3/SrTiO_3$, any conducting residues at the interface need to be thoroughly removed. In order to achieve an effective canvas cleaning, it is important to make sure a well-defined electric potential difference is applied between the tip and the interface and the cleaning spacing is smaller than the width of a nanowire which is typically 10 nm. The well-defined potential difference is achieved by making the structure to be erased electrically connected to the interface electrode which is grounded during the c-AFM lithography. This can be done either by writing a conducting area connected to interface electrodes before erasing or using the previously written device which is already connected to interface electrodes.

The canvas cleaning first focuses on a small rectangular area where the device for experiments is going to be written. Since this area is the location for the main device, a fine clean with a slower speed and small spacing is necessary. A -12 V is applied to the AFM tip and the negatively biased AFM tip raster scans the small rectangular area with a line spacing of 2 nm in both horizontal and vertical directions with a speed of 10 μm/s. Next, the AFM tip with the same negative bias raster scans a larger rectangular area extended to interface electrodes in both directions with a larger line spacing of 20 nm and a speed of 40 μm/s. After the cleaning, the conductance between interface electrodes should drop to zero and the old AFM tip will be replaced with a new tip for device writing since the old tip wears out during the canvas cleaning.

2.2.3.2 Frictional drag device writing

Typical canvas and device design are shown in Figure 17 (a). A device consists of virtual electrodes, leads, and the main device. Virtual electrodes are funnel-shaped conducting areas which connect leads and the front of interface electrodes to maintain good electrical connections between them. They are written with around 20 V at a speed of 3 μm/s. Better electrical contact can be achieved by making larger and longer funnels which cover a larger area of the interface electrode or a longer section of leads. Writing funnels multiple times can also make funnels more conducting and electrical contact better. If the above methods do not help, it is likely that the interface electrode makes poor contact with the interface and should be replaced by another one. Leads are essentially nanowires to make electrical contact between the main device and interface electrodes. They are written with around 15 V at a speed of 300 nm/s. Writing leads multiple times can make them more robust and conducting, thus good for electrical contact.

The main device is written after finishing virtual electrodes and leads. The main device for the frictional drag experiment is composed of two parallel nanowires (zoom-in figure in Figure 17 (a)). They are closely spaced but electrically isolated from each other. Each nanowire is contacted with four leads to allow for four-terminal measurements. However, due to the limitation of wiring in the instrument, only one nanowire is connected with four leads while the other one with three leads. Two nanowires are first written with around 15 V at a speed of around 100 nm/s. After this, unwanted conducting channels can form between

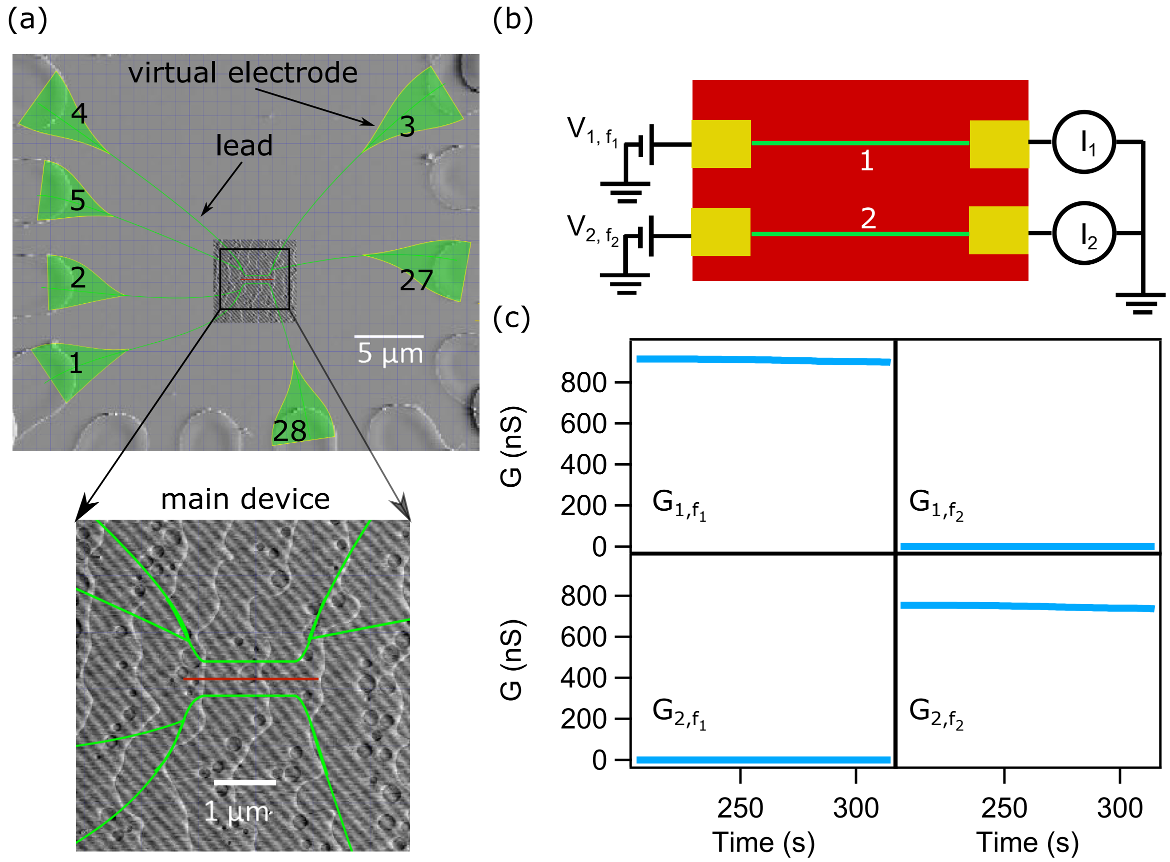

Figure 17: Writing of the frictional drag device. (a) Top: The design of a frictional drag device in Inkscape. The design consists of virtual electrodes, leads and the main device with two parallel nanowires. Bottom: Zoom-in figure of the frictional drag main device. The red line is used to erase between two nanowires to eliminate possible leakage. (b) Conductance monitoring setup during the device writing. For simplicity, only two terminals are shown for each nanowire. Voltages with 100 mV amplitude and frequency f_1 and f_2 are applied on wire 1 and wire 2 to source current, respectively. I_1 and I_2 from wire 1 and wire 2 are measured containing both f_1 and f_2 components (c) Conductance matrix after writing is successful. Diagonal terms are two-terminal conductance for each nanowire and off-diagonal terms are the leakage between nanowires.

two nanowires which cause the leakage. Therefore, it is important to erase between two nanowires to avoid leakage. As shown by the red line in the zoom-in figure of Figure 17 (a), erasing is done along a line in the middle of two nanowires with around -10 V and a speed of around 100 nm/s. The exact parameters for writing nanowires and erasing in between should be adjusted during device fabrication so that after the erasing both nanowires are sufficiently conducting without leakage in between. Generally speaking, a larger magnitude of the tip voltage and lower tip moving speed can make both writing and erasing more effective. But a more effective writing can lead to a higher chance of leakage which is hard to erase and a more effective erasing between nanowires can damage nanowires during erasing. Two methods of increasing success rate are (1) repeating the sequence of writing nanowires and erasing twice or three times (2) making two nanowires further apart so that both writing and erasing processes affect less to nanowires not right underneath the AFM tip. The electron waveguide-regular nanowire frictional drag devices are fabricated in the same way, except one regular nanowire is replaced with an electron waveguide whose fabrication method will be introduced in the next section.

During frictional drag device writing, two-terminal conductance of both nanowires can be monitored at the same time. As shown in Figure 17 (b), two AC voltages with the same amplitude and different frequencies are applied on each nanowire. Voltages applied on wire 1 and wire 2 have a frequency f_1 and f_2 and are defined as V_{1,f_1} and V_{2,f_2}, respectively. The typical amplitude for sourcing voltages is 100 mV. Current I_1 and I_2 are measured from wire 1 and wire 2 containing both f_1 and f_2 components and the current component measured from wire i at frequency j is defined as I_{i,f_j}. Correspondingly, the two-terminal conductance measured from wire i at frequency j can be defined as $G_{i,f_j} = I_{i,f_j}/(100\text{ mV})$ with 100 mV being the typical sourcing voltage amplitude. If we think of 4 two-terminal conductance terms from two wires at two frequencies as a matrix, a successful frictional drag device with two good nanowires and without leakage should show large diagonal terms G_{i,f_i} representing the two-terminal conductance of each nanowire and zero off-diagonal terms G_{i,f_j} representing leakage (Figure 17 (c)).

2.2.3.3 Electron waveguide writing

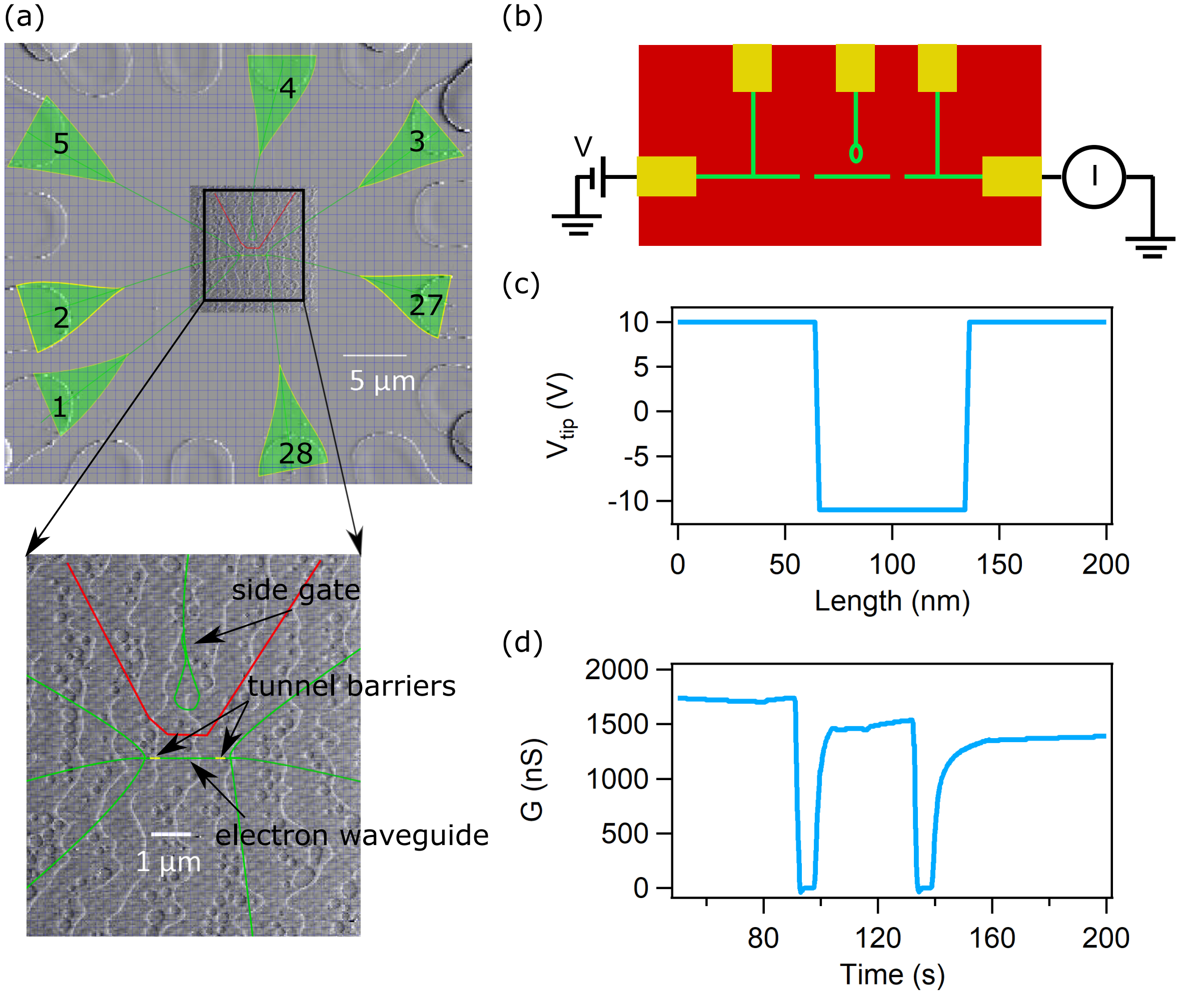

Figure 18: Writing of the electron waveguide. (a) Top: The design of an electron waveguide device in Inkscape. Bottom: Zoom-in figure of the electron waveguide main device. The red line is used to erase and avoid leakage between the waveguide and side gate and yellow lines are used for creating tunnel barriers. (b) Conductance monitoring setup during the device writing. (c) The voltage pulse for creating tunnel barriers. (d) Two-terminal conductance during the writing of an electron waveguide.

One of the major breakthroughs in c-AFM lithography is the capability to write electron waveguides [1, 16] with fully quantized conductance plateaus in steps of e^2/h. Besides virtual electrodes, leads, and the main device, an electron waveguide device also consists of a side gate to tune the chemical potential of the waveguide (Figure 18 (a)). The side gate usually has a loop shape to prevent the electric field between the gate and electron waveguide from being too strong due to sharp structures. The side gate is written with similar parameters as leads. To avoid possible leakage between the gate and the electron waveguide, an erasing around the side gate is performed using a negative tip voltage of ~ -12 V at a speed of 300 nm/s (the red line in Figure 18 (a)). The main device of an electron waveguide is a nanowire bracketed by two highly transparent tunnel barriers. The nanowire is first written with the same parameters as leads which are typically around 18 V for tip voltage and 300 nm/s for tip moving speed. As represented by two short yellow lines in Figure 18 (a), highly transparent barriers are created by retracing the previously written nanowire with $\sim$ 10 V at a speed of 10 nm/s over a distance of $\sim$ 200 nm, during which a negative tip voltage pulse around -11 V is applied over a distance of $\sim$ 60 nm (Figure 18 (c)). The strength of the tunnel barriers can be tuned by changing the speed and magnitudes of positive and negative voltages during the retracing. A larger positive tip voltage magnitude can make tunnel barriers weaker and more transparent. In comparison, a larger negative pulse magnitude, longer negative pulse distance, and slower retracing speed can make tunnel barriers stronger. If tunnel barriers are too weak, the electron waveguide will be highly conducting and similar to a regular nanowire which is hard to pinch off and does not have a quantized conductance (Figure 19 (a)). If tunnel barriers are too strong, the electron waveguide can not survive at low temperatures. If only one single tunnel barriers work with the other one too weak, even though the electron waveguide appears tunable by the side gate, the conductance is not well quantized at all values of magnetic fields (Figure 19 (b)). One candidate explanation is that the observation of quantized conductance requires the side gate to tune the chemical potential of the nanowire region between tunnel barriers. However, when only one tunnel barrier works, the side gate tunes the chemical potential of the nanowire and the connected lead together, which is highly conducting and the conductance is outside of the quantized regime.

Two-terminal conductance is monitored during the writing to determine the quality of highly transparent tunnel barriers and whether the electron waveguide is ready (Figure 18 (c)). Figure 18 (d) shows the change of two-terminal conductance when tunnel barriers are

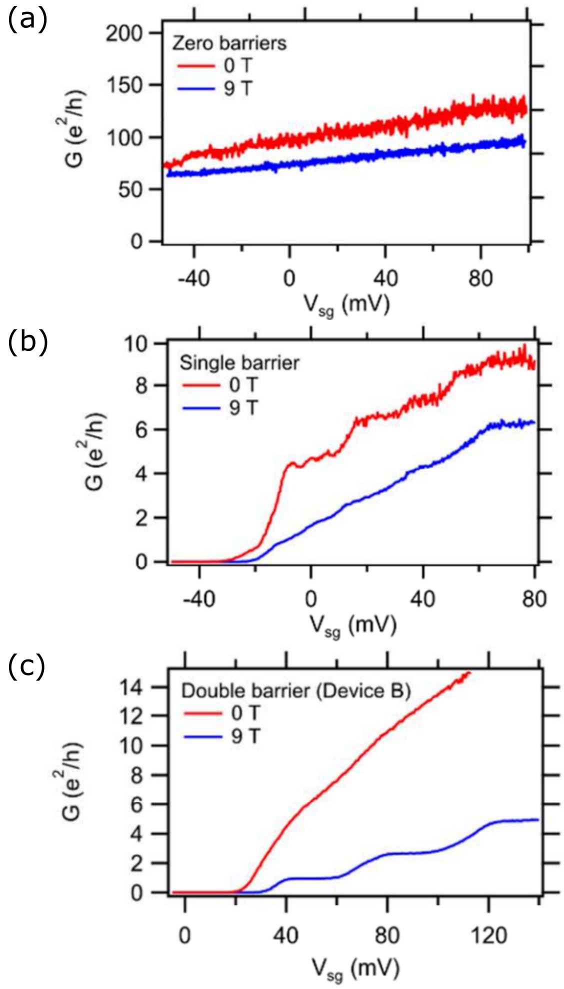

Figure 19: Electron waveguide device with zero, one, and two barriers. Quantized conductance is only observed in devices with two transparent tunnel barriers. When no tunnel barrier is present, the device is highly conducting and hard to be tuned to an insulating state. When one tunnel barrier is present, although the device can be tuned by the side gate, the conductance is not well quantized. Adapted from Supporting Information in [1]

being created. Typically for a good electron waveguide, when creating the barrier with a negative voltage pulse, the conductance will drop to zero. Within ~ 1 s after the negative voltage pulse is withdrawn, the conductance increases back to a value comparable but smaller than the value before the negative voltage pulse is applied. After both barriers are created, the final two-terminal conductance usually is still larger than half of the original value.

2.3 Low Temperature Transport Measurement

2.3.1 Physical property measurement system

After the device fabrication is completed with c-AFM lithography, the sample is transferred to a cryostat, placed under vacuum, and cooled down to perform low-temperature transport experiments. A Quantum Design dilution refrigerator integrated into Quantum Design Physical Property Measurement System (PPMS) is used to achieve a base temperature of 50 mK. The PPMS provides a flexible and automated workstation which controls the temperature and magnetic field during the experiment. The field can be applied up to ±9 T and PPMS alone can reach a temperature as cold as 1.8 K, which is necessary for the dilution refrigerator to reach 50 mK. Figure 20 (a) and (b) are schematics of the sample probe and dewar of PPMS. The sample probe surrounded by a superconducting magnet is at the innermost part of the PPMS dewar. Both the sample probe and magnet are submerged in the liquid helium bath in PPMS dewar. The vacuum, liquid nitrogen jacket, and superinsulation layers are used to reduce the helium boil-off rate and preserve the helium. The base temperature of 1.8 K is achieved by pumping on the liquid helium bath through the sample probe.

2.3.2 Dilution refrigerator

In the atmosphere, the boiling temperature of helium is 4 K. By pumping on it, the temperature can be reduced to 1.8 K, which is the base temperature for PPMS. A Quantum Design dilution refrigerator (DR) insert is used (Figure 22 (b)) to achieve millikelvin base temperature. A DR uses a mixture of 33% ^{3}He and 66% ^{4}He to cool to 50 mK. As shown in Figure 21, when the temperature is cooled down to below $\sim$ 870 mK, the mixture is separated into two phases. The heavier dilute phase consists mostly of ^{4}He with around 6% ^{3}He and

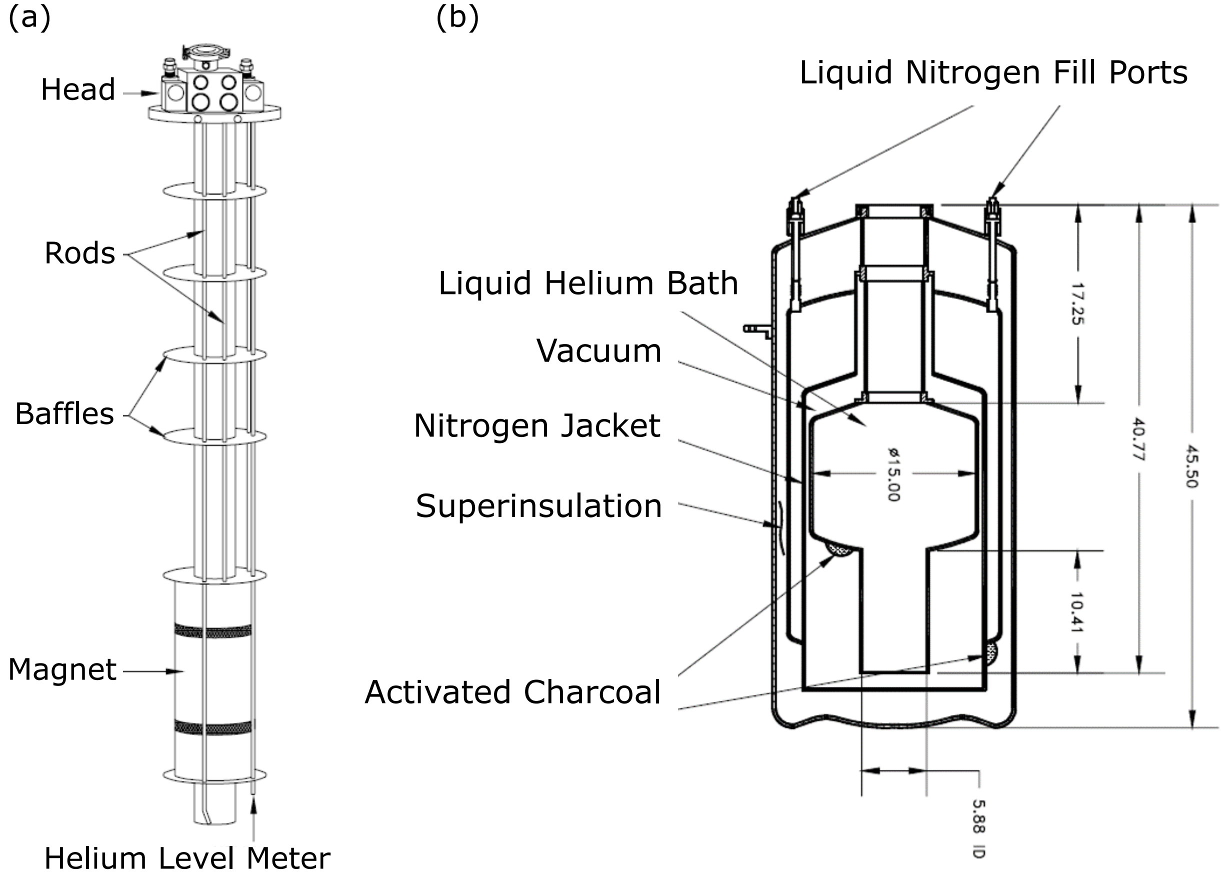

Figure 20: Schematic of PPMS. (a) Sample probe and magnet (b) PPMS dewar. Sample probe in (a) is inserted into the PPMS dewar with the magnet submerged in the liquid helium bath (adapted from PPMS manual)

the lighter concentrated phase is almost pure ^{3}He. Since the dilute phase is heavier than the concentrated phase, the concentrated phase is on top of the dilute phase. The enthalpy of ^{3}He in the dilute phase is larger than the enthalpy of ^{3}He in the concentrated phase. Using this property, it is possible to achieve cooling by migrating ^{3}He from the concentrated phase into the dilute phase. The working principle of a dilution refrigerator is shown in Figure 22 (a). The DR uses a turbopump backed up by a diaphragm pump to circulate the ^{3}He-^{4}He mixture in the mixing chamber (Figure 22 (a)). The dilute phase extends from the bottom

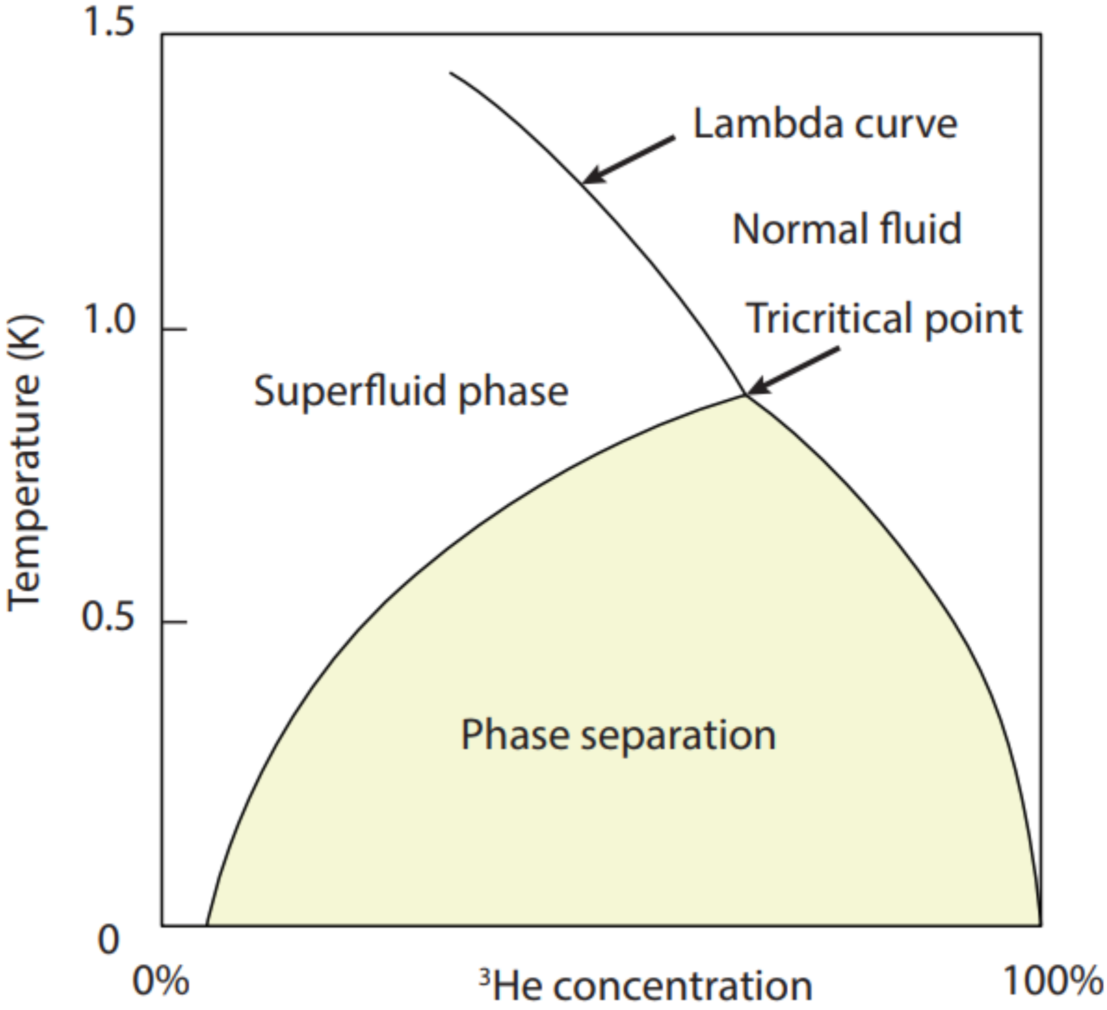

Figure 21: ^{3}He-^{4}He mixture phase diagram. Adapted from [5]

of the mixing chamber through the counter-flow heat exchanger and partially fills the still. Pumping on the still with the turbopump decreases the temperature of the still down to around 600 mK and reduces the ^{3}He concentration in the still. The reduced ^{3}He in the dilute phase is compensated by the ^{3}He from the concentrated phase. ^{3}He atoms absorb heat as they cross the phase boundary from the concentrated phase into the dilute phase in the mixing chamber, which provides cooling power for the sample stage. Pumped ^{3}He gas exiting the diaphragm pump is circulated back into the condenser of the DR and condenses into the liquid. The condenser's cooling power comes from the PPMS sample chamber wall. Then the liquid ^{3}He flows through the heat exchanger, gets further cooled, and enters the concentrated side of the mixing chamber, completing the circulation path.

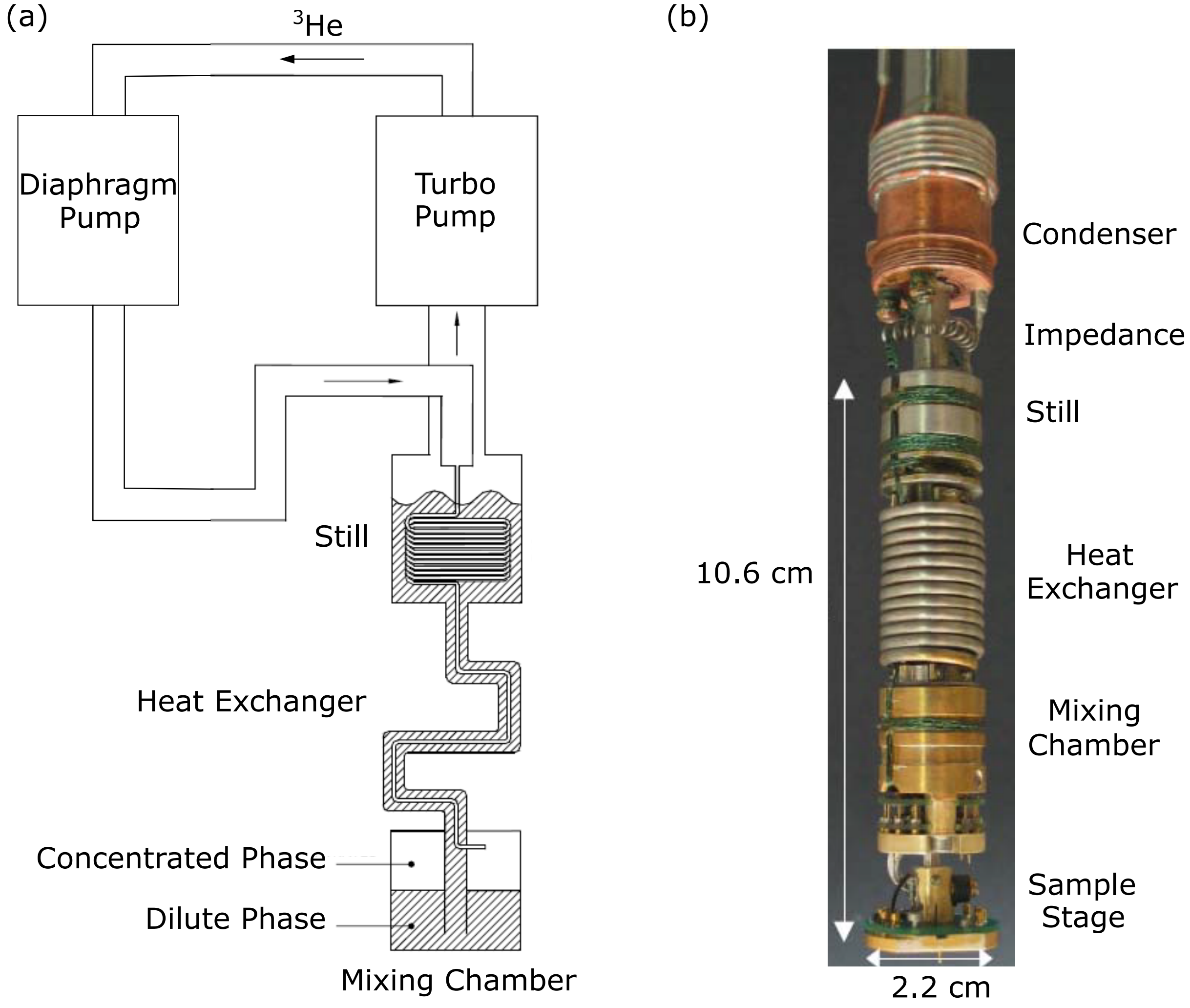

Figure 22: Dilution refrigerator. (a) Schematic of the working principle of a dilution refrigerator. (b) Quantum Design dilution refrigerator.

2.3.3 Electrical transport measurement

A Multichannel Lockin program is developed with LabVIEW in our lab, which communicates with hardware to apply voltages and measure signals from the device. Typically, there are two types of measurements, "I-V" using direct current (DC) and "lock-in" using an alternating current (AC). Transport experiments are performed by taking these two types of measurements on the device under different physical conditions such as temperature, magnetic fields, and side gate voltages.

I-V is performed by applying a sawtooth or triangular wave excitation voltage with a low frequency ($0.2 - 1$ Hz) and large amplitude ($1 - 3$ mV). The full waveform of the excitation voltage, measured current, and measured voltage signals are collected to construct two-terminal (measured current versus the excitation voltage) and four-terminal (measured current versus the measured differential voltage) I-V curves. I-V curves reveal transport behaviors of the device at both zero and finite biases. Typically I-V measurement is used to determine the lever arm ratio of an electron waveguide, which relates the applied side gate voltage to the chemical potential of the waveguide by calculating the ratio between the side gate voltage and voltage bias across the nanowire needed to make the same transition between adjacent bands.

Unlike I-V which gets a whole curve containing information at different biases from every measurement, lock-in only gets a single value at a single bias through the demodulation of measured signals. Lock-in uses a sine wave excitation voltage with a relatively high frequency ($1-13$ Hz) and small amplitude (around 100 μV). The Multichannel Lockin program demodulates the measured current and voltage signals at requested reference frequencies to obtain a single value at each reference frequency. Most of the time, only a single reference frequency is in use which is the same as the excitation voltage. For example, the frictional drag resistance is obtained by measuring the current in the drive nanowire and induced differential voltage across the drag nanowire at the frequency of the excitation voltage applied on the drive nanowire. Sometimes multiple reference frequencies are used. One example is monitoring the leakage and two-terminal conductance of nanowires simultaneously during the frictional drag device writing.

2.3.4 Thermopower measurement

Thermopower or thermoelectric measurement measures the induced thermoelectric voltage in response to a temperature difference across a material. In our lab, thermopower measurement uses the same software and hardware as electrical transport measurement. Take the thermopower measurement across an electron waveguide as an example. Thermopower measurement requires a temperature difference across the electron waveguide. As shown in Figure 23, a current is sourced on the left side of the electron waveguide between electrodes 1 and 2 with a frequency of f_h by applying V_{1,f_h} and V_{2,f_h} on electrodes 1 and 2, respectively. V_{1,f_h} and V_{2,f_h} are adjusted so that the potential at the intersection between the electron waveguide and left leads is zero to minimize the possible influence on thermopower voltage V_{2f_h} measurement. The current on the left side of the electron waveguide generates heat as it flows through the nanowire between electrodes 1 and 2, thus creating a temperature difference between the left and right sides of the electron waveguide. The heat is given by I^2R with I being the current and R being the resistance of the nanowire. Since the current has a frequency of f_h, the corresponding generated heat oscillates at a frequency of $2f_h$. The Multichannel Lockin program demodulates the voltage signal across the electron waveguide measured between electrodes 3 and 4 at $2f_h$ to obtain the induced thermopower voltage across the electron waveguide.

2.3.5 Data acquisition setup

Figure 24 (f) shows the schematic of the electronics setup for experiments. Bonding pads on the sample are connected to the chip carrier through wire bonding (Figure 11). The chip carrier is connected to the wiring in the DR insert. To avoid heat leaks, the wiring in the DR insert has low thermal conductance and is thermally anchored to the condenser, the still, and the mixing chamber before connected to the sample stage (Figure 22). The wiring in DR is connected to the breakout box through the Fischer connector provided by Quantum Design (the red box in Figure 24 (a)). The breakout box and measurement hardware are connected through a Pickering Matrix Module (the green box in Figure 24 (a); Figure 24 (d)). X channels of the Pickering Matrix are connected to electrodes of the

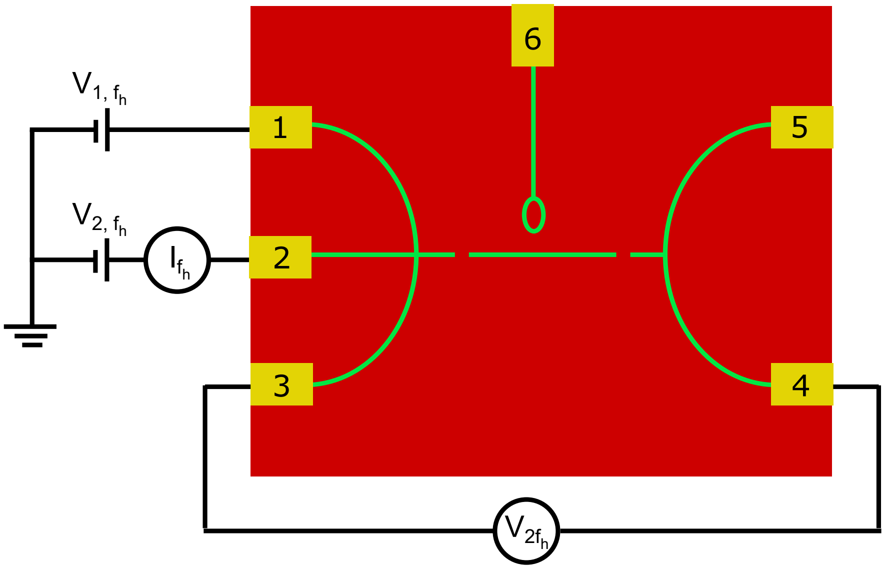

Figure 23: Thermopower measurement setup. Excitation voltage V_{1,f_h} and V_{2,f_h} with frequency f_h is applied on electrodes 1 and 2. V_{1,f_h} and V_{2,f_h} are adjusted so that the potential at the intersection between the electron waveguide and left leads is zero to minimize the influence on thermopower V_{2f_h} measurement. The induced thermopower voltage across the nanowire is measured between electrodes 3 and 4 at frequency $2f_h$.

breakout box (the white box in Figure 24 (a)), while Y channels of the Pickering Matrix are connected to analog inputs (AI) and analog outputs (AO) of data acquisition cards (the blue box in Figure 24 (a); Figure 24 (c)). As shown in Figure 24 (f), the Pickering Matrix allows switching the measurement configuration without physically touching cables. Any pair of X and Y channels of the Pickering Matrix can be connected through switches inside the Pickering Matrix, which is controlled by a LabVIEW program. AO channels are voltage sources controlled by the Multichannel Lockin program. The amplitude of the output voltage is at the order of 1 mV when AO channels are used to source current through the device. However, when AO channels are used for gate voltages, the amplitude is at the order of 100 mV. Directly applying such large voltages can irreversibly and drastically change the transport property of the device and make the device completely insulating. Therefore it

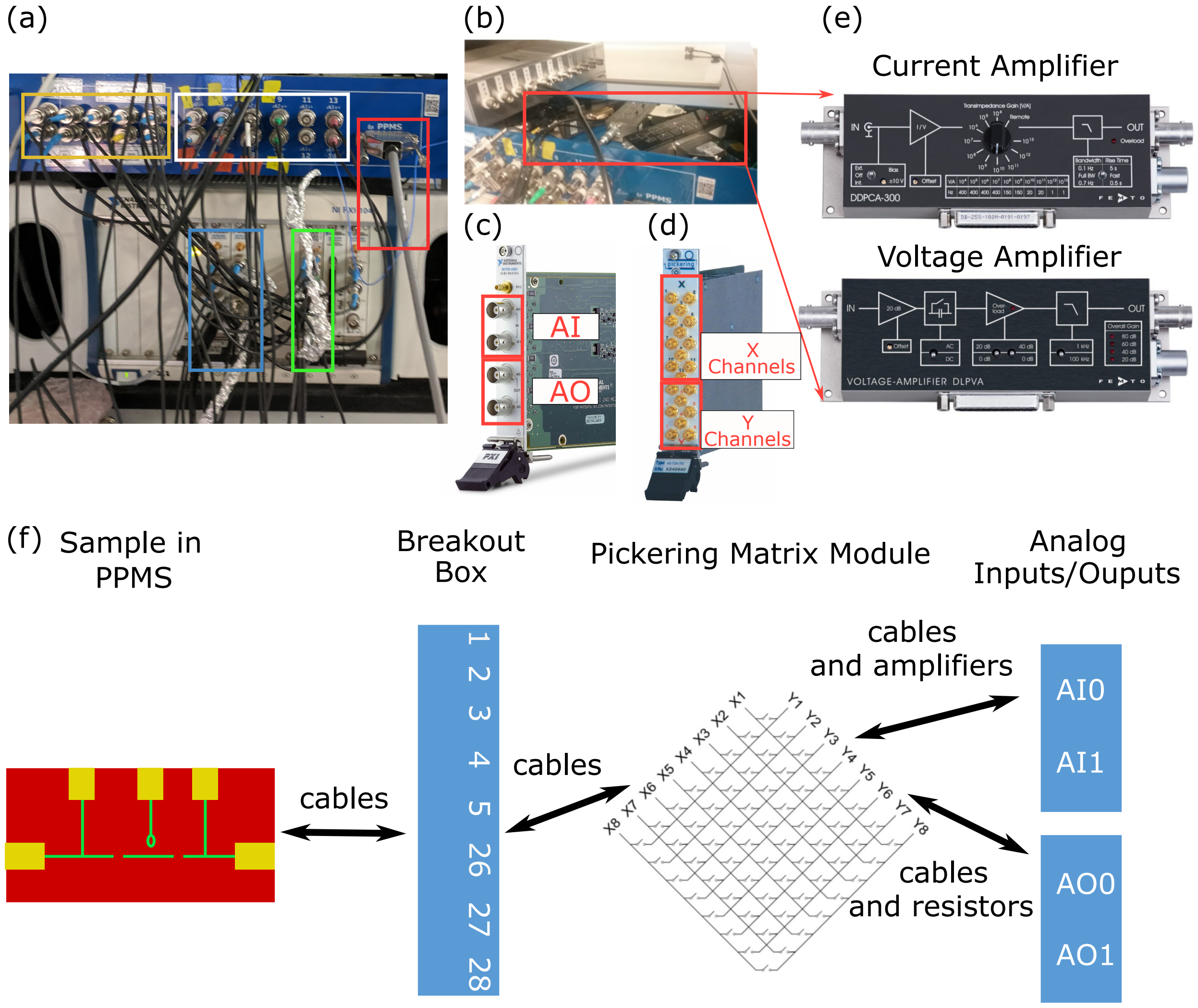

Figure 24: Electronics setup for experiments. (a) Breakout box is connected to DR by Quantum Design Fischer connector (red box). X channels of the Pickering Matrix Module (green box) is connected to the breakout box (white box). Y channels of the Pickering Matrix Module is connected to analog inputs or outputs (blue box) through amplifiers (yellow box) or resistors. (b) and (e) Current amplifier Femto model DDPCA and voltage amplifier Femoto model DLPVA. (c) Data acquisition cards (d) Pickering Matrix Module (f) The schematic of the electronics setup for experiments.

is important to connect the AO channel for the side gate with a large series resistor (100 M$\Omega - 1$ GΩ) to limit the current flow. AI channels receive signals from the sample after passing through the current (Femto model DDPCA-300) or differential voltage (Femto model DLPVA) amplifiers (the yellow box in Figure 24 (a); Figure 24 (b, e)). The signals collected by AI channels are then either directly outputted in an I-V measurement or demodulated by the Multichannel Lockin program to give the current or voltage reading in a lock-in measurement. The data acquisition process is controlled by the LabVIEW program, and the data is stored as text files ($*$.itx).

3.0 Long-Range Non-Coulombic Electron Interactions between $LaAlO_3/SrTiO_3$ Nanowires

3.1 Introduction

This chapter represents a collaborative work published in Yuhe Tang, Anthony Tylan-Tyler, Hyungwoo Lee, Jung-Woo Lee, Michelle Tomczyk, Mengchen Huang, Chang-Beom Eom, Patrick Irvin, Jeremy Levy, *Advanced Materials Interfaces*, **6** (15), 1900301 (2019) [148].

The $LaAlO_3/SrTiO_3$ system exhibits unusual magnetic and superconducting behavior arising from electron–electron interactions whose physical origin is not well understood. Quantum transport techniques, especially those involving mesoscopic geometries, can offer insights into these interactions. Here evidence for long-range electron–electron interactions in $LaAlO_3/SrTiO_3$ nanowires, measured through the phenomenon of frictional drag, is reported, in which current passing through one nanowire induces a voltage across a nearby electrically isolated nanowire. Frictional drag mediated by the Coulomb interaction is predicted to decay exponentially with interwire separation, but with the $LaAlO_3/SrTiO_3$ nanowire system it is found to be nearly independent of separation. Frictional drag experiments performed with three parallel wires demonstrate long-range frictional coupling even in the presence of an electrically grounded central wire. Collectively, these results provide evidence for a new long-range non-Coulombic electron–electron interaction unlike anything previously reported for semiconducting systems.

The heterointerface between the complex oxides $LaAlO_3$ and $SrTiO_3$ (LAO/STO) [111] exhibits a rich variety of electrically tunable properties such as superconductivity [124, 21], magnetism [17, 113], and spin–orbit coupling [135, 20]. Many of these properties have been associated with strong gate-tunable electron–electron interactions which can be challenging to dissect using conventional transport methods [28, 29]. The LAO/STO interface also exhibits a hysteretic metal–insulator transition [149], which can be controlled locally using conductive atomic force microscopy (c-AFM) lithography [22, 23] and used to create a range of mesoscopic devices [146].

The transport technique of Coulomb drag (or more generally "frictional drag") can provide unique insights into electron– electron interactions in the LAO/STO system [104]. When two electrical conductors are situated in close proximity, a current driven through one (the "drive") conductor may induce a voltage (or current) in the second ("drag") conductor. This effect was first proposed by Pogrebinskii [116] as a method to probe correlations among the charge carriers of the system. Frictional drag measurements have been carried out in coupled 2D–3D semiconductor systems [140, 139], coupled semiconductor two-dimensional electron gases (2DEGs) [50, 51, 53, 139, 40] and graphene systems [88, 84], 1D–1D nanowires defined from semiconductor 2DEGs [33, 162, 82], and in coupled semiconductor quantum dots [74]. In these systems, the physical mechanism underlying frictional drag is dominated by Coulomb interactions. At large separations, non-Coulombic corrections can become apparent in some semiconductor devices [52, 153, 154].

3.2 Experimental Methods

The device fabrication process is illustrated in Figure 25 (a). C-AFM lithography is used to define nanowires at the interface between 3.4 unit cells (uc) of LAO deposited on an STO substrate by pulsed laser deposition (PLD). Details of the sample growth and fabrication of electrical contacts are described elsewhere [18, 22]. Positive tip voltages applied on the LAO surface produce locally conductive regions at the LAO/STO interface. The mechanism for the writing process is attributed to surface protonation [18, 8]. A typical frictional drag system (illustrated in Figure 25 (b)) is composed of two parallel nanowires with a width $w \sim 10$ nm, length L ranging between 400 nm and 1.5 μm, and separation d ranging between 40 nm and 1.5 μm. Devices consisting of three parallel nanowires (shown in Figure 25 (c)) are also investigated. Except where noted otherwise, all measurements are performed below $T = 100$ mK. In both double-wire (Figure 25 (b)) and triple-wire (Figure 25 (c)) device geometries, frictional drag measurements are performed by sourcing a current I_j in nanowire j and measuring an induced voltage V_i in nanowire i. All nanowires are connected to the

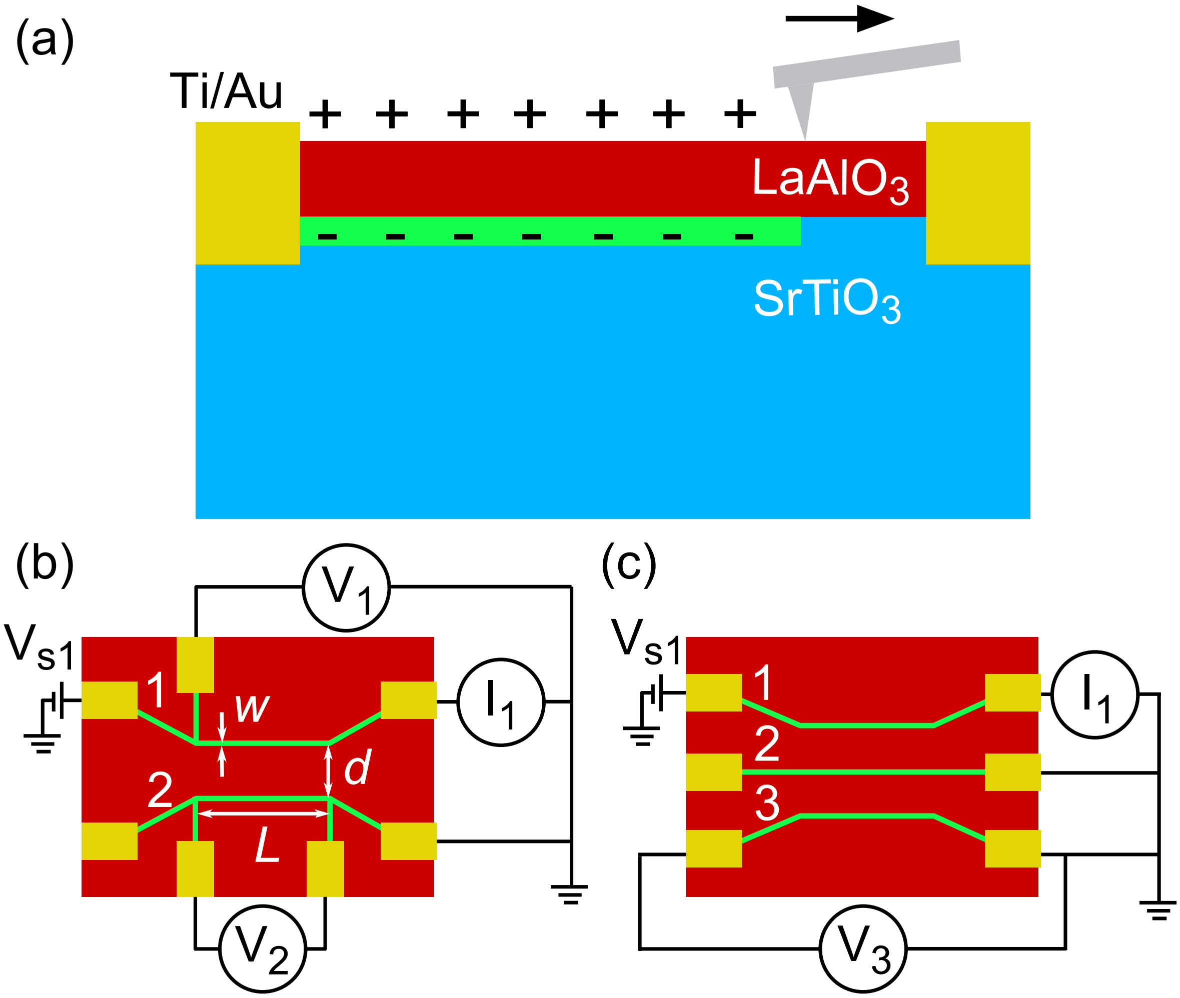

Figure 25: Non-Coulombic frictional drag experimental setup. (a) Side-view of the nanowire fabrication process. A nanowire is created at the LAO/STO interface between two Ti/Au electrical contacts with c-AFM lithography. Protons (+) patterned on the surface by the AFM tip attract electrons (−) to the interface forming a nanowire (green area). (b) Top-view schematic of the double nanowire device with length L, width w, and wire separation d. The setup measures the induced drag voltage $V_{\text{drag}} = V_2$ across wire 2 created by current I_1, which is induced by application of a voltage V_{S1} across wire 1. (c) Schematic of a triple nanowire device where drag voltage V_3 induced by I_1 is measured. All three wires are grounded during the measurement.

same ground during the measurement. The current I_j is produced by applying a voltage $V_{Sj} = V_{DC} + V_{AC}\cos\omega t$ to one end of nanowire j; the resulting current $I_j(\omega)$ and induced voltage $V_j(\omega)$ at frequency ω are measured using a lock-in amplifier. The resistance may then be expressed as a matrix $R_{ij} = dV_i/dI_j = V_i(\omega)/I_j(\omega)$, which is generally a function of the DC drive current I_j (as well as other parameters such as temperature T and applied magnetic field $\vec{B}$). The off-diagonal terms then define the drag resistance R_{ij}, characterizing the mutual friction between electrons in the drive and drag nanowires. In order to ensure that the drag resistances R_{ij} are not influenced by electron tunneling between the two nanowires, we characterized IV properties across two nanowires from all devices before experiments (see Figure 26 for typical data). All measurements are performed well below the measured interwire breakdown voltage of each device.

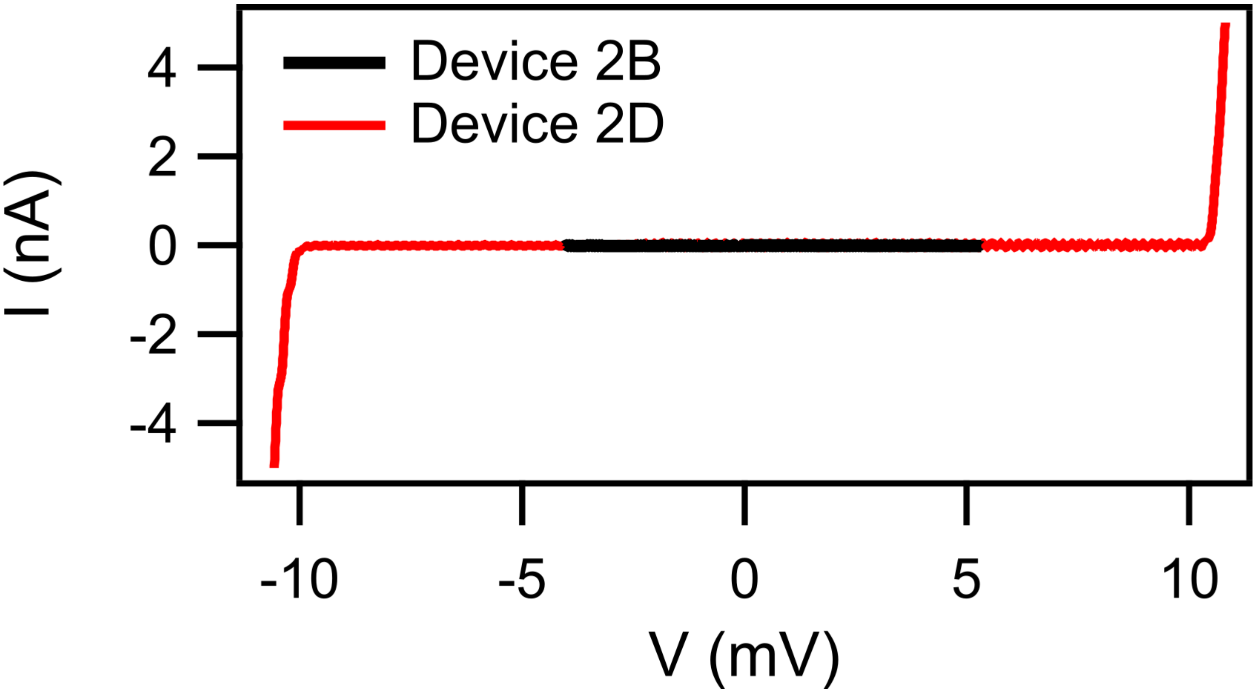

Figure 26: IV properties across two nanowires. Data is from Device 2B ($d = 40$ nm) and 2D ($d = 550$ nm).

3.3 Results and Discussion

Two tables are provided that list device parameters for double-wire and triple-wire devices. Parameters for double-wire devices include lengths and separations between nanowires, two-terminal resistance, four-terminal resistance, and drag resistance measured from each nanowire. In the table for triple-wire devices, each row corresponds to a different measurement configuration depending on which two nanowires are used for drive and drag wires. For example, $3A_{12}$ corresponds to the configuration where wire 1 and 2 are utilized and wire 3 is the grounded wire. R_{12} is the drag resistance measured from wire 1 with wire 2 being the drive wire and vice-versa for R_{21}. Due to the limitation of the number of electrodes, there is no four-terminal resistance in the triple-wire device table.

Table 1: Double-wire device parameters

Device	L (nm)	d (nm)	$R_{2\mathrm{T},\,1}$ (kΩ)	$R_{2\mathrm{T},\,2}$ (kΩ)	R_{11} (kΩ)	R_{22} (kΩ)	R_{12} (Ω)	R_{21} (Ω)
2A	400	40	58 – 72	42 – 48	31.3 – 43.5	8.4 – 9.2	20	60
2B	400	40	22 – 31	26 – 34	8.6 – 12.5	14.0 – 18.3	14	4
2C	1000	300	37 – 47	25 – 46	NA	8.7 – 18.4	51	23
2D	1500	550	27 – 35	29 – 63	NA	7.8 – 11.8	15	52
2E	1500	550	22 – 29	33 – 77	NA	NA	27	26
2F	1500	550	23 – 36	22 – 51	11.5 – 16.0	3.7 – 5.5	19	41
2G	1500	1500	17 – 27	22 – 37	10.2 – 14.8	2.7 – 4.1	10	9

3.3.1 Double-wire device results

Typical results of a frictional drag measurement are shown in Figure 27 (a). The nanowires are rendered non-superconducting by a magnetic field $\vec{B} = B\hat{z}$ (where $|B| > 0.2$ T) applied perpendicular to the heterointerface. The magnitude of R_{21} varies with B and is antisymmetric in the drive current I_1. In frictional drag measurements, R_{ij} is expected to be symmetric about $I_j = 0$ as the interaction transfers momentum from the drive system

Table 2: Triple-wire device parameters. Subscripts i and j represent nanowires used in a configuration. R_{ij} and R_{ji} represent drag resistances measured from wire i and j, respectively.

Config ($3\mathrm{A}_{ij}$)	L (nm)	d (nm)	$R_{2\mathrm{T},i}$ (kΩ)	$R_{2\mathrm{T},j}$ (kΩ)	R_{ij} (Ω)	R_{ji} (Ω)
$3\mathrm{A}_{12}$	1500	750	$26-41$	$26-34$	14	5
$3\mathrm{A}_{13}$	1500	1500	$26-41$	$29-47$	10	18
$3\mathrm{A}_{23}$	1500	750	$26-34$	$29-47$	8	30

to the drag system [33, 162, 82, 85]. Thus, when I_j changes sign, so should V_i. One possible origin of antisymmetric R_{ij} is an induced thermopower effect in the drag wire from Joule heating in the drive wire. But this possibility can be ruled out because the drag voltage is expected to scale as I^2, causing the drag resistance to scale linearly with I, which is not what we observe. The fact that R_{ij} is antisymmetric with respect to I_j indicates that the inversion symmetry of the nanowires is broken somewhere and that quantum shot noise in the drive wire is primarily responsible for the drag voltage V_2 [85].

3.3.2 Separation dependence

In order to help identify the electron–electron interactions responsible for frictional drag in this system, we have created several devices with differing L and d, as delineated in Tables 1 and 2. The maximum values for $|R_{ij}|$ for the magnetic field range explored (0.2 T $\leq B \leq$ 9 T) are plotted as a function of nanowire separation d (Figure 27 (b)). Circle and square markers represent double-wire and triple-wire devices, respectively. Square markers are composed of red, blue, and black segments that represent the arrangement of drive, drag, and grounded wires, respectively. For example, a circle marker with blue on top corresponds to a measurement of R_{12} in a double-wire device and a square one with the color blue, black, and red from top to bottom corresponds to a measurement R_{13} for a triple-wire device. As shown in Figure 27 (b), the electron–electron interactions between the drive and

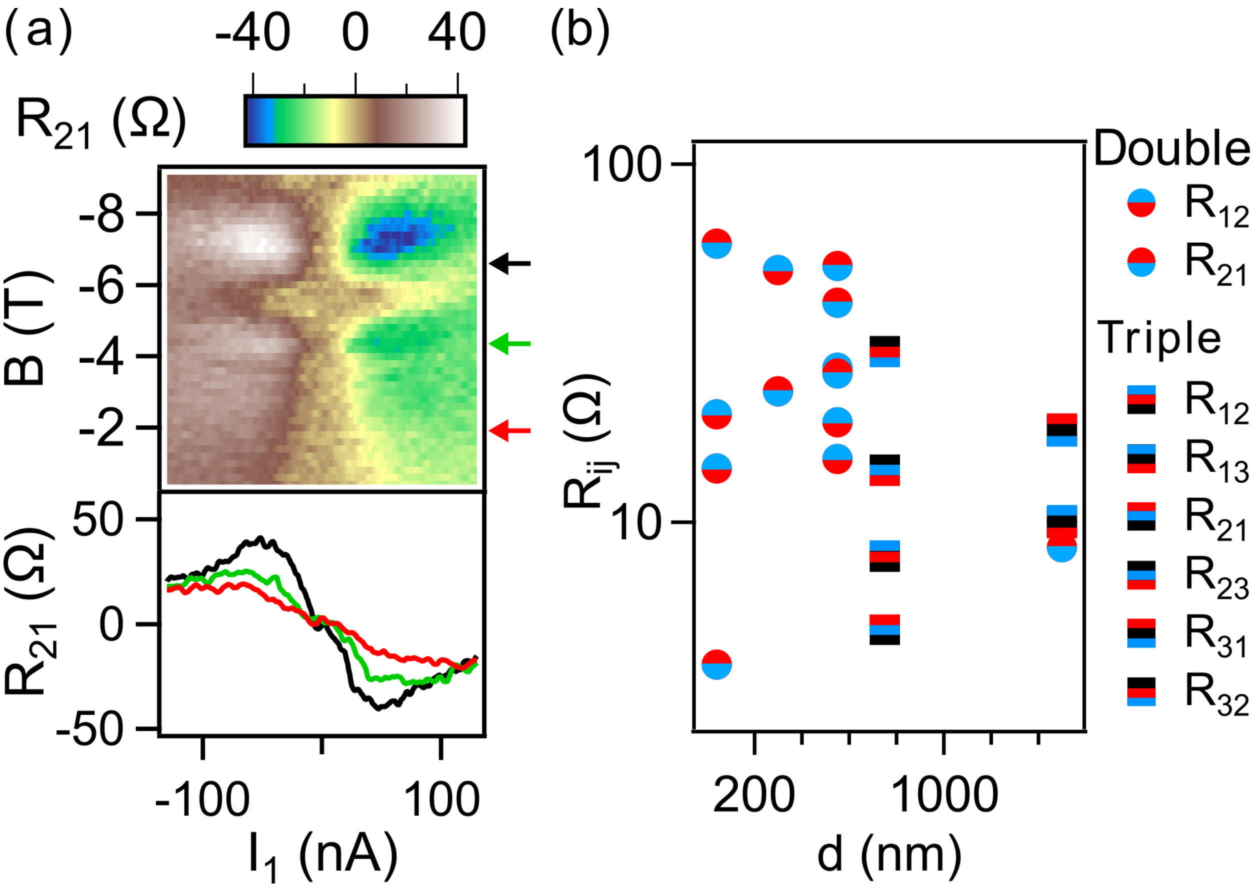

Figure 27: Magnetic-field and separation dependence of drag resistance in non-Coulombic frictional drag. (a) Top panel, drag resistance R_{21} as a function of bias current I_1 and magnetic field B (Device 2F in Table 1). Bottom panel, line profiles of R_{21} at $B = -7$ T (black), -4.6 T (green), and -2 T (red). (b) Drag resistance R_{ij} as a function of d in the normal-state regime in double- and triple-wire devices. Circle and square markers represent double- and triple-wire devices. Red, blue, and black represent drive, drag, and grounded wire, respectively. The relative position of the three colors corresponds to the measurement configuration in the device

drag nanowires exhibit large variations with little if any explicit dependence on the nanowire separation d. Since the experiments are performed in a nonequilibrium regime where there is a bias across the drive wire and a magnetic field is applied, the well-known Onsager relations do not necessarily apply. Thus, R_{ij} can be quite different from R_{ji}. The unusual scaling with distance would be a significant departure from the expected behavior if the Coulomb interaction were responsible for the drag resistance. In the case when a Coulomb interaction gives rise to a drag voltage in coupled nanowires, Raichev and Vailopoulos predict that $R_{ij} \propto e^{-4k_F d}/\kappa^2$, where $k_F \sim$(10nm)$^{-1}$ is the Fermi wave vector, and $\kappa = 4\pi\epsilon$ with $\epsilon > 10000$ being the dielectric constant of STO [100, 122]. Such an exponential decay with distance is absent in our measurements. Moreover, the exceptionally large dielectric constant of STO (and proximity to an incipient ferroelectric instability) should lead to a suppression of R_{ij} by several orders of magnitude smaller compared with those measured in similar devices formed from other material systems [33, 162, 82]; however, no such reduction is found. The weak scaling with separation and the insensitivity to the large dielectric constant of STO indicate that the electron–electron interactions responsible for frictional drag are non-Coulombic in nature.

3.3.3 Triple-wire device results

In order to further explore the nature of the long-range interactions leading to frictional drag, experiments with three parallel nanowires are investigated in detail. Schematics for two configurations (Figure 28 (a,b)) yield measurements of R_{12} and R_{13}, respectively (Figure 28 (c,d)), as a function of drive current and magnetic field. A comparison of R_{12} and R_{13} allows for the nanowire separation to be varied within a single device, and simultaneously probes the impact of introducing a central, grounded screening wire (for the case of R_{13}). Both the pattern and the magnitude of R_{12} and R_{13} are nearly identical, despite d doubling (Figure 28 (e)). This result is consistent with the statistical findings summarized in Figure 27 (b). The frictional drag for the R_{13} geometry is naively expected to be impacted by screening from the central wire. Instead, there is no discernible screening effect. The triple-wire device geometry also enables one to ascribe the origin of the unique magnetic signature of the drag signal (i.e., Figures 27 (a) and 28 (c)) to the properties of the drag wire and not the source wire.

3.3.4 Temperature dependence

In 2D semiconductor drag systems, virtual phonon exchange was shown to be independent of distance [52, 153, 154]. The phonon-mediated coupling of the drag and drive systems, however, had a characteristic temperature scaling; the phonon-mediated drag is expected to increase with increasing temperature [52, 104]. Figure 29 shows the typical temperature dependence of frictional drag. The drag resistance decreases monotonically with increasing temperature, becoming negligible for $T > 500$ mK. This temperature dependence is inconsistent with phonon-mediated frictional drag reported for 2D systems.

3.4 Conclusion

Frictional drag measurements between nanowires created on the LAO/STO heterointerface exhibit a strong, distance-insensitive coupling, which indicates a non-Coulombic interaction. The temperature dependence of this effect is incompatible with other known non-Coulombic interactions, such as virtual phonon exchange [52, 153, 154, 104]. While these measurements do not specifically point to a particular coupling mechanism, there are candidates worth considering. STO possesses a bulk cubic structure at room temperature that is unstable to an anti-ferrodistortive transition to a tetragonal phase below $T = 105$ K [129]. The ferroelastic domain structure gives rise to domain walls, which are correlated with anisotropic electronic phenomena observed at LAO/STO heterointerface [72]. Ferroelastic domain walls are nominally insulating in bulk, but they are also reported to be polar and mobile under applied electric fields. The coupling of ferroelastic strain states and local surface potentials could potentially mediate long-range interactions through the insulating near-surface bulk STO layer [61]. Long-range couplings, whether mediated through ferroelastic domains or some other as-yet-unidentified mechanism, introduce a fascinating new element to the celebrated electronic properties of this oxide interface.

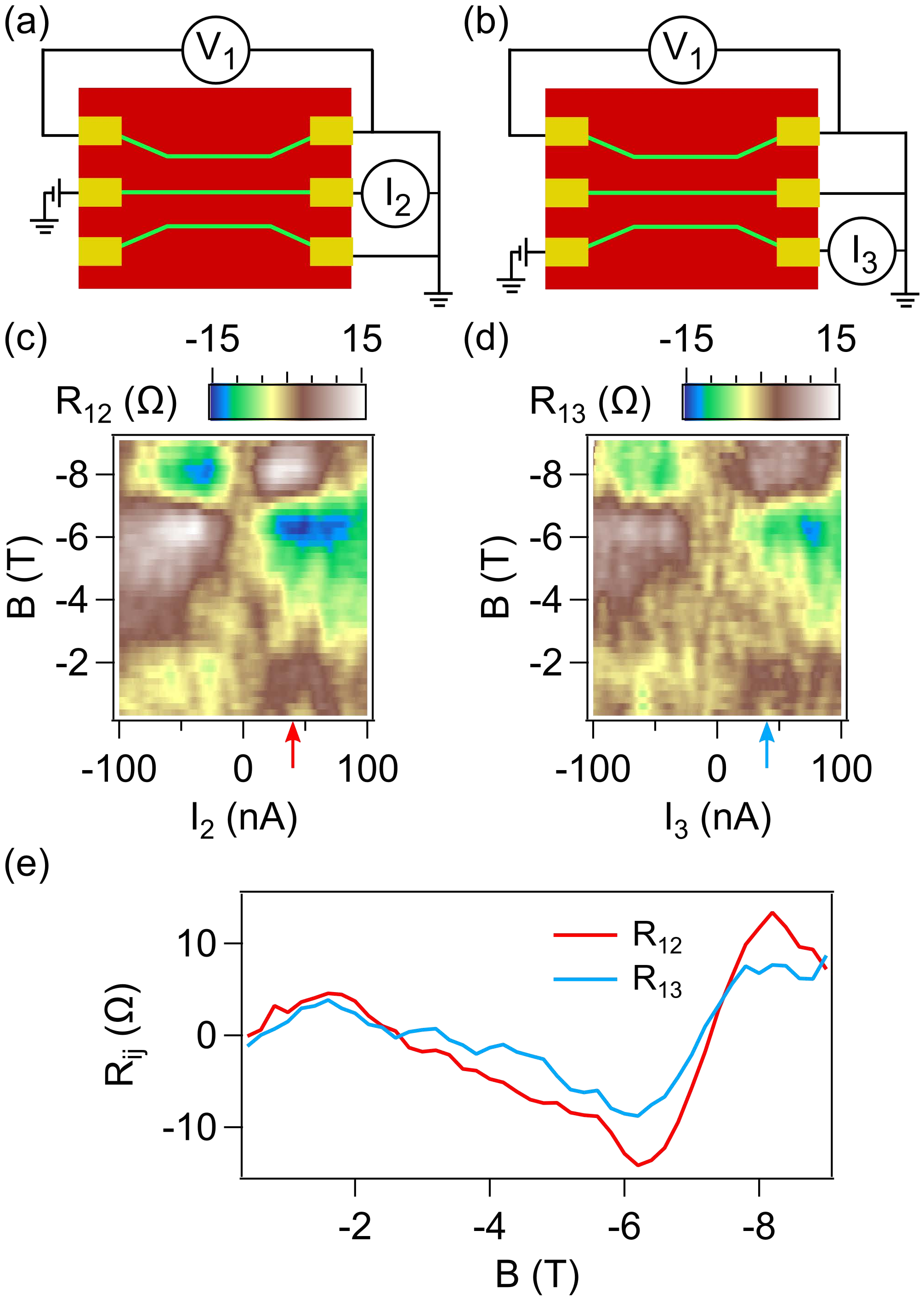

Figure 28: Triple-wire experimental data. (a), (b) Schematics of triple-wire frictional drag. Drag voltage V_1 is measured from wire 1 with current sourced in wire 2 and 3, respectively. (c), (d) Drag resistance R_{12} and R_{13} corresponding to configurations in (a) and (b) plotted as a function of B. (e) Line profiles at I_2 and $I_3 = 40$ nA in (c) and (d)

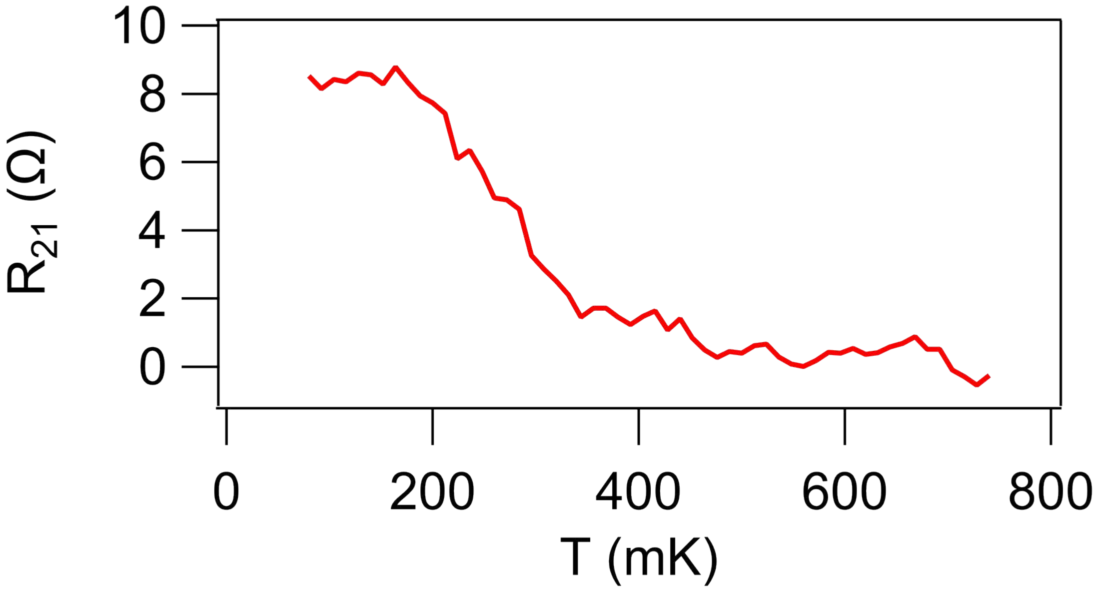

Figure 29: Temperature dependence of drag resistance. R_{21} between $T = 80$ mK and $T = 740$ mK at sourcing current $I_2 = -100$ nA and $B = -9$ T (Device 2G). The drag resistance becomes negligible above $T = 500$ mK for all of the devices investigated.

4.0 Frictional Drag between Superconducting $LaAlO_3/SrTiO_3$ Nanowires

4.1 Introduction

The contents of this chapter represent a collaborative work published in Yuhe Tang, Jung-Woo Lee, Anthony Tylan-Tyler, Hyungwoo Lee, Michelle Tomczyk, Mengchen Huang, Chang-Beom Eom, Patrick Irvin, Jeremy Levy, *Semiconductor Science and Technology*, **35** (9), 09LT01 (2020) [147].

We report frictional drag measurements between two superconducting $LaAlO_3/SrTiO_3$ nanowires. In these experiments, a current passing through one nanowire induces a voltage across a nearby electrically isolated nanowire. The frictional drag signal contains both symmetric and anti-symmetric components. The anti-symmetric component arises from the rectification of quantum shot noise in the drive nanowire by the broken symmetry in the drag nanowire. The symmetric component in the drag resistance is ascribed to the rectification of thermal noise in the drive nanowire during the superconducting-normal transition. The suppression of the symmetric component is observed when a normal nanowire is used as either a drag or drive nanowire with the other nanowire superconducting. The absence of the symmetric drag resistance between a normal drag nanowire and a superconducting drive nanowire suggests a higher electron-hole asymmetry in the superconducting $LaAlO_3/SrTiO_3$ nanowire arising from the 1D nature of superconductivity at the $LaAlO_3/SrTiO_3$ interface.

$SrTiO_3$ (STO) has long attracted interest as a superconducting semiconductor [133, 90, 112]. Recently, interest in the superconducting properties of STO was revived by the development of STO-based heterostructures and nanostructures and with the $LaAlO_3/SrTiO_3$ (LAO/STO) system [111] in particular. The LAO/STO two-dimensional interface supports superconductivity, which is electrostatically gateable, and various transport techniques have been used to study the superconductivity at the interface [125]. The superconducting transition temperature (T_c) has a dome shape as a function of carrier density, which is controllable via a back gate [21]. With the use of conductive atomic force microscope (c-AFM) lithography, nanoscale control over the conductance of the LAO/STO interface is possible. This technique relies on AFM tip-controlled protonation or deprotonation of the LAO surface, which enables the creation of a wide variety of quantum-confined structures, including superconducting nanowires [157], ballistic 1D electron waveguides [1], and single-electron transistors [27, 28]. These mesoscopic devices, drawn from a well-established toolset of quantum transport, often exhibit surprising new properties due to the unique physics of the STO interface such as electron pairing without forming superconductivity [28]. Recently by studying the superconductivity in LAO/STO nanowires of different widths and numbers, it is discovered that superconductivity exists at the boundary of nanowires and is absent within the interior region of nanowires, which indicates the 1D nature of superconductivity at the LAO/STO interface [112].

Coulomb drag [104], or more generally frictional drag, first proposed by Pogrebinskii [116], has proven to be a powerful technique to study electron transport and electronic correlations. When two electrical conductors are placed in close proximity, a current driven through one ("drive") conductor may induce a voltage (or current) in the second ("drag") conductor. Frictional drag measurements have mostly been carried out between normal-state conductors in coupled 2D semiconductor systems [50, 51, 53, 139, 40], graphene systems [88, 84], 1D semiconductor systems [33, 162, 82], 1D complex oxide systems [148], and quantum dot systems [74]. Frictional drag in the superconducting regime has been carried out in normal-metal-superconductor systems [46, 65] and the phenomenon is explained by the local fluctuating electric field induced by mobile vortices in the superconducting layer [136] or Coulomb coupling between two conductors [73, 37]. There are, to our knowledge, no prior reports of frictional drag between two quasi-1D superconductors.

Previously-reported frictional drag experiments at the LAO/STO-based nanowires have shown surprising results, particularly in the high magnetic field regime [148]. The drag resistance is anti-symmetric, indicating that the drag resistance arises via rectification of quantum shot noise in the drive nanowire due to the broken inversion symmetry of the drag nanowire [85]. Remarkably, the drag resistance shows little to no dependence on the separation between nanowires (up to $\sim \mu$m scales). This unusual scaling strongly indicates that non-Coulombic interactions dominate the coupling between these nanowires.

Here we report frictional drag experiments between two LAO/STO superconducting nanowires. The drag resistance contains a mixture of symmetric and anti-symmetric components and the symmetric component disappears whenever one nanowire is normal and the other is superconducting. The anti-symmetric component arises for the same reasons as in the high B regime. The symmetric component is ascribed to the rectification of thermal noise in the drive nanowire during the superconducting-normal transition. Suppression of the symmetric drag component, when a normal nanowire is used as the drag nanowire, suggests the existence of a higher electron-hole asymmetry [102] in the superconducting LAO/STO nanowires arising from the 1D nature of superconductivity at the LAO/STO interface.

4.2 Experimental Methods

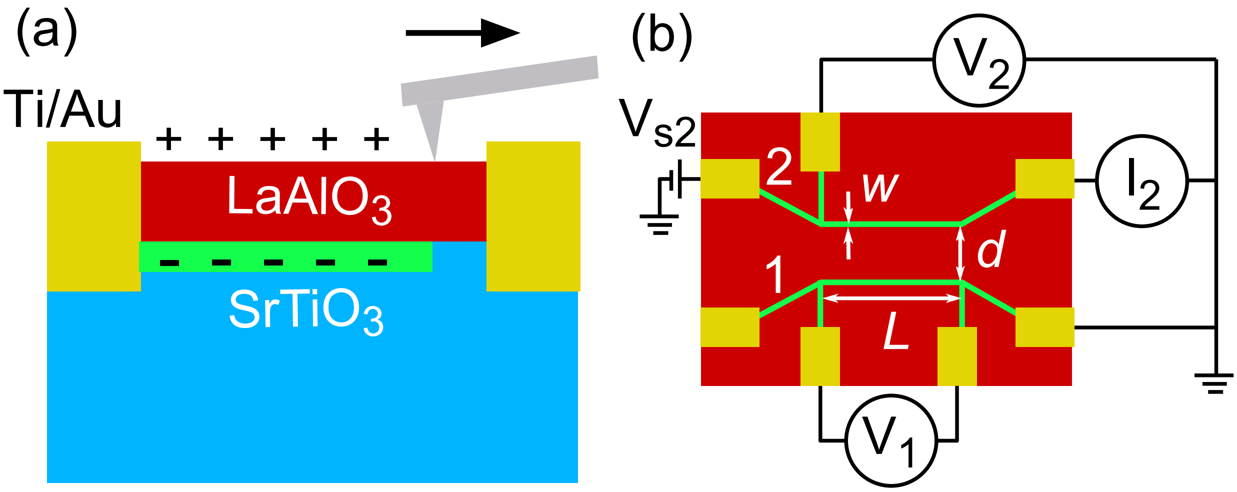

Figure 30: Superconducting frictional drag experimental setup. (a) Side-view of the nanowire fabrication process. A nanowire is created at the LAO/STO interface between two Ti/Au electrical contacts with c-AFM lithography. Protons (+) patterned on the surface by the AFM tip attract electrons (−) to the interface forming a nanowire (green area). (b) Top-view schematic of the double nanowire device with length L, width w, and nanowire separation d. The setup measures the induced drag voltage V_1 across nanowire 1 created by the current I_2, which is induced by the application of a voltage V_{S2} across nanowire 2.

Nanowire devices are 'sketched' on LAO/STO heterostructures using c-AFM lithography [22] (Figure 30 (a)). LAO/STO heterostructures with an LAO thickness of 3.4 unit cells are grown by pulsed laser deposition (PLD). Further details of the sample growth and the device fabrication process are described elsewhere [18]. The width of the nanowires used for these experiments is approximately $w = 10$ nm, as quantified by erasure experiments [22]. Other device parameters include the separation between nanowires d and the nanowire length L. Here we focus on two sets of parameters: $d = 40$ nm and $L = 400$ nm (Device 2B, Figure 31) and $d = 40$ nm and $L = 300$ nm (Device 2J, Figure 34). To investigate frictional drag at the LAO/STO interface in the superconducting regime, the magnitude of B is kept below 0.3 T and the temperature less than 100 mK (except for temperature-dependent measurements that explicitly go above $T = 100$ mK).

In a frictional drag experiment, a voltage V_i in nanowire i is induced by a current I_j in nanowire j (Figure 30 (b)). All nanowires are connected to the same ground during the measurement. The current I_j is produced by applying a voltage $V_{\mathrm{S}j} = V_{\mathrm{DC}} + V_{\mathrm{AC}} \cos \omega t$ to one end of nanowire j; the resulting AC components current $I_j(\omega)$ and induced voltage $V_j(\omega)$ at frequency ω are measured using a lock-in amplifier. The resistance may then be expressed as a matrix $R_{ij} = dV_i/dI_j = V_i(\omega)/I_j(\omega)$, which is generally a function of the DC drive current I_j (as well as other parameters such as temperature T and applied magnetic field $\vec{B}$). The off-diagonal terms that define the drag resistance R_{ij} characterize the mutual friction between electrons in the drive and drag nanowires. A standard low ω technique is used with the typical ω around 7 Hz. We varied ω from 2 to 14 Hz and did not find the ω scaling of R_{ij}. In order to ensure that the drag resistances R_{ij} are not influenced by current leakage between the two nanowires, all measurements are performed well below the inter-wire breakdown voltage (~ 10 mV) measured for each device.

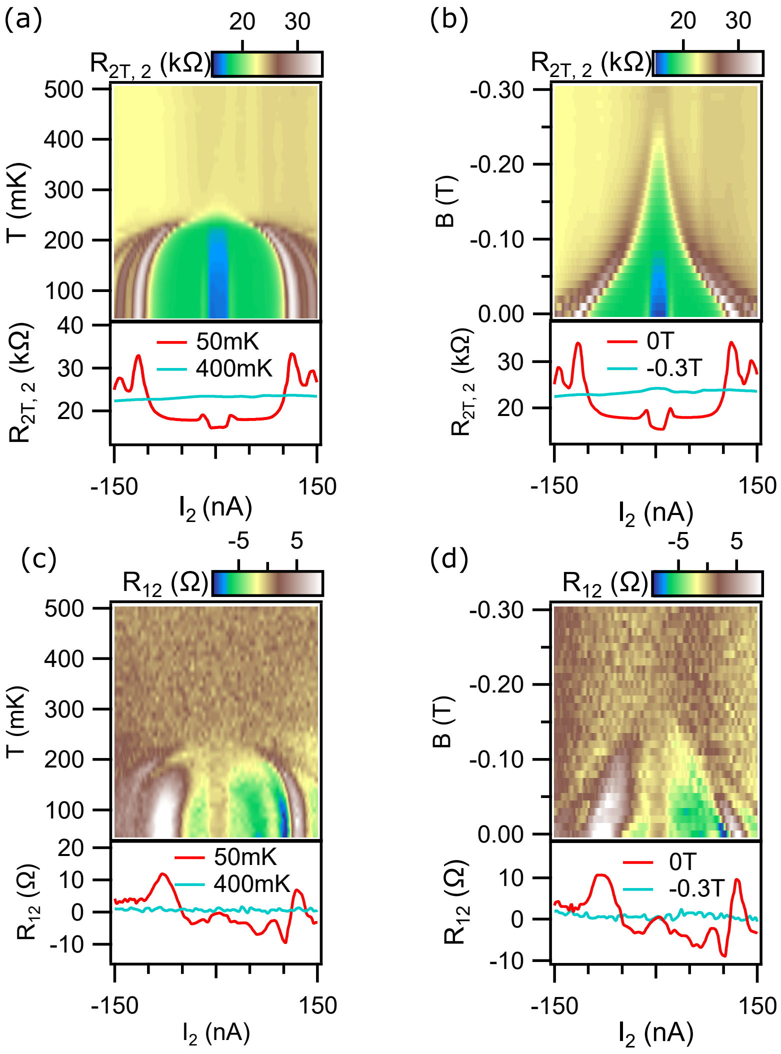

Figure 31: Temperature and magnetic-field dependence of the drag resistance and two-terminal resistance in superconducting frictional drag. (a) T dependence and line profiles of two-terminal resistance $R_{2\mathrm{T},\,2}$ from nanowire 2. Top panel, T dependence of $R_{2\mathrm{T},\,2}$. Bottom panel, line profiles of $R_{2\mathrm{T},\,2}$ at 50 mK and 400 mK. (b) B dependence and line profiles of $R_{2\mathrm{T},\,2}$. (c) T dependence and line profiles of drag resistance R_{12} from nanowire 1. (d) B dependence and line profiles of R_{12}. T dependence experiments in (a) and (c) are performed at 0 T. B dependence experiments in (b) and (d) are performed at 80 mK.

4.3 Results and Discussion

4.3.1 Frictional drag between two superconducting nanowires

Typical frictional drag resistance measurements in the superconducting regime are shown in Figure 31. T dependence experiments in Figure 31 (a) and (c) are performed at 0 T. B dependence experiments in (b) and (d) are performed at 80 mK. Both nanowires in Device 2B show signatures of superconductivity [157, 112]. As shown in the bottom panels of Figure 31 (a) and (b), nanowire 2 displays three superconducting-normal transitions with critical current I_c defined as the location of the peaks in $R_{2\mathrm{T},2}$ [157]. The first is at ±20 nA, the second at ±110 nA, and the third at ±140 nA. Non-vanishing resistances in superconducting nanowires are common and are attributed to normal hot spots below I_c [150] or quantum phase slips [45]. Besides, the smallness of nanowire width ($w \sim 10$ nm) can make the difference between superconducting and normal resistances even smaller due to phase-slip mechanisms [83]. The superconducting-normal transition at ±20 nA arises from the nanowire since it shows up both in $R_{2\mathrm{T},\,2}$ and four-terminal resistance R_{22} and the transition at ±110 nA and ±140 nA arises from wires connecting the nanowire and electrodes since it only shows up in $R_{2\mathrm{T},2}$ (Figure 32). The drag resistance R_{12} is greatly enhanced in the superconducting regime, as shown by examining both the temperature-dependence (Figure 31 (c)) and the magnetic-field dependence (Figure 31 (d)). The nature of R_{12} in the superconducting regime is qualitatively different from the high magnetic field regime (where the nanowires are not superconducting). In the high magnetic field regime, the drag resistance R_{ij} is anti-symmetric [148] with respect to the sourcing current, while the superconducting response is asymmetric with drive current. The superconducting R_{ij} is mostly symmetric between $I_2 = \pm 40$ with two tiny dips at ±10 nA. As the magnitude of I_2 increases, an anti-symmetric component starts showing up in R_{ij} and R_{ij} becomes asymmetric.

4.3.2 Symmetric and anti-symmetric components analysis

The appearance of asymmetric R_{12} (Figures 32 (c) and (d)) in the superconducting regime is correlated with the superconductivity in the drive nanowire 2 (Figure 32 (a) and

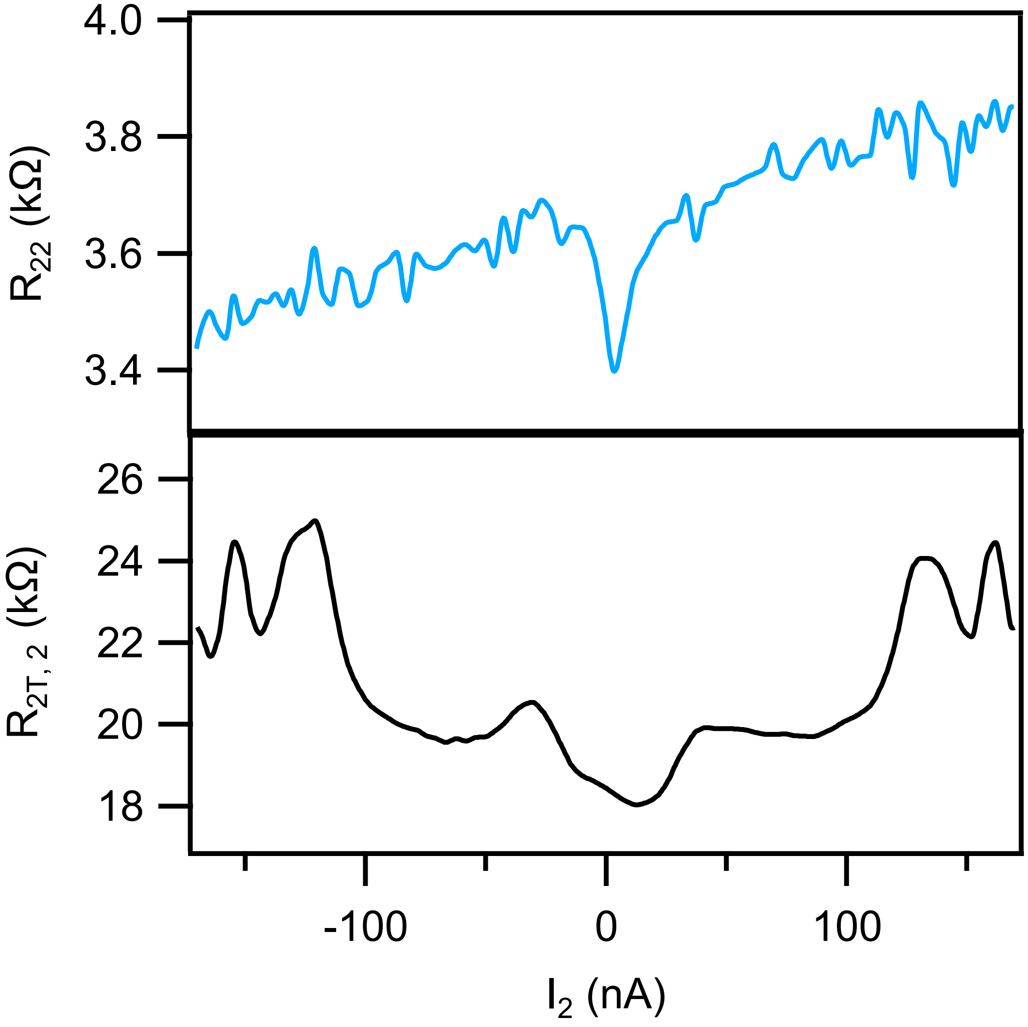

Figure 32: Two-terminal and four-terminal resistances of a superconducting nanowire. Top panel: Four-terminal resistance R_{22} and superconducting-normal transition from the nanowire only shows up at small bias from ±20 nA. Bottom panel: Two-terminal resistance $R_{2\mathrm{T},\,2}$. Besides the superconducting-normal transition at small bias, extra superconducting-normal transitions show up at larger bias ±110 nA and ±150 nA. Superconducting-normal transitions at larger bias come from wires connecting the nanowire and electrodes.

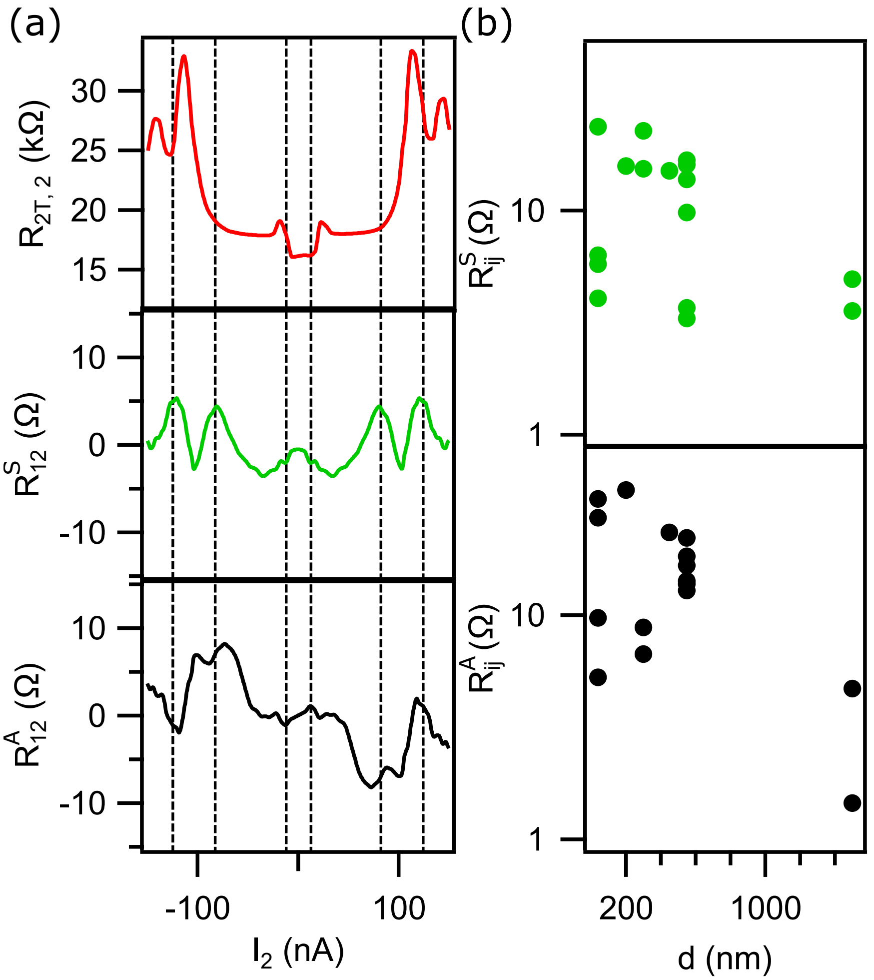

Figure 33: Symmetric and anti-symmetric components of drag resistance in superconducting frictional drag. (a) Typical symmetric and anti-symmetric components of drag resistance from Device 2B. Top panel: Two-terminal resistance $R_{2\mathrm{T},2}$ of drive nanowire. Middle panel: Symmetric component of drag resistance R^{S}_{12}. Bottom panel: Anti-symmetric component of drag resistance R^{A}_{12}. Dashed lines pinpoint locally strongest drag resistance in R^{S}_{12} (b) d dependence of maximum symmetric and anti-symmetric components of drag resistance from different samples. d ranges from 40 nm to 1.5 μm. Top panel: Symmetric component R^{S}_{ij} as a function of d. Bottom panel: Anti-symmetric component R^{A}_{ij} as a function of d.

(b)). To further understand the frictional drag in the superconducting regime, we extract symmetric and anti-symmetric components by $R_{ij}^{\mathrm{S}}(I) = (R_{ij}(I) + R_{ij}(-I))/2$ and $R_{ij}^{\mathrm{A}}(I) = (R_{ij}(I) - R_{ij}(-I))/2$. $R_{2\mathrm{T},\,2}$, R_{ij}^{S}, and R_{ij}^{A} are shown in the top, middle, and bottom panels of Figure 33 (a). Dashed lines pinpoint the locally strongest drag resistance in R_{12}^{S}. As shown in Figure 33 (a), the locally strongest R_{12}^{S} shows up around the superconducting-normal transition represented by peaks in $R_{2\mathrm{T},\,2}$ in the drive nanowire 2 accompanied by the locally strongest R_{12}^{A}. The nature of the coupling between nanowires for R_{ij}^{S} and R_{ij}^{A} is still unknown. But according to devices with d ranging from 40 nm to 1.5 μm, both R_{ij}^{S} and R_{ij}^{A} persist over large separations and are nearly independent of d (Figure 33 (b)). Since the $e^{-4k_F d}$ behavior is not observed in both R_{ij}^{S} and R_{ij}^{A}, where $k_F \sim(10\mathrm{nm})^{-1}$ is the Fermi wave vector, the Coulomb coupling can be ruled out as the dominating effect [122].

4.3.3 Frictional drag between a superconducting and a normal-state nanowire

We examine the drag resistance from devices with one superconducting nanowire and one normal nanowire to corroborate that the symmetric component of drag resistance is related to the superconducting-normal transition in the drive nanowire. The superconducting properties of LAO/STO are known to be gate-tunable both in 2D geometries [124] and in 1D [157, 112]. There are known inhomogeneities in electron density which most likely arise from the underlying ferroelastic domain structure [106]. While we cannot independently control the carrier density of one nanowire while keeping the second fixed, we can select devices in which one nanowire shows superconducting behavior and the other does not. Figure 34 shows the typical data from Device 2J. As illustrated in Figure 34 (a), green-colored nanowires are superconducting, while black nanowires are in the normal-state. The information about the state of the nanowires is inferred from two-terminal resistance measurements (Figure 34 (b)). We then can compare the frictional drag as sensed by nanowire 1 due to two configurations–one in which one device contains a superconducting section and one in which the other does not.

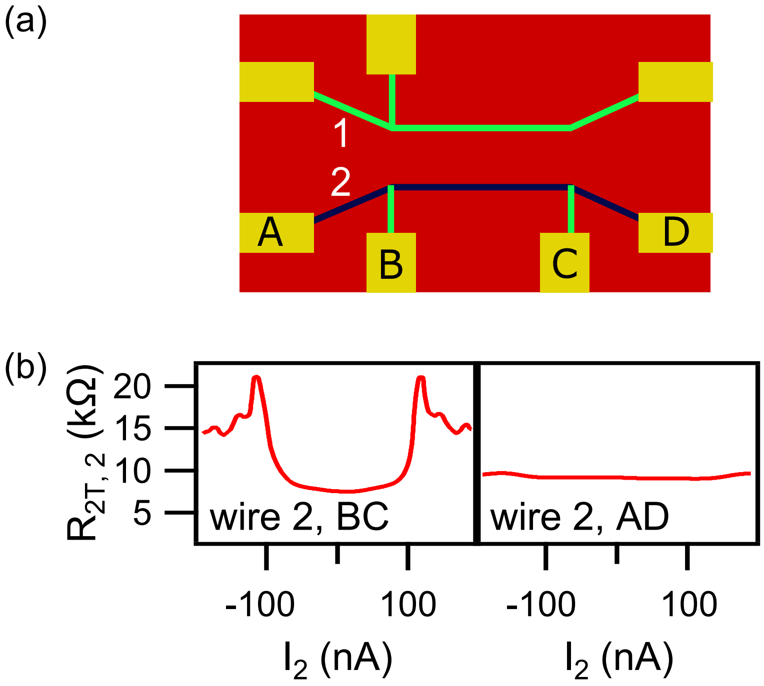

Figure 34: Schematic of frictional drag between one superconducting and one normal-state nanowire. (a) Schematic of the device with normal-state nanowire. Black sections in nanowire 2 are normal; green sections in nanowire 2 and 1 are superconducting. (b) Left: Two-terminal resistance of nanowire 2 measured between B and C. Superconductivity arises from the green portions as shown in panel (a). Right: Two-terminal resistance of nanowire 2 between A and D where the whole nanowire is in the normal-state.

4.3.3.1 Normal-state nanowire as the drive nanowire

First, we consider the configuration where superconducting nanowire 1 is the drag nanowire and examine the influence of drive nanowire's state on drag resistance, as shown in Figure 35 (a). When both the drive and drag nanowires are superconducting, the drag resistance R_{12} is asymmetric with a large symmetric component (Figure 35 (b) left). However, when the drive nanowire is normal, the drag resistance is mostly anti-symmetric with a negligible symmetric component (Figure 35 (b) right).

The symmetric component of drag resistance showing up around the superconducting-

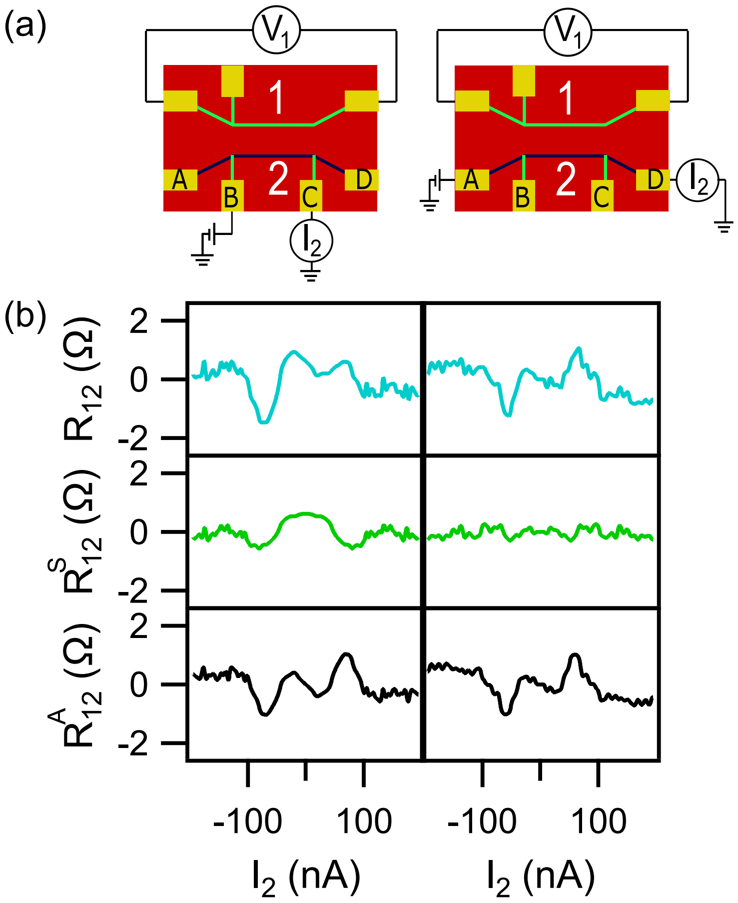

Figure 35: Frictional drag with a superconducting drag nanowire and a normal-state drive nanowire. (a) Measurement configurations when nanowire 2 is used as the drive nanowire. (b) From top to bottom panels: Drag resistance R_{12}, its symmetric and anti-symmetric components R_{12}^{S} and R_{12}^{A}. Left and right panels correspond to the measurement configurations in (a).

normal transition in the drive nanowire can be explained by the rectification of the thermal noise in the drive nanowire [85]. When a superconducting nanowire undergoes a superconducting-normal transition, the nanowire's resistance increases. This process generates thermal energy, which in turn gives rise to a large thermal noise and a greatly enhanced symmetric component of drag resistance. For the normal nanowire, therefore there is no significant enhancement of the thermal noise, and the symmetric component of drag resistance remains small at all biases across the drive nanowire.

The rectification of thermal noise in the drive nanowire also explains the strong correlation between R^{A}_{12} and R^{S}_{12}. R^{A}_{12} comes from the rectification of the shot noise in the drive nanowire [148]. Shot noise is a non-equilibrium phenomenon depending on the voltage bias across the drive nanowire [85]. During the superconducting-normal transition in the drive nanowire, the change of drive nanowire's resistance changes the bias across different portions of the nanowire, thus inducing quantum shot noise and the anti-symmetric drag resistance is observed simultaneously with the symmetric drag resistance.

4.3.3.2 Normal-state nanowire as the drag nanowire

The symmetric component in drag resistance is also strongly suppressed when the drag nanowire is in the normal-state. As shown in the left panel of Figure 36 (a), when the drag resistance is measured between B and C of nanowire 2, the drag resistance R_{21} is asymmetric with a large symmetric component (Figure 36 (b) left). However, when the drag resistance is measured between A and D, the drag resistance is anti-symmetric with a negligible symmetric component (Figure 36 (b) right). Since the drive nanowire 1 is superconducting in both configurations, the absence of the symmetric drag resistance component with a normal drag nanowire cannot be ascribed to the absence of thermal noise in the drive nanowire. The fact that the symmetric drag resistance measured from a superconducting drag nanowire is larger may be explained by the symmetric drag resistance depends on the electron-hole asymmetry in the drag nanowire [104], and the electron-hole asymmetry is stronger in superconducting nanowire than normal nanowire. Electron-hole symmetry is more easily broken in low-dimensional devices [102, 85]. It is reported that the superconductivity at the LAO/STO interface is 1D in nature, situated at the boundary of the nanowire, and is absent within the interior region of the nanowire [112]. Thus the overall dimension of the nanowire is reduced as it becomes superconducting compared to a normal nanowire due to the formation of the 1D superconducting boundary. This reduced dimension of the nanowire gives rise to a stronger electron-hole asymmetry. Therefore the symmetric component of drag resistance is stronger

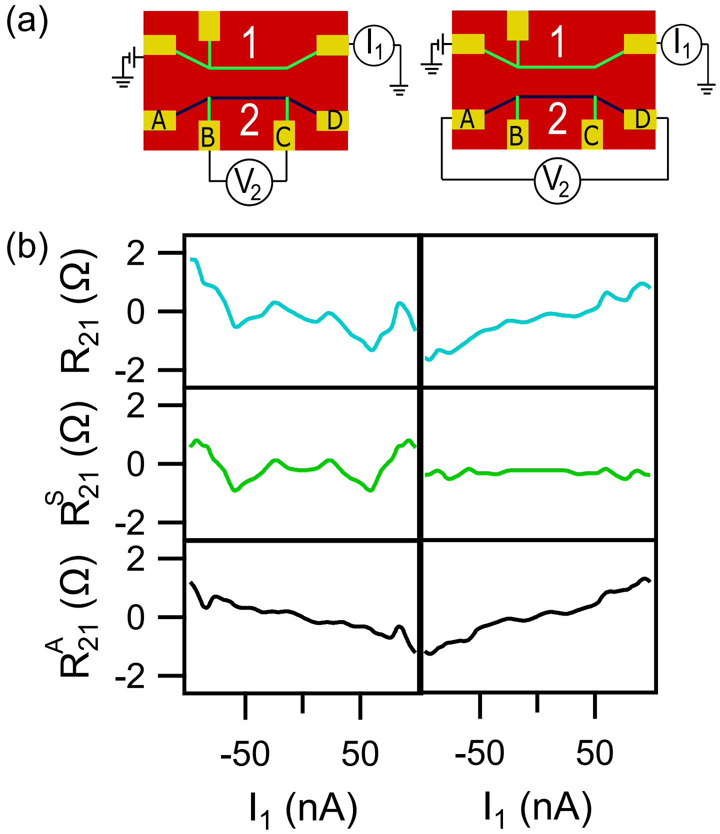

Figure 36: Frictional drag with a superconducting drive nanowire and a normal-state drag nanowire. (a) Measurement configurations when nanowire 2 is used as the drag nanowire. (b) From top to bottom panels: Drag resistance R_{21}, its symmetric and anti-symmetric components R^{S}_{21} and R^{A}_{21}. Left and right panels correspond to the measurement configurations in (a).

when it is measured in a superconducting drag nanowire.

4.4 Conclusion

In summary, frictional drag between superconducting LAO/STO nanowires exhibits a strong and highly symmetric component in drag resistance, which is distinct from the anti-symmetric drag resistance between LAO/STO nanowires in the normal-state. The symmetric component arises from the rectification of thermal noise in the drive superconducting nanowire based on the fact that it shows up at the vicinity of superconducting-normal transition in the drive nanowire and disappears when the drive nanowire is normal. The symmetric component in drag resistance also disappears when the drag nanowire is normal, which can be attributed to the 1D nature of superconductivity in LAO/STO systems.

5.0 Frictional Drag between $LaAlO_3/SrTiO_3$ Nanowires and Electron Waveguides

5.1 Introduction

Frictional drag experiments described in Chapters 3 and 4 are performed with regular nanowires with multiple conducting channels in the high magnetic field or superconducting regimes. A better understanding and control of nanowires in the frictional drag experiment can be beneficial. One of the most important advancements in the lab is the capability of fabricating electron waveguides which exhibit quantized ballistic transport and the subband structure is well understood by lateral and vertical spatial quantum numbers as well as the spin degree of freedom. The conductance of the electron waveguide can be tuned by side gate voltages to populate different subbands, which may allow to gain access to the real 1D regime and achieve a Luttinger liquid. Previously in semiconductor systems, frictional drag experiments between ballistic quantum nanowires with quantized conductance have shown drag signals correlated with the subband structure and are attributed to the enhanced electron-hole asymmetry when a new subband is populated [81, 32]. By tuning the conductance of a quantum nanowire below the first conductance plateau, the drag resistance is found to increase as the temperature decreases, which suggests the formation of a Luttinger liquid in the quantum wire [82].

Frictional drag with electron waveguides at the $LaAlO_3/SrTiO_3$ interface can be more interesting because of the attractive electron-electron interaction and exotic Pascal electron liquid phase showing up in the electron waveguide. In this chapter, we present frictional drag experiments between a regular nanowire and an electron waveguide. Frictional drag with a short electron waveguide is qualitatively similar to the frictional drag between two regular nanowires in both high magnetic field and superconducting regimes. The correlation between the frictional drag and long electron waveguide is observed when the long electron waveguide is used as the drag nanowire. However, when the long electron waveguide is used as the drive nanowire, no correlation is observed between the frictional drag and the subband structure.

5.2 Experimental Methods

Figure 37 shows the schematic of a frictional drag device involving one electron waveguide and one regular nanowire. The device also consists of a round shape side gate which applies voltage V_{sg} to tune the chemical potential μ of the electron waveguide. The main reason why devices with two parallel electron waveguides are not written is that the side gate tunes both electron waveguides simultaneously therefore we can not control the chemical potential of each electron waveguide independently. As a result, the device with coupled electron waveguides usually operates at a state where one electron waveguide is in the quantized conductance regime ($G \sim 1e^2/h$) while the other one is highly conducting ($G \gg 2e^2/h$) functioning like a regular nanowire. Therefore we focus on the device with one electron waveguide and one regular nanowire instead. The electron waveguide is defined to be wire 1 and the regular nanowire is defined to be wire 2 with corresponding lengths L_1 and L_2. Data presented in this chapter comes from two devices. Device 1 has a short electron waveguide $L_1 = 400$ nm and a regular nanowire $L_2 = 800$ nm with a separation of $d = 600$ nm. The regular nanowire of Device 2 has the same length as Device 1 namely $L_2 = 800$ nm but with longer electron waveguides. Parameters for Device 2 are $L_1 = 4.5$ μm and $d = 1$ μm.

The measurement is performed by sourcing current in one nanowire and measuring the induced voltage in the other nanowire. Use the measurement configuration in Figure 37 as an example. Since the electron waveguide is defined to be wire 1 and the regular nanowire is defined to be wire 2, when applying a voltage $V_{\mathrm{S1}} = V_{\mathrm{DC}} + V_{\mathrm{AC}} \cos(\omega t)$ on the electron waveguide, the resulting AC components current $I_1(\omega)$ and induced voltage $V_2(\omega)$ at frequency ω are measured using a lock-in amplifier. Thus $R_{21} = V_2(\omega)/I_1(\omega)$ is the drag resistance measured from the regular nanowire and $R_{11} = V_1(\omega)/I_1(\omega)$ is the four-terminal resistance of the electron waveguide. By varying V_{DC}, R_{21} and R_{11} can be expressed as a function of the DC component in drive currents I_1. In order to ensure that the drag resistances R_{ij} are not influenced by current leakage between the electron waveguide and regular nanowire,

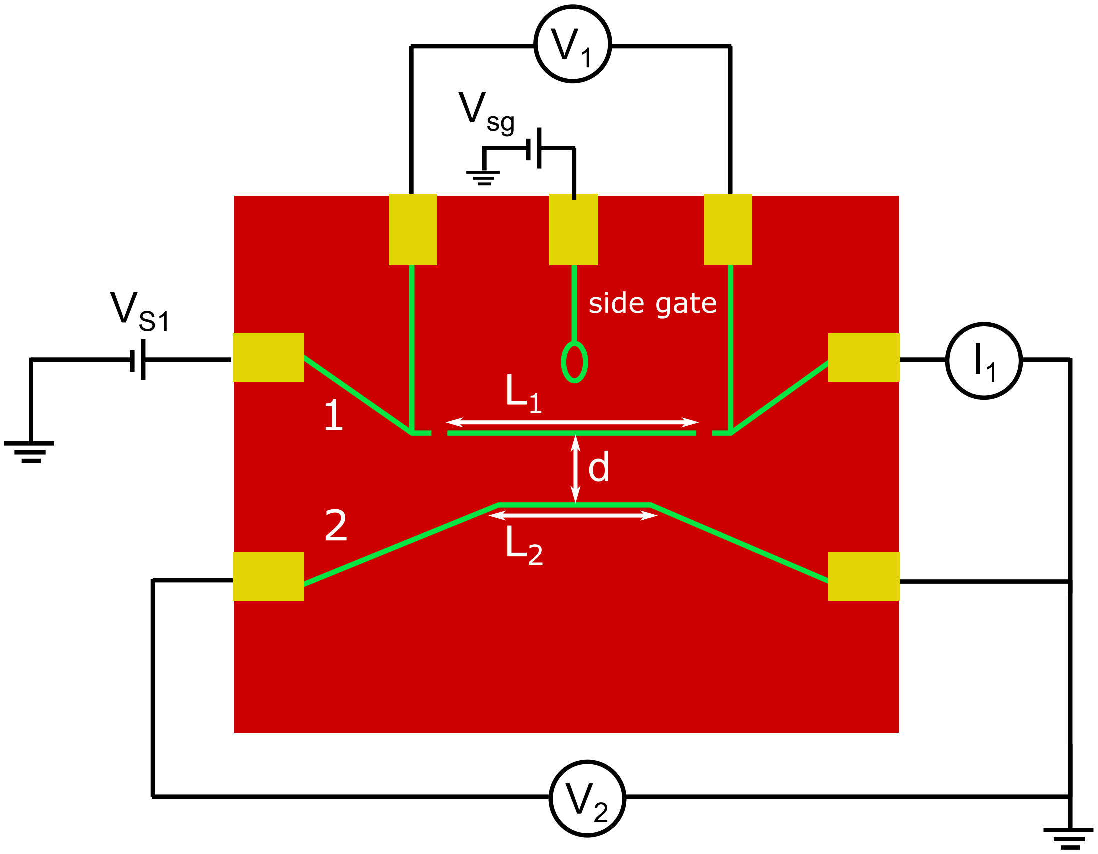

Figure 37: Schematic of frictional drag between one electron waveguide and one regular nanowire. The electron waveguide is defined to be wire 1 and the regular nanowire is defined to be wire 2. Correspondingly, the length of the electron waveguide is L_1 and the regular nanowire L_2. The separation between them is d. The chemical potential of the electron waveguide is tuned by the side gate voltage V_{sg}. In the figure, the current I_1 is sourced in the electron waveguide by voltage V_{S1}. The four-terminal voltage across the electron waveguide is V_1 and the induced drag voltage measured from the regular nanowire is V_2.

all measurements are performed well below the inter-wire breakdown voltage ($\sim$ 10 mV) measured for each device. All experiments are performed at a temperature $T < 100$ mK.

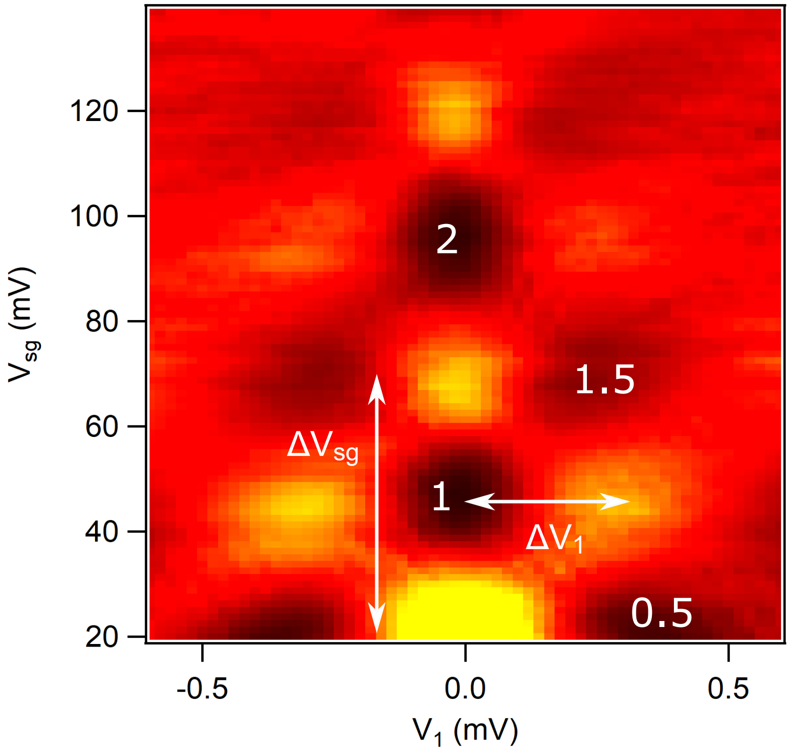

Figure 38: Finite bias transconductance analysis. The data shown here comes from Device 2. Dark areas mark the conductance plateau. Quantized conductance numbers are labeled accordingly. Bright areas mark where a subband opens. The lever-arm ratio $\alpha = e\Delta V_{\text{sd}}/\Delta V_1$. Here $\Delta V_{\text{sd}} = 300$ μV and $\Delta V_1 = 52.5$ mV.

The gate voltage V_{sg} can be converted to the chemical potential μ by the lever-arm α, which can be obtained through the finite-bias transconductance data. I-V curves are taken under different V_{sg} across the electron waveguide. At each V_{sg}, the four-terminal conductance $G_{11} = dI_1/dV_1$ of the electron waveguide can be obtained as a function of the four-terminal voltage V_1 across the electron waveguide. As shown in Figure 38, the transconductance at different biases V_1 can be obtained from dG_{11}/dV_{sg}. Lever-arm $\alpha = e\Delta V_{\text{sg}}/\Delta V_1$, where the four-terminal voltage difference ΔV_1 and the side gate voltage ΔV_{sg} difference mark the same transition between adjacent bands. α of Device 1 is around 4.17 μeV/mV and α of Device

2 is around 5.71 μeV/mV.

5.3 Results and Discussion

5.3.1 Frictional drag with the short electron waveguide

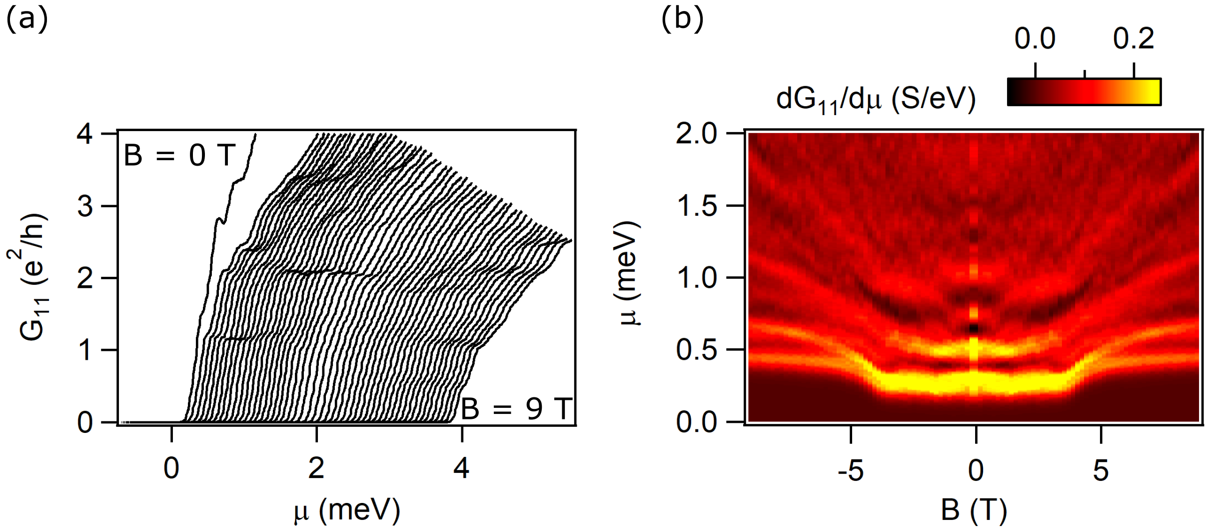

Figure 39: Four-terminal conductance and transconductance of the short electron waveguide from Device 1. (a) Zero-bias four-terminal conductance G_{11} of Device 1 as a function of chemical potential μ. B ranges from 0 to 9 T. (b) Transconductance $dG_{11}/d\mu$ as a function of B and μ. The bright band marks the crossing of a subband and the dark area marks the conductance plateau

Device 1 has a short electron waveguide with $L_1 = 400$ nm. The four-terminal conductance G_{11} and transconductance $dG_{11}/d\mu$ are shown in Figure 39. Figure 39 (a) displays G_{11} from $B = 0$ T to 9 T with an interval of $B = 0.18$ T. The conductance is larger at $B = 0$ T due to the superconductivity. At -9 T, the first spin-polarized conductance plateau shows up at $\sim 0.5\ e^2/h$ instead of $1\ e^2/h$. This suggests the existence of backscattering processes. The subband structure of the electron waveguide is captured by examining $dG_{11}/d\mu$. Bright band marks the Fermi energy crossing a subband and the dark area marks the conductance plateau. We can see subbands get populated as the chemical potential of the electron waveguide increases and electrons remain pair until $B = 5$ T.

To explore the effect of the subband structure, we first study the frictional drag as a function of μ. Figure 40 shows the frictional drag as a function of μ at $B = 9$ and 0 T. At $B = 9$ T, the negatively saturated R_{12} below ~ 0.4 meV shows up when the electron waveguide is not conducting and still in a pinch-off state therefore frictional drag does not exist. As μ increases, R_{12} is anti-symmetric (Figure 40 (a) bottom panel) through the whole μ range during the experiment without much variation as a function of μ. The anti-symmetric drag resistance is qualitatively the same as what is observed between two regular nanowires in the high magnetic field regime ($B > -0.2$ T) and is attributed to the rectification of quantum shot noise in the drive nanowire by the broken symmetry in the drag nanowire [148]. Two representative R_{12} line profiles at $I_2 = 0$ and 32 nA are picked to compare with the transconductance $dG_{11}/d\mu$ of the electron waveguide. However, it is hard to find the correlation between R_{12} and the subband structure represented by $dG_{11}/d\mu$ partly due to the smallness of R_{12}. The frictional drag with the electron waveguide as the drive nanowire is also explored, as shown in Figure 40 (b). Similar to R_{12} shown in Figure 40 (a), R_{21} is also anti-symmetric through the whole μ range without much variation as a function of μ except R_{21} is larger at low μ. The larger R_{21} at low μ is expected since drag resistance tends to be larger when either the drive or drag nanowire is more resistive according to Eq. 3. According to R_{21} at DC current $I_1 = 0$ and 68 nA, R_{21} does not show much correlation with the subband structure of the electron waveguide as well. Therefore, the phenomenon that the drag resistance peaks when the chemical potential crosses a subband bottom in the drive quantum wire is not observed as reported in earlier experiments [33, 81].

Frictional drag as a function of μ is also studied at $B = 0$ T from Device 1 (Figure 40 (c, d)). The negatively saturated R_{12} below 0.2 meV shows up when the electron waveguide is not conducting. Both R_{12} and R_{21} are asymmetric with respect to the sourcing current, similar to the frictional drag between regular superconducting nanowires. Asymmetric drag resistance consists of symmetric and anti-symmetric components. The symmetric drag resistance component, which is not observed in the high magnetic field regime, is ascribed to

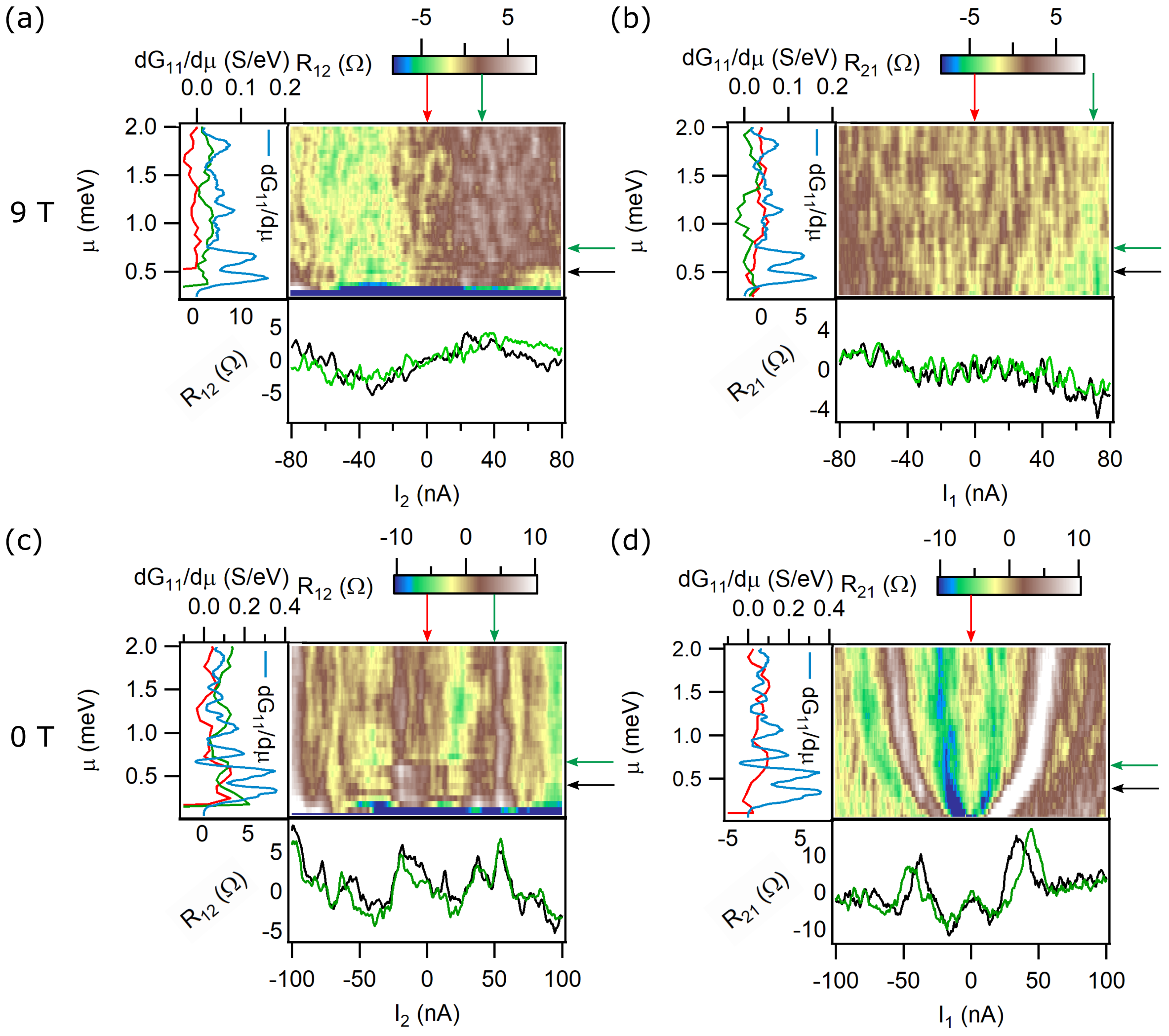

Figure 40: Frictional drag as a function of μ from Device 1 with a short electron waveguide device. (a) and (b) are measured at 9 T. (c) and (d) are measured at 0 T. (a), (c) R_{12} measured from the electron waveguide at 9 and 0 T, respectively. Bottom panel: Representative line profiles of R_{12} as a function of I_2 at values of μ pointed by horizontal arrows of the corresponding color. Left panel: Zero-bias $dG_{11}/d\mu$ (blue) at the corresponding B and line profiles of R_{12} as a function of μ at I_2 pointed by vertical arrows of the same color. The red arrow points to the zero sourcing current. (b), (d) R_{21} measured from the regular nanowire.

the rectification of thermal noise around the superconducting-normal transition in the drive nanowire [147]. R_{12} as a function of μ is different when $\mu < 0.75$ meV. This is manifested when comparing line profiles of R_{12} at $I_2 = 0$ and 50 nA with $dG_{11}/d\mu$. Below 0.75 meV, R_{12} shows some correlation with the subband structure. However, from the intensity graphs in Figure 40 (c), the rest of R_{12} when $\mu > 0.75$ meV and R_{21} shows the same drag resistance features through the whole range of μ without much correlation with the subband structure of the electron waveguide.

Besides sweeping μ at different B, sweeping B at different μ is also performed to study the subband structure effect on the frictional drag (Figure 41). $\mu = 0.50$ and 1.74 meV are picked corresponding to $G_{11} = 0.5$ and 2 e^2/h at $B = 9$ T. Both R_{12} and R_{21} are magnetically tunable and anti-symmetric with respect to the sourcing current (bottom panels in Figure 41). R_{12} and R_{21} at different μ show little variation despite the change of drag resistance's magnitude. The drag resistance is smaller at $\mu = 1.74$ meV compared to $\mu = 0.50$ meV because both the electron waveguide and the regular nanowire are more conducting. By comparing R_{12} and R_{21} at different biases with $dG_{11}/d\mu$ (left panels in Figure 41), no clear correlation is observed between the drag resistance and the subband structure of the electron waveguide, whether it is used as the drive or drag nanowire.

Overall, the frictional drag observed between a short electron waveguide and a regular nanowire is qualitatively the same as what is observed between two regular nanowires and is independent of the subband effect of the electron waveguide. However, this is not surprising because the frictional drag at the $LaAlO_3/SrTiO_3$ interface is not sensitive to the separation between two nanowires [148, 147]. The insensitivity to the interwire separation suggests the frictional drag depends on the whole nanowire ~ 30 μm including leads, instead of only the nanowire or the electron waveguide ~ 1 μm in the main device section.

5.3.2 Frictional drag with the long electron waveguide

Due to the shortness of the electron waveguide, it is hard to tell the contribution of the electron waveguide from the influence of the leads. Therefore, the frictional drag with a long electron waveguide is also performed whose electrical transport property is more determined

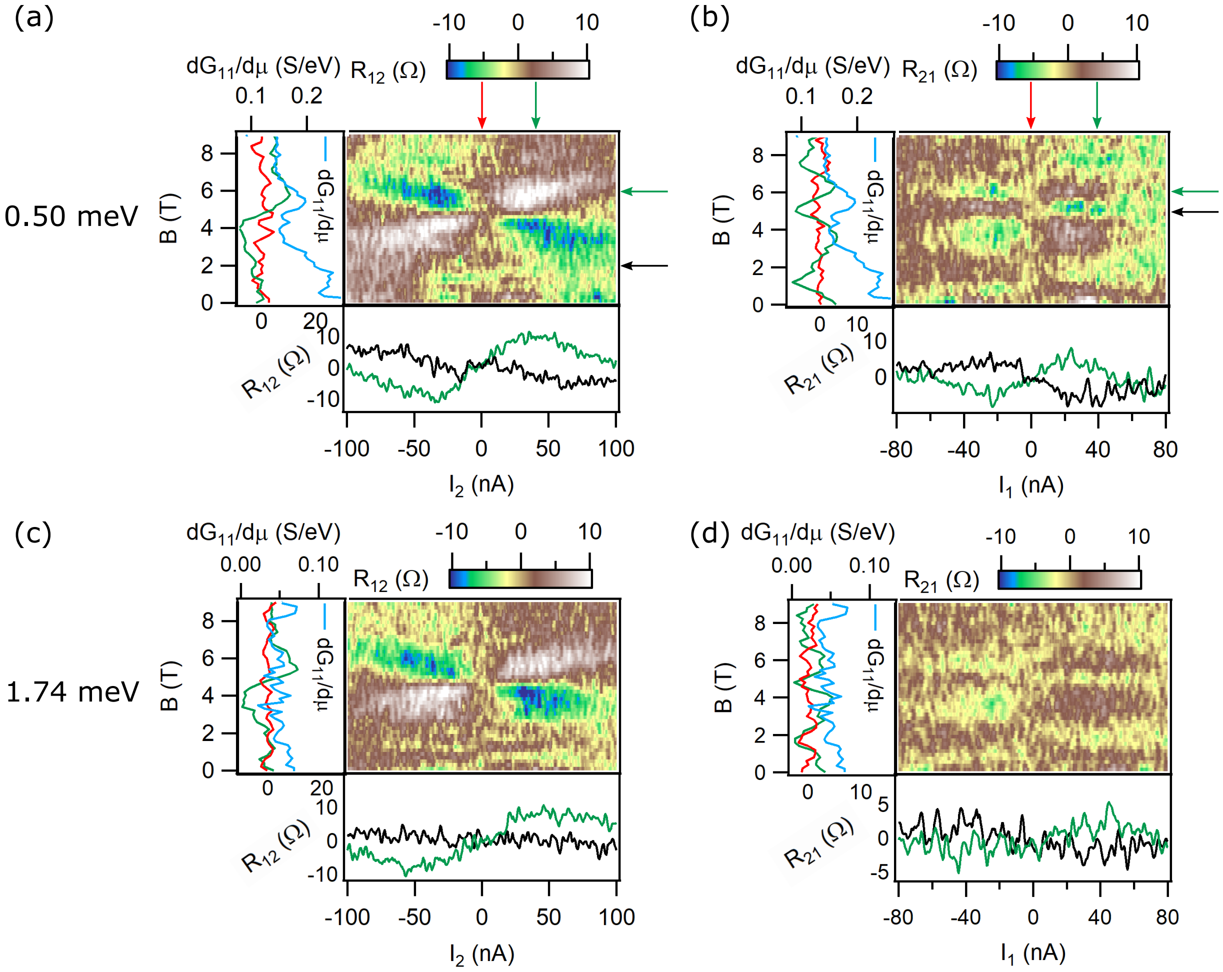

Figure 41: Frictional drag as a function of B at $\mu = 0.50$ meV and 1.74 meV from Device 1 with a short electron waveguide device. (a), (c) R_{12} measured from the electron waveguide at $\mu = 0.50$ meV (a) and 1.74 meV (c). Left panel: Line profiles of R_{12} at $I_2 = 0$ (red) and 40 nA (green) compared with $dG_{11}/d\mu$ at the corresponding μ (blue). Bottom panel: Line profiles of R_{12} at $B = 6$ (green) and 2 T (black). (b), (d) R_{21} measured from the regular nanowire at $\mu = 0.50$ meV (b) and 1.74 meV (d). Left panel: Line profiles of R_{12} at $I_2 = 0$ (red) and 40 nA (green) compared with $dG_{11}/d\mu$ (blue). Bottom panel: Line profiles of R_{12} at $B = 6$ (green) and 2 T (black).

by the electron waveguide due to the larger length. In the long electron waveguide frictional drag experiment, the length L_2 of the regular nanowire is kept unchanged and the same as the frictional drag with a short electron waveguide. First, since the frictional drag is separation independent, it is not necessary to make the parallel part of the regular nanowire the same length as the electron waveguide. Second, the longer regular nanowire makes the parallel part longer and it is more likely to cause leakage between the electron waveguide and the regular nanowire.

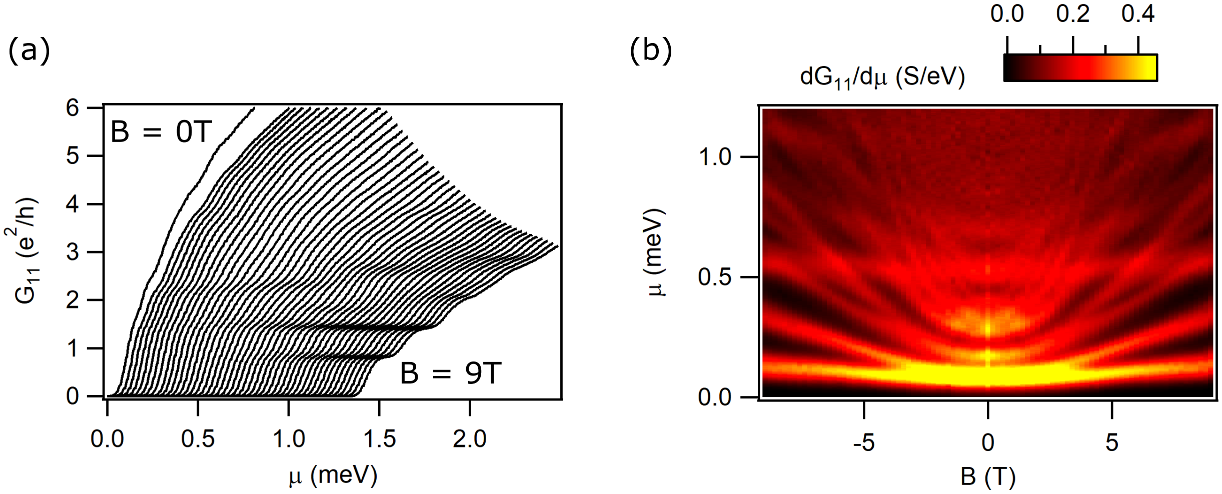

Figure 42: Four-terminal conductance and transconductance of the long electron waveguide from Device 2. (a) Zero-bias four-terminal conductance G_{11} of Device 2 as a function of chemical potential μ. B ranges from 0 to 9 T. (b) Transconductance $dG_{11}/d\mu$ as a function of B and μ.

Due to the advancement of the electron waveguide fabrication technique, the electron waveguide as long as ~ 10 μm can be written which presents well-observed quantized conductance plateaus. The electron waveguide in Device 2 is 4.5 μm. Figure 42 (a) shows G_{11} from $B = 0$ T to 9 T as a function of μ. At 9 T, the first plateau shows up at $G_{11} = 0.8$ e^2/h and the second one at 1.5 e^2/h. Despite the imperfect quantized conductance value, the subband structure in the transconductance $dG_{11}/d\mu$ as a function of B and μ is well resolved with high contrast between bright bands and dark areas throughout the whole measurement range (Figure 42).

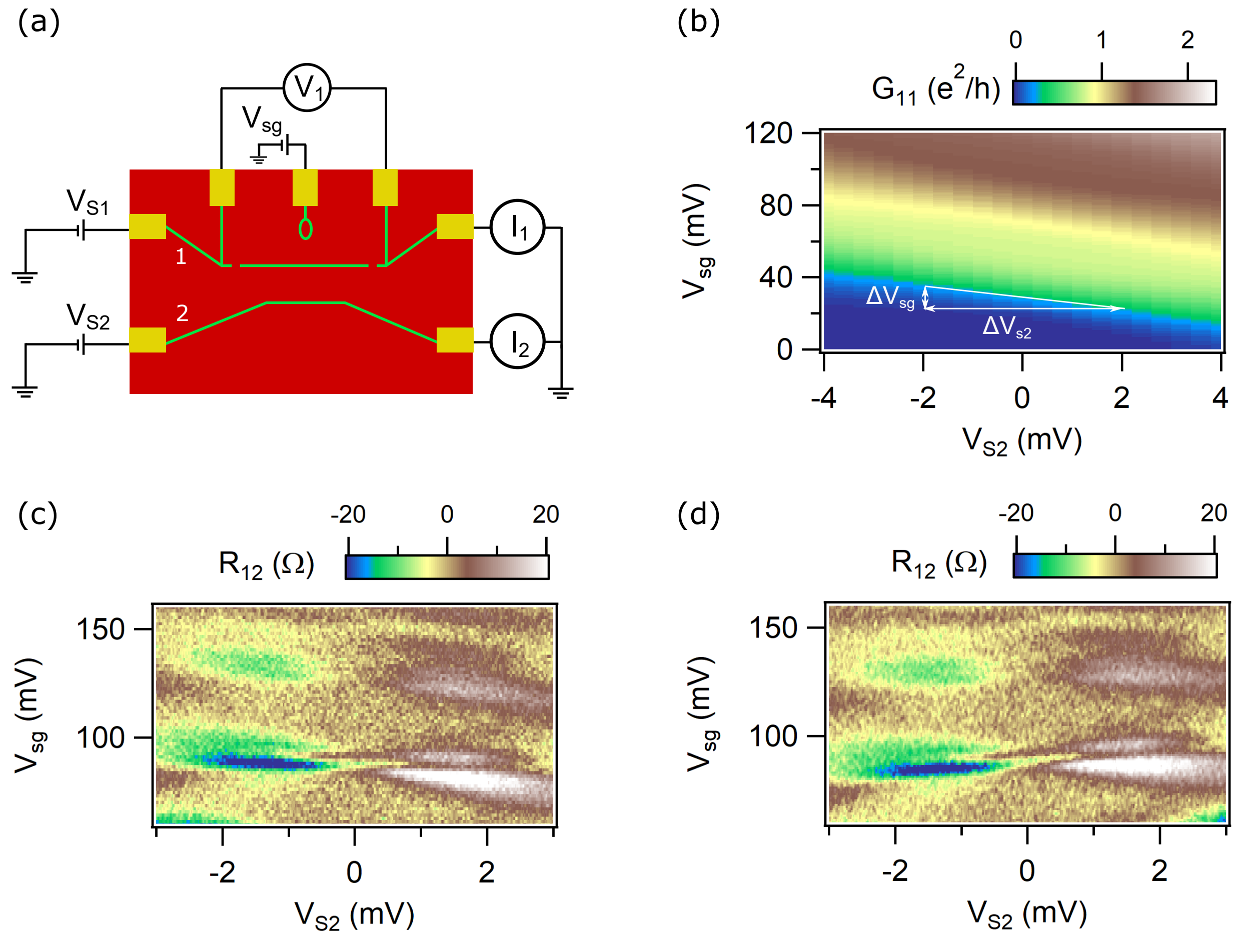

Figure 43: Gating voltage ratio of the long electron waveguide frictional drag. (a) Experimental configuration for the gating voltage ratio β characterization. (b) Four-terminal conductance G_{11} of the electron waveguide as a function of V_{sg} and V_{S2}. β is the slope of the white line with equal G_{11} given by $\beta = \Delta V_{\text{sg}}/\Delta V_{\text{S2}}$. (c) Drag resistance R_{12} as a function of V_{sg} and V_{S2} before correction. (d) R_{12} after the correction.

As shown in Figure 43 (c), the drag resistance in the long electron waveguide frictional drag is anti-symmetric but in a tilted direction. This is because both the regular nanowire 2 and the side gate are tunning the chemical potential of the long electron waveguide as they apply voltages during the experiment. A positive bias applied across the regular nanowire increases the chemical potential of the electron waveguide and can be offset by a smaller side gate voltage to decrease the chemical potential. Therefore the drag resistance is tilted so that the feature at a positive bias shows up at a smaller side gate voltage compared to the corresponding anti-symmetric feature at a negative bias.

The gating ratio between the side gate and bias across the regular nanowire can be characterized by the experimental configuration shown in Figure 43 (a) which simulates the frictional drag configuration where the regular nanowire 2 is used as the drive nanowire. To characterize the zero-bias conductance of the electron waveguide, $V_{\mathrm{S1}} = V_{\mathrm{AC}} \cos(\omega t)$ is applied with typical $V_{\mathrm{AC}} = 100\ \mu V$. DC voltages are applied and varied on V_{sg} and V_{S2}. The typical four-terminal conductance of the electron waveguide G_{11} as a function of V_{sg} and V_{S2} is shown in Figure 43 (b). The gating ratio can be obtained from the slope of a line with equal G_{11} (white line). The ratio β is calculated as $\beta = \Delta V_{\mathrm{sg}}/\Delta V_{\mathrm{S2}}$, which is around 3.5 for Device 2. The tilted drag resistance (Figure 43 (c)) can be corrected by keeping the V_{sg} of drag resistance at $V_{\mathrm{S2}} = 0$ mV unchanged and shifting the V_{sg} at bias V_{S2} by $\Delta V_{\mathrm{sg}} = \beta V_{\mathrm{S2}}$. As shown in Figure 43 (d), after the correction, the drag resistance becomes anti-symmetric as observed before [148]. All data shown in this section is after the correction.

Figure 44 shows the drag resistance as a function of μ and sourcing current at $B = 9$, 3, and 0 T. First, we focus on the configuration where the electron waveguide is used as the drag nanowire and the regular nanowire is used as the drive nanowire. At $B = 9$ T and 3 T, where there is no superconductivity, R_{12} is antisymmetric with sourcing current I_2 (bottom panels of Figure 44 (a) and (c)). Besides the anti-symmetry with respect to I_2, the magnitude of R_{12} also varies with the chemical potential μ, which is not observed in Device 1 with a short electron waveguide. To further study the μ dependence, a linecut at a chosen non-zero bias (red arrow) is taken to compare with $dG_{11}/d\mu$ at the same B (left panels of Figure 44 (a), (c)). The overall magnitude of R_{12} decreases with increasing μ due to the electron waveguide becoming more conducting. Different from the frictional drag with a short electron waveguide, R_{12} measured from the long electron waveguide is well correlated with $dG_{11}/d\mu$. R_{12} shows a peak when a subband opens and $dG_{11}/d\mu$ reaches a peak; R_{12} becomes zero at the quantized conductance plateau where $dG_{11}/d\mu$ is close to zero and reaches a local minimum. This correlation is not surprising since compared to a short electron waveguide, the transport property of the nanowire between two interface electrodes is more determined by the long electron waveguide. At $B = 0$ T, R_{12} is asymmetric with I_2 and the symmetric component in R_{12} can be observed at $I_2 \sim 110$ nA. The correlation between R_{12} and $dG_{11}/d\mu$ is also observed at $B = 0$ T. The R_{12} is larger at $\mu < 0.2$ meV therefore it is easier to observe the correlation between R_{12} and $dG_{11}/d\mu$. As μ increases, R_{12} decreases and gets close to zero, which makes the correlation with $dG_{11}/d\mu$ difficult to observe.

When the electron waveguide is used as the drive nanowire and the regular nanowire is used as the drag nanowire, the drag resistance R_{21} shows qualitatively the same behavior as observed in the frictional drag with a short electron waveguide. From the horizontal linecuts at selected μ, R_{21} is anti-symmetric with respect to the sourcing current I_1 at $B = 9$ T and 3 T and asymmetric at $B = 0$ T (bottom panels in Figure 44 (b), (d) and (e)). As μ increases, the pattern of R_{21} remains approximately the same despite it expands as the electron waveguide becomes more conducting, resulting in features showing up at larger I_1. R_{21} as a function of μ can be captured from vertical linecuts at zero or non-zero I_1. R_{21} at $I_1 = 0$ nA is around zero throughout the whole μ range while R_{21} at non-zero I_1 shows small and non-zero values which decreases with the increasing μ. As shown in left panels of Figure 44 (b), (d), and (e), no correlation between R_{21} and $dG_{11}/d\mu$ is observed whether at zero or non-zero I_1. Therefore, R_{21} measured with the long electron waveguide being used as the drive wire shows no subband effects.

It is reported that the frictional drag between two quantum wires peaks when a subband opens in either the drive or drag quantum wire [81, 32]. Although R_{12} is observed to peak when a subband opens, R_{21} shows no correlation. This is because while the electron waveguide exhibits quantized ballistic transport, the transport property of a regular nanowire is not ballistic or quantized. Therefore the frictional drag with one electron waveguide and one regular nanowire is not in the regime of the frictional drag between two quantum wires. In fact, despite the correlation between R_{12} and subbands when the long electron waveguide is used as the drag nanowire, overall phenomena observed in the frictional drag between a long electron waveguide and a regular nanowire suggests it is in the same regime as the frictional drag between coupled regular nanowires. The anti-symmetric drag resistance is explained by the rectification of quantum shot noise in the drive nanowire by the broken symmetry in the drag nanowire. Thus the asymmetry of the electron waveguide and the subband structure may be correlated, and the asymmetry reaches a maximum when a new subband opens, resulting in the correlation between R_{12} and the subband structure.

5.4 Conclusion

In summary, frictional drag experiments are performed between an electron waveguide and a regular nanowire. In the frictional drag with a short electron waveguide, no subband effects are observed, no matter when the short electron waveguide is used as the drive or the drag nanowire. In the frictional drag with a long electron waveguide, when the electron waveguide is used as the drag nanowire, the drag resistance shows a correlation with the subband structure; when the electron waveguide is used as the drive nanowire, the drag resistance shows no correlation with the subband structure. Frictional drag experiments can benefit a lot from the capability of tunning two nanowires independently, thus allowing us to explore the regime between two electron waveguides with quantized ballistic transport and even access the real 1D-1D frictional drag regime. One possible route is to increase the separation between two electron waveguides further so that the side gate can tune the closer electron waveguide more effectively without affecting the further electron waveguide.

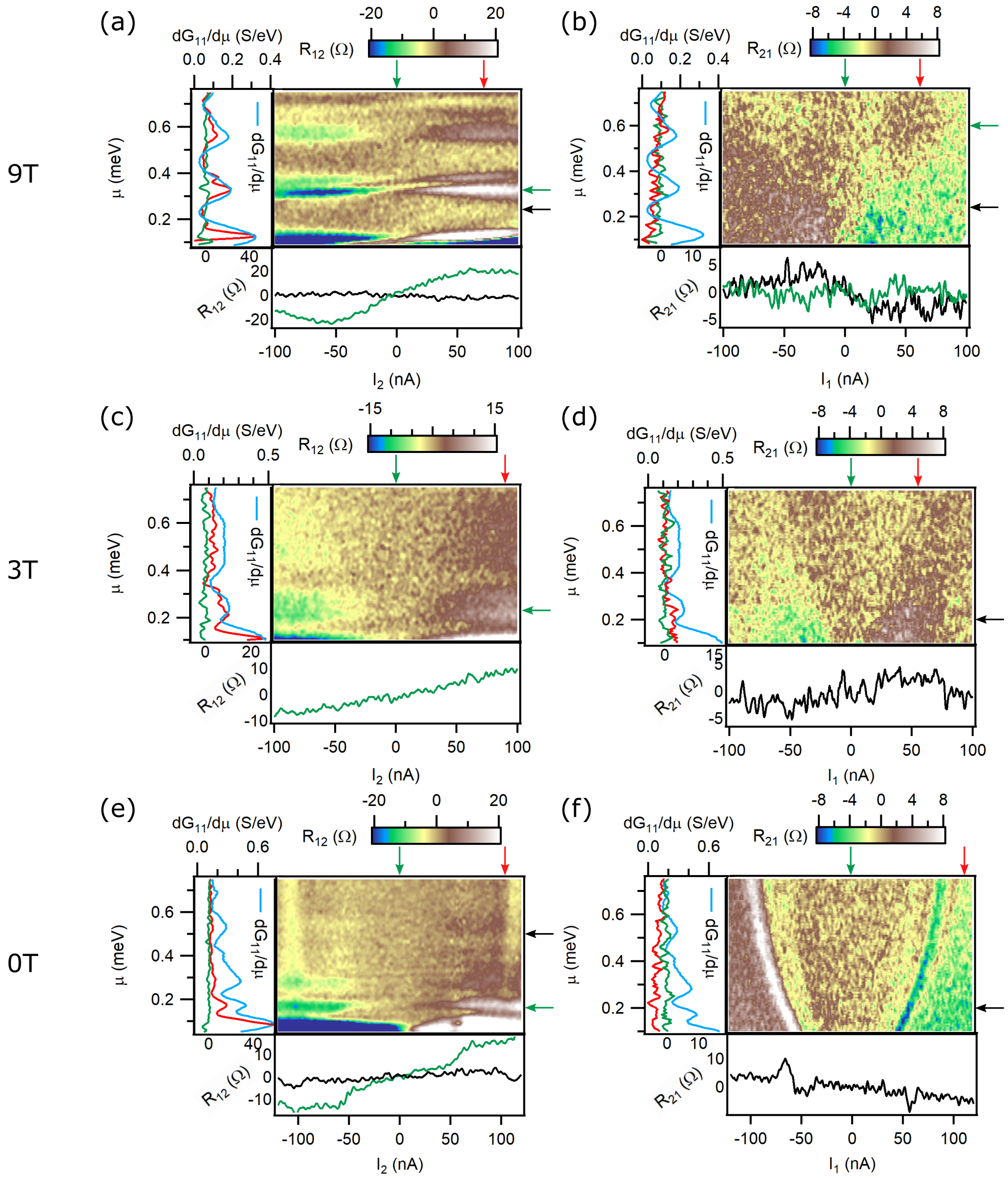

Figure 44: Frictional drag as a function of μ from Device 2 with a long electron waveguide device. The first, second, and third rows are measured at 9, 3, and 0 T, respectively. (a), (c) and (e) R_{12} measured from the electron waveguide. Bottom panel: Representative Line profiles of R_{12} as a function of I_2 at μ pointed by horizontal arrows of the corresponding color. Left panel: Zero-bias $dG_{11}/d\mu$ (blue) at the corresponding B and line profiles of R_{12} as a function of μ at I_2 pointed by vertical arrows of the corresponding color. The green arrow points to the zero sourcing current. (b), (d) and (f) R_{21} measured from the regular nanowire.

6.0 Mott-Limited Thermopower of Pascal Electron Liquid Phases at the $LaAlO_3/SrTiO_3$ Interface

6.1 Introduction

$LaAlO_3/SrTiO_3$ heterostructures exhibit a wide range of physical properties and associated quantum transport phenomena. We investigate the electrical and thermoelectric transport properties of quasi-one-dimensional (1D) electron waveguides at the $LaAlO_3/SrTiO_3$ interface at milli-Kelvin temperatures. We find a highly enhanced and oscillating thermopower for these electron waveguides, with values exceeding 100 μV/K in the electron-depletion regime. The Mott relation, which governs the band term thermopower of non-interacting electrons, agrees well with the experimental findings in and around regimes where strongly attractive electron-electron interactions lead to a previously reported Pascal series of conductance explained by bound states of $n = 2, 3, 4,..$ electrons. These results pave the way for quantized thermal transport studies of emergent electron liquid phases in which transport is governed by quasiparticles with charges that are integer multiples or fractions of an electron.

The heterointerface between the complex oxides $LaAlO_3$ and $SrTiO_3$ provides a highly versatile platform to study electronic correlations in low dimensions. A rich variety of electrically tunable properties have been observed in experiments that probe the behavior in two spatial dimensions, including superconductivity [124, 21], magnetism [17], and tunable spin-orbit interactions [20, 135]. Many unusual aspects of the transport in 2D appear to originate from naturally forming quasi-one-dimensional (1D) ferroelastic domain boundaries [108, 72]. These behaviors include highly anisotropic magnetoresistance, enhanced conductance along ferroelastic domain boundaries, and quantum oscillations whose Luttinger count disagrees sharply with Hall effect estimates of electron density [29]. The importance of quasi-1D transport at the $LaAlO_3/SrTiO_3$ interface has been increasingly realized due to the deployment of various spatially resolved probes, including scanning squid microscopy [72], scanning single-electron transistor microscopy [61], and scanning force microscopy coupled with transport [112].

Artificially created 1D electronic nanostructures have proven useful in teasing out the physics that is due to 1D versus 2D behaviors. Using conductive atomic force microscope (c-AFM) lithography, $LaAlO_3/SrTiO_3$ heterostructures that are on the verge of an insulator-to-metal transition [149] can be made locally conductive by charging the surface (with protons) at room temperature [18]. This form of modulation doping tetragonally distorts the conductive regions, "seeding" the formation of z-oriented ferroelastic domains at low temperatures. This results in conductive nanostructures that exhibit signatures of superconductivity [157], electron pairing outside the superconducting phase [28], ballistic quantized electron transport [1], and other exotic phases in 1D such as a Pascal series of conductance [16] associated with transport governed by bound states of $n = 2, 3, 4, \ldots$ electrons. Further nanoscale engineering of these electron waveguides leads to experimentally observed fractional conductance plateaus, which may be signatures of electron fractionalization.

Thermal transport techniques offer opportunities for obtaining further insights into the full phase diagram of these rich 1D systems. Here we describe thermopower measurements of electron waveguides which show ballistic transport and also exhibit signatures of a Pascal series of conductance steps associated with strong, attractive electron-electron interactions. We find a highly enhanced and oscillating thermopower with values exceeding 100 μV/K in the electron-depletion regime. The thermopower is directly correlated with the subband structure of the electron waveguide and well described quantitatively by the Mott relation with no adjustable parameters. Our findings set the stage for thermal conductance measurements which may be able to quantitatively measure the charge of emergent Pascal phases.

6.2 Experimental Methods

The electron waveguides are fabricated at the $LaAlO_3/SrTiO_3$ interface using c-AFM lithography. With 3.4 unit cells of $LaAlO_3$ grown on the TiO_2-terminated $SrTiO_3$ substrate, the $LaAlO_3/SrTiO_3$ interface is initially insulating. The interface is contacted electrically by depositing titanium and gold in lithographically defined areas that are etched below the $LaAlO_3/SrTiO_3$ interface, as illustrated in Figure 45 (b). Positive voltages applied between the c-AFM tip and the $LaAlO_3/SrTiO_3$ interface locally protonate the top $LaAlO_3$ surface and accumulate conducting electrons in $SrTiO_3$ near the $LaAlO_3/SrTiO_3$ interface, thus defining the nanowire for electron conduction, while negative voltages locally restore the insulating phase, as illustrated in Figure 45 (a, b). The sketched quantum wire system consists of a main channel. The nominal width of the main channel is $w = 10$ nm quantified by erasure experiments [22] and the total length is $L_c = 1.2$ μm, contacted by five terminal leads and one side gate. The main channel contains two narrow barriers (with nominal width $L_B = 10$ nm) that are separated by a distance of $L_s = 0.6$ μm, as illustrated in Figure 45 (c). The side gate supplies a controlled voltage V_{sg} that tunes the chemical potential μ of the quantum wire and the number of accessible quantum channels. Note that the two barriers with appropriate widths are essential to make the chemical potential of the quantum wire tunable by the side gate voltage, which would otherwise be impossible if there is only one or none of the barriers, or the barriers are either too wide or too narrow. The relationship between V_{sg} and μ, governed by the so-called lever-arm ratio $\alpha \equiv d\mu/dV_{\mathrm{sg}}$, is determined as $\alpha = 8 \pm 0.2$ μeV/mV for our Device A and 6.4 ± 0.2 μeV/mV for our Device B through the analysis of non-equilibrium conductance. Novel properties such as electron pairing without superconductivity [28], tunable electron-electron interactions [29], and Shubnikov-de Haas-like quantum oscillations [26] have previously been revealed by studying quantum transport in similarly designed nanostructures.

The four-terminal electrical conductance G of the quantum wire is first measured at a temperature of $T = 80$ mK as a function of the side gate voltage V_{sg} and corresponding chemical potential μ, in magnetic fields ranging from -9 T to 9 T. Specifically, as illustrated in Figure 45 (c), a sinusoidal source voltage of $V_{\mathrm{S}} \sin(\omega t)$ with $V_{\mathrm{S}} = 100$ μV and $\omega/2\pi = 3.156$ Hz is supplied on terminal 1 while terminal 2 acting as the drain is grounded; the amplitudes of both the alternating current on terminal 2 (I_2) and the voltage difference between terminals 3 and 4 ($V_{4\mathrm{T}}$) at the same frequency ω are measured using a lock-in amplifier. The conductance of the quantum wire is determined as $G = dI/dV = I_2/V_{4\mathrm{T}}$.

The thermopower (the absolute value of Seebeck coefficient S) of the same quantum wire is through a different experimental configuration, see Figure 45 (d). The thermopower is defined as the electric field generated by a temperature gradient in the absence of any charge

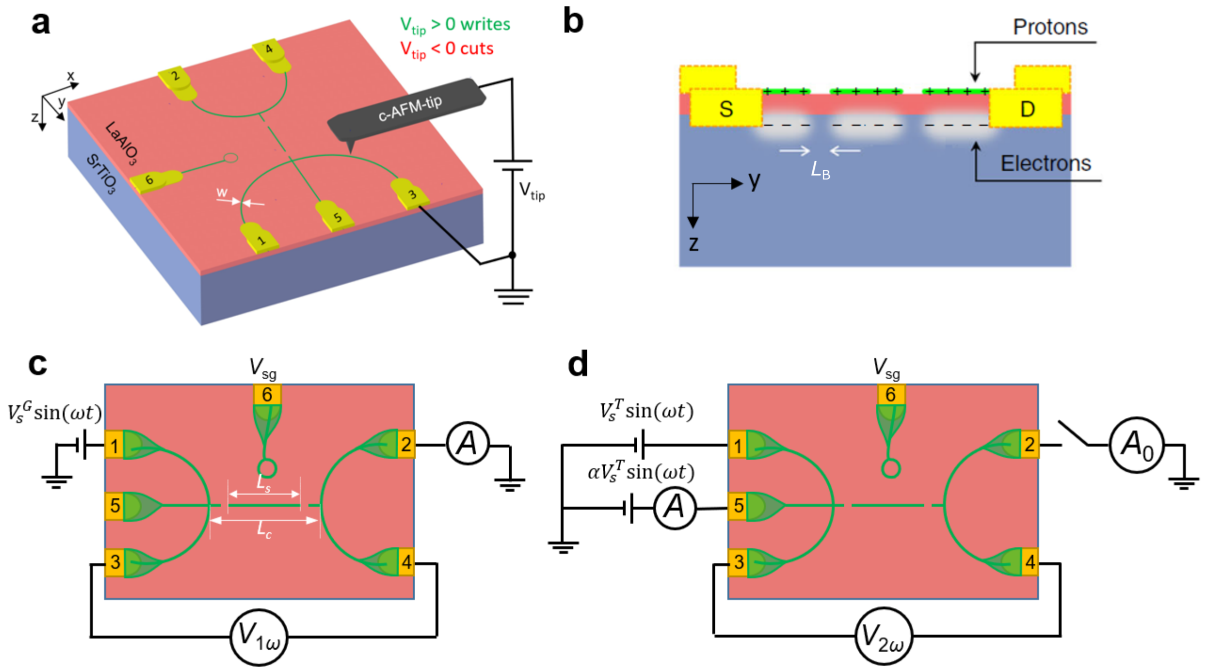

Figure 45: Schematics of the experimental device and measurement configurations. (a) Schematic diagram of the four-terminal quantum nanowire at the interface of LaAlO$_3$/SrTiO$_3$ heterostructure created using conductive atomic force microscope (c-AFM) lithography. (b) A side view of the sample showing the c-AFM-sketched quantum nanowire located at the interface of the LaAlO$_3$/SrTiO$_3$ heterostructure. (c, d) Experimental designs for the four-terminal conductance and thermopower measurements, respectively.

current. To measure the thermopower, a temperature difference ΔT is generated between two ends of the quantum wire by applying a sinusoidal source voltage of $V_S \sin(\omega t)$ to terminal 1 and another voltage of $aV_S \sin(\omega t)$ to terminal 5, with $V_S = 100\mu V$, $\omega/2\pi = 3.156$ Hz, and a being finely tuned so that no current can flow through the quantum wire even when the quantum wire is conductive and terminal 2 is grounded, as shown in Figure 45 (d). We thus have supplied a heating current at frequency ω flowing from terminal 1 to terminal 5 without superimposing any potential difference between the two ends of the quantum wire. This current at frequency ω generates an alternating heat source at frequency 2ω on the left side of the quantum wire due to Joule heating ($P = I^2R$), which in turn induces a temperature modulation at the same frequency 2ω on the left side of the quantum wire. Terminal 2 is kept floating so that no closed-circuit current can flow through the quantum wire. Since electrons with higher temperatures have lower chemical potentials, the temperature gradient in the quantum wire drives the cold electrons to the hot side until this thermal imbalance is counteracted by an induced thermovoltage V_{th}, thus defining the thermopower $S = dV_{\mathrm{th}}/dT$. Since the temperature difference fluctuates at frequency 2ω, the thermovoltage V_{th} generated by the Seebeck effect should also have the same frequency of 2ω, which is measured using a lock-in amplifier between terminal 3 and 4. In Figure 45 (c) and (d), $V_{4\mathrm{T}}$ and V_{th} are represented by $V_{1\omega}$ and $V_{2\omega}$ according to reference frequencies.

Generally, the thermopower S is the sum of two terms, the electronic term S_e and the phonon-drag term S_{ph} that is generated by the coupling of electrons with diffused phonons. In linear response, the electronic term S_e is given by the Mott relation [31, 70] as:

$$S_e = \lim_{\Delta T \to 0} \frac{V_{th}}{\Delta T} = -\frac{\pi^2}{3e} k_B^2 T \frac{d}{d\mu} \ln G \tag{10}$$

where $\Delta T = T_e - T_l$ is the temperature difference that generates the thermovoltage V_{th}.

6.3 Results and Discussion

6.3.1 Characterization of the electron waveguide

Quantized conductance steps are observed with the conductance increasing with chemical potential by steps of roughly an integer multiple of the unit conductance $G_0 = e^2/h$. The observed conduction plateaus can be explained by Landauer quantization for which the total conductance G depends on the number of available quantum channels, $G = (e^2/h) \sum_i T_i(\mu)$, where each energy subband available at the chemical potential μ contributes one quantum of the conductance e^2/h with transmission probability $T_i(\mu)$. The subband dispersion of the $\mathrm{LaAlO_3/SrTiO_3}$ quantum wire can be revealed by examining the transconductance $dG/d\mu$ as a function of μ and external magnetic field B, which is shown in Figure 46 (b, d). The transconductance peaks (bright areas) mark the boundaries where new subbands become available, and the subbands are separated by dark areas ($dG/d\mu \to 0$) where the conductance is highly quantized. Some more interesting features of the band structures of the $LaAlO_3/SrTiO_3$ quantum wire are also manifested from the transconductance. For example, several branches are sometimes locked together and then spread apart again, as shown in Figure 46 (b, d). The locking behavior can be accounted for by introducing attractive electron-electron interactions within the waveguide [1]. At some magnetic fields (such as $B = \pm 4$ T for Device A and ± 6 T for Device B), multiple locked subbands contribute to the total conductance together, resulting in a sequence of conductance plateaus which follows a characteristic sequence within Pascal's triangle: $(1, 3, 6, 10 \ldots)\cdot e^2/h$. This demonstrates the existence of the Pascal phase [16] in the electron waveguide formed from bound states of 2, 3, 4, . . . electrons with attractive electronic interactions.

Transport of electrons through the quantum wire is also highly ballistic, which is determined by the relationship between two length scales, the device length scale L and the elastic scattering length L_0. These two length scales can be related to the conductance as $G = G_0 \exp(-L/L_0)$, with the assumption of exponential decay of the conductance with device length. Since the conductance G of our quantum wire has been measured to be very close to G_0 ($G > 0.9G_0$ for both devices) when the first subband is occupied (which corresponds to the location of the first minimum in the transconductance), there should be $L_0 > 10L = 6\mu$m, indicating that the system enters a quantized ballistic regime.

6.3.2 Thermopower measurement

The Mott relation states that the thermovoltage V_{th} should be linearly proportional to the energy derivative of the logarithmic conductance $d(\ln G)/d\mu$. To check whether the Mott relation holds for $LaAlO_3/SrTiO_3$ electron waveguides, we compare the measured V_{th} and $d(\ln G)/d\mu$ at different T and B and in different devices. At $T = 100$ mK, thermopower measurement is taken from Device A at $B = 0.5$ T (Figure 47 (a)) and 3.5 T (Figure 47 (b)); At $B = 6$ T, thermopower measurement is taken from Device B at $T = 100$ mK (Figure 47 (c)) and 400 mK (Figure 47 (c)). The measured V_{th} is found to compare very well

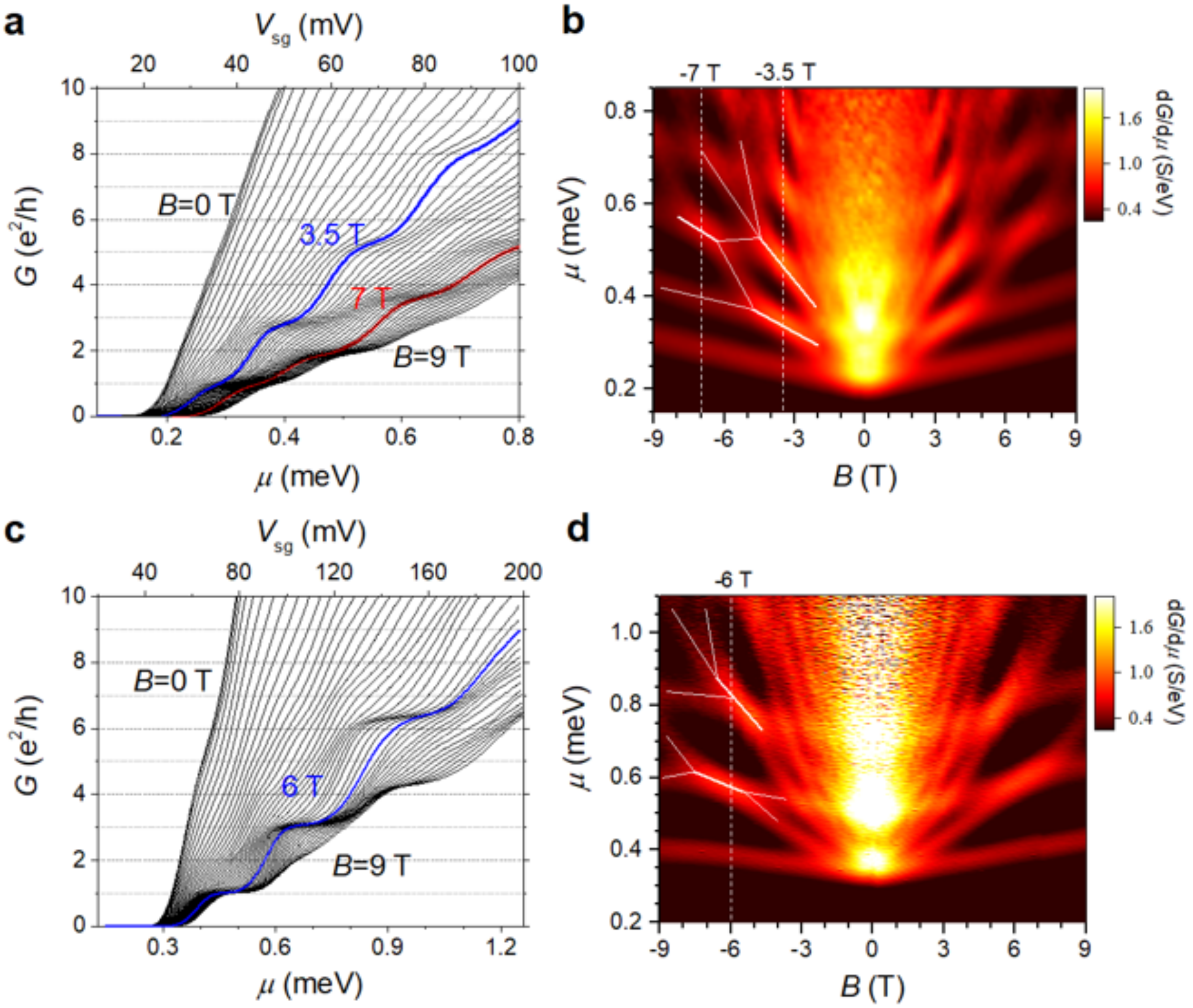

Figure 46: Characterization of quantum wires in thermopower experiments. (a, c) Zero-bias conductance of the quantum nanowires (Devices A and B) as a function of chemical potential μ and magnetic field B in the range $0-9$ T at $T=80$ mK. (b, d) Transconductance map $dG/d\mu$ as a function of chemical potential μ and magnetic field B at $T=80$ mK showing the band structure of electrons in the c-AFM-sketched $LaAlO_3/SrTiO_3$ quantum nanowires.

with $d(\ln G)/d\mu$, irrespective of the device, B or T. As T increases, features attributable to the subband structure governing the electrical conductance G, $dG/d\mu$, and $d(\ln G)/d\mu$ are

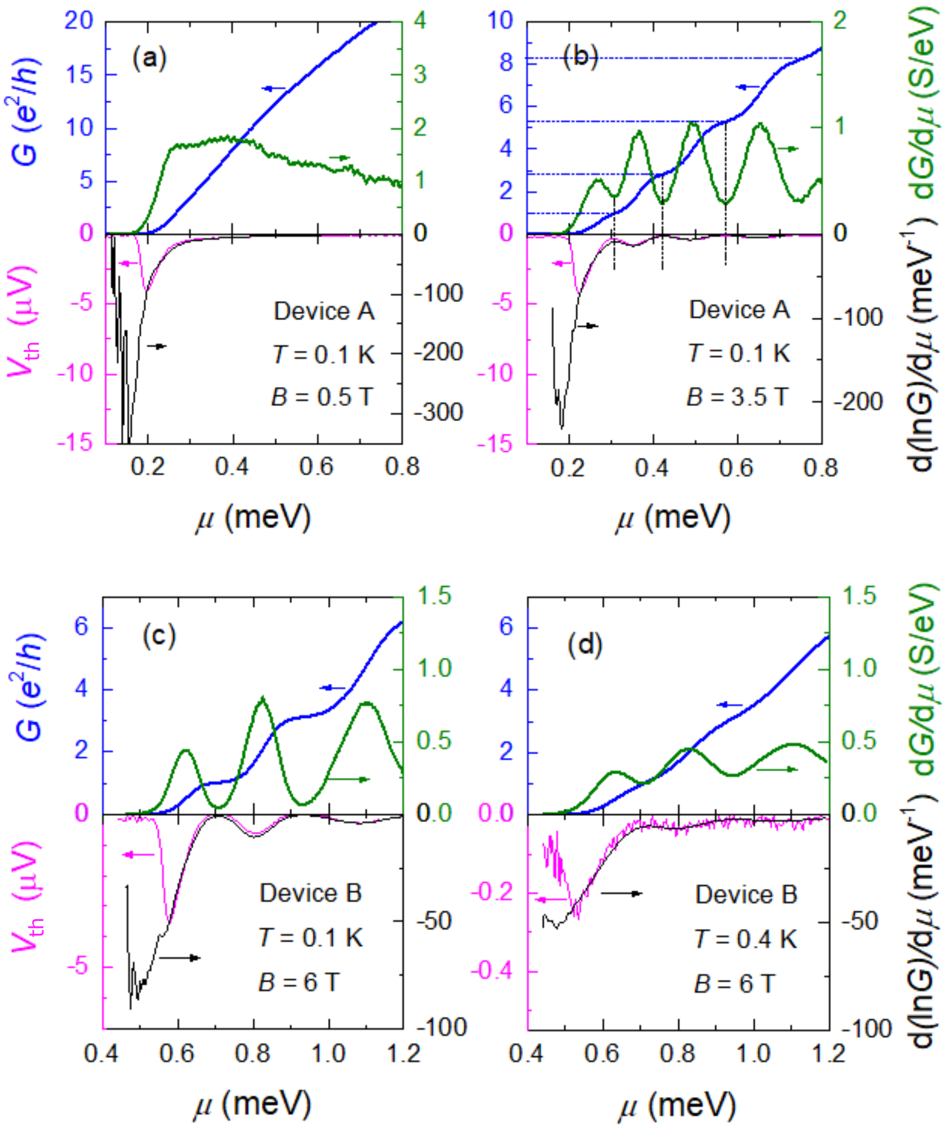

Figure 47: Thermovoltage measurement of Device A. Top panels: Four-terminal conductance G and transconductance $dG/d\mu$ as a function of chemical potential μ. Bottom panels: $V_{\rm th}$ and $d(\ln G)/d\mu$. (a) and (b) are taken from Device A at $T = 100$ mK and $B = 0.5$ and 3.5 T, respectively. (c) and (d) are taken from Device B at $B = 6$ T and $T = 100$ and 400 mK, respectively

thermally broadened. The measured thermovoltage $V_{\rm th}$ also shows muted oscillatory features but still compares well with $d(\ln G)/d\mu$. The thermovoltage as a function of the side gate voltage reaches a local maximum every time the conductance changes from one plateau to the next, and has a dip corresponding to each plateau of the conductance. Similar features have also been observed on quantum point contacts [120, 38, 2], where the thermopower as a function of the gate voltage also shows a peak every time the conductance plateau changes from one subband to the next. The excellent agreement between V_{th} and $d(\ln G)/d\mu$ confirms the validity of the Mott relation (Eq. 10), and furthermore allows us to deduce the (gate-dependent) temperature difference between the two sides of the quantum wire as:

$$T_e - T_l = \sqrt{\frac{T_l^2}{4} + \frac{1}{-\frac{\pi^2}{3e}k_B^2} \frac{V_{th}}{\frac{d}{d\mu}\ln G}} - \frac{T_l}{2} \tag{11}$$

Figure 48 (a) shows the corresponding electron temperatures, calculated using Eq. 11. We notice that the calculated temperature difference $T_e - T_l$ reduces to zero as the quantum wire is tuned to the insulating state, which, however, is not realistic, as the temperature difference should still exist even when the quantum wire is insulating. This apparent disagreement can be explained by a space-charge effect proposed by Mahan [97, 98], who stated that the thermovoltage should instead read as $V_{\text{th}} = -S\Delta T f$, where f is the dielectric screening function and approaches zero as the electron density approaches zero (being insulating). Therefore, the measured thermovoltage being zero does not necessarily require the Seebeck coefficient S or the temperature difference ΔT to vanish. The temperature difference derived in the insulating regime is ignored and we only focus on the conducting regime.

The temperature difference of the quantum wire in the conducting regime exhibits oscillations. The Seebeck coefficient of the quantum wire can be determined from Eq. 10, with the results plotted in Figure 48 (b). The negative sign of S confirms the electrons as energy carriers. The magnitude of the Seebeck coefficient S (the thermopower) increases dramatically as the quantum wire being tuned to the electron-depletion regime, reaching as high as 400 μV/K for Device A at only $T = 0.1$ K. The magnetic fields do not have a significant effect on the thermopower S.

The Mott relation also predicts that the thermopower S should be linearly proportional to the temperature. To test if this is true for our electron waveguide, we measure the thermopower of Device B in a magnetic field of $B = 6$ T at different temperatures ranging from 100 to 400 mK. Results are plotted as a function of the normalized electrical conductance

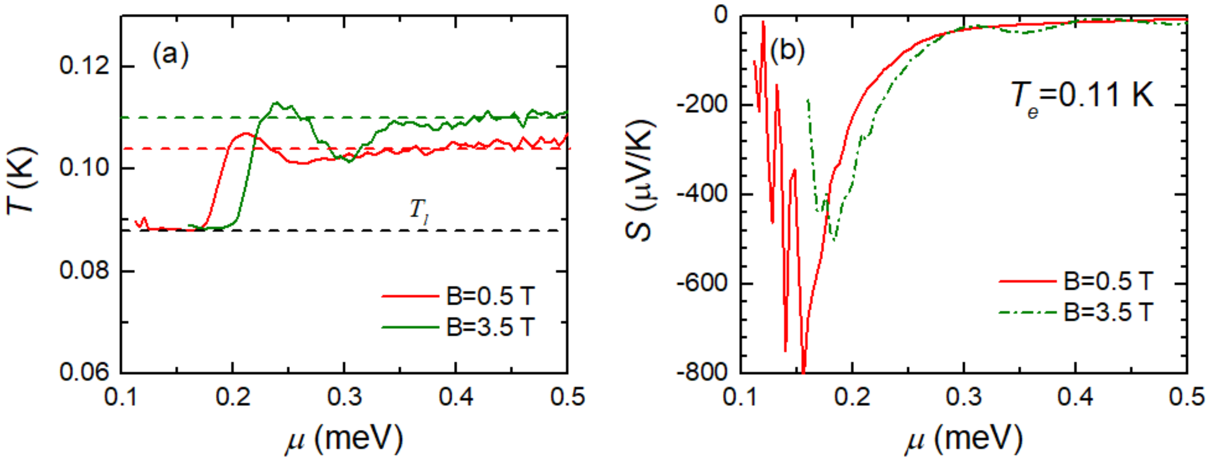

Figure 48: Derived electron temperature and Seebeck coefficient. Electron temperature T_e (a) and Seebeck coefficient (b) S of the quantum wire (Device A) as a function of chemical potential μ at different magnetic fields $B = 0.5$ and 3.5 T.

G/G_0, as shown in Figure 49 (a). We find that overall, the thermopower increases with temperature. At a low temperature of 100 mK, the thermopower has sharp local minimums (dips in the plot) when the conductance reaches plateaus (G/G_0 = 1,3,..). As the temperature increases, these dips are smeared out, analogous to $dG/d\mu$ being smeared out at a higher temperature (Figure 48 (d)). S shown in Figure 49 (a) suggests different temperature dependencies depending on whether G of the electron waveguide is at a conductance plateau. To further explore this point, S at representative G values are plotted as a function of T with both S and T axes in log scale (Figure 49 (c)). It can be observed that S at conductance plateaus G = 1 and 3 e^2/h are parallel to each other with a T^2 dependence while S at conductance values between plateaus is also parallel to each other but with a $T^{0.5}$ dependence. This is also shown in Figure 49 (b), where the exponent m of the thermopower's T dependence is plotted as a function of G/G_0.

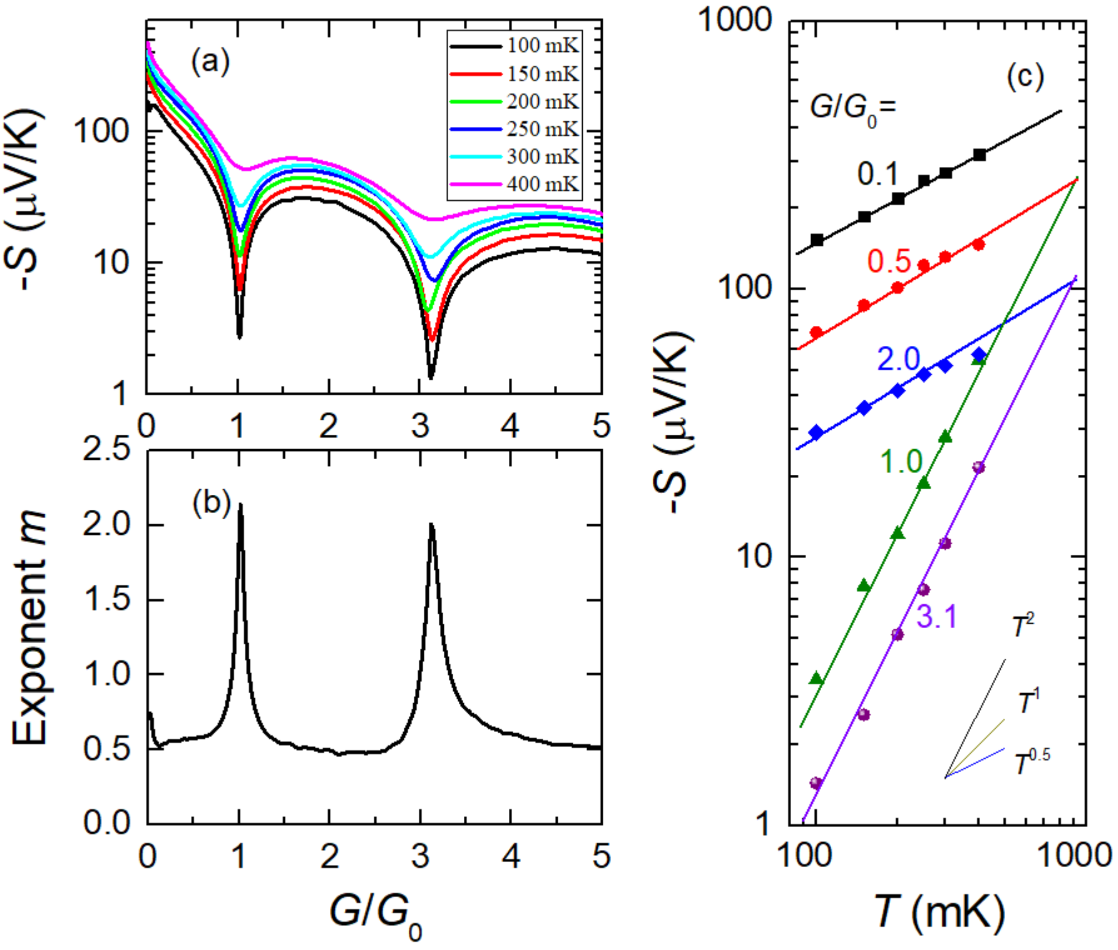

Figure 49: Thermopower as a function of T and G for Device B. (a) The measured thermopower of Device B in a magnetic field of $B = 6$ T at T ranging from 100 to 400 mK as a function of normalized electrical conductance G/G_0. (b) Exponent m of the thermopower's T dependence as a function of G/G_0. (c) Thermopower plotted as a function of T at fixed G values and fittings showing their T dependences.

6.4 Conclusion

In conclusion, we have measured the field-effect electrical transport and thermoelectric properties of quasi-1D electron waveguides at the $LaAlO_3/SrTiO_3$ interface at low temperatures of $100-400$ mK. We find an oscillating thermopower for the electron waveguide as a function of the side gate voltage. The thermopower is well described by the Mott relation and exhibits different T dependencies with the exponent varying from 0.5 to 2 depending on whether the G of the electron waveguide is at a quantized conductance plateau. Our results demonstrate the capability to study electronic structures of nanowires at the $\mathrm{LaAlO_3/SrTiO_3}$ interface with the thermal transport technique. And due to the fascinating electronic phases $\mathrm{LaAlO_3/SrTiO_3}$ nanowires exhibit, it can further lead to the understanding of quantization of thermal conductance and other exotic electronic phases in $\mathrm{LaAlO_3/SrTiO_3}$ systems.

7.0 Conclusions and Outlook

Electronic correlations in $LaAlO_3/SrTiO_3$ heterostructures give rise to a lot of unconventional physical phenomena and make this system rich in physics. The development of c-AFM lithography enables the fabrication of nanodevices at the interface with reduced dimensionalities. Combining the rich physics and device fabrication capability of the interface, transport experiments performed with nanowire-based nanodevices at the interface help to reveal emergent electronic properties and the nature of electron-electron interactions in the system. This makes STO-based complex oxide heterostructures continue to be a promising candidate for next-generation nanoelectronic devices.

Not restricted to one single nanowire, in this dissertation, the frictional drag experiment is performed which involves two closely spaced but electrically isolated nanowires. We explored frictional drag in high magnetic field regime, superconducting regime, and frictional drag which involves an electron waveguide. In the high magnetic field regime and superconducting regime, the frictional drag reveals a non-Coulombic coupling between nanowires. In the superconducting regime, the enhanced frictional drag suggests a reduced dimension in superconducting nanowires because superconductivity is situated at the boundary between the nanowire and insulating regime.

Results from the frictional drag suggest the potentially important role the ferroelastic domain plays in the transport properties at $LaAlO_3/SrTiO_3$ interface. To further understand the ferroelastic domain, one direction is using a low-temperature scanning probe microscope to directly image the evolution of ferroelastic domains in a frictional drag experiment. Another direction is the frictional drag between coupled electron waveguides which allows to further explore 1D electronic properties. Since the coupling is not sensitive to the separation between nanowires, we can try further increasing the separation and scale up the device dimension with ultra-low-voltage electron-beam lithography (ULV-EBL) so that each electron waveguide can be more independently tuned by the local side gate voltage.

Electronic properties at the $LaAlO_3/SrTiO_3$ interface are mostly explored by electrical transport experiments in our group. However, thermal transport experiments can also provide insights into electronic properties. In this dissertation, the Seebeck effect of an electron waveguide is studied which paves the way for the study of electronic properties in electron waveguides with the thermal transport technique. The Seebeck coefficient can be explained by the Mott relation, which indicates the heat is carried by electrons. It would be interesting to measure the thermal conductance of the electron waveguide which can provide quantitative information on charges of emergent Pascal phases.

More broadly speaking, researches on $LaAlO_3/SrTiO_3$ interfaces can greatly benefit from the rich physics at the interface and the capability to fabricate nanodevices at the interface due to c-AFM lithography and newly developed ULV-EBL. A lot of explorations can be done in both 1D and 2D physics. 1D physics can greatly benefit from the electron waveguide. The advancement of the electron waveguide fabrication technique has lead to better control and a deeper understanding of electronic properties in the electron waveguide. By modulating the tip voltage or shape of the electron waveguide, more electron transport properties can be achieved, which has great potential for controlling the spin of electrons and can lead to the realization of spintronics and Majorana physics. Placing $LaAlO_3/SrTiO_3$ with other 2D materials, more novel nanodevices can be produced. These complex heterostructures can give rise to novel physical properties or allow us to study electronic interactions between charge carriers with distinct natures. In terms of the fabrication techniques, ULV-EBL can open new avenues for the exploration of physics at $LaAlO_3/SrTiO_3$ interfaces, which is able to rapidly create complex nanostructures and study electronic properties at a large scale.

Bibliography

[1] Anil Annadi, Guanglei Cheng, Hyungwoo Lee, Jung-Woo Lee, Shicheng Lu, Anthony Tylan-Tyler, Megan Briggeman, Michelle Tomczyk, Mengchen Huang, David Pekker, et al. Quantized ballistic transport of electrons and electron pairs in LaAlO3/SrTiO3 nanowires. *Nano letters*, 18(7):4473–4481, 2018.

[2] NJ Appleyard, JT Nicholls, WR Tribe, MY Simmons, and M Pepper. Thermopower of one-dimensional devices–measurement and applications. *Physica E: Low-dimensional Systems and Nanostructures*, 6(1-4):534–537, 2000.

[3] Ramazan Asmatulu and Waseem S Khan. *Synthesis and applications of electrospun nanofibers*. Elsevier, 2018.

[4] OM Auslaender, H Steinberg, A Yacoby, Y Tserkovnyak, BI Halperin, KW Baldwin, LN Pfeiffer, and KW West. Spin-charge separation and localization in one dimension. *Science*, 308(5718):88–92, 2005.

[5] Nicholas Howard Balshaw. *Practical cryogenics: an introduction to laboratory cryogenics*. Oxford Instruments, Scientific Research Division, 1996.

[6] John Bardeen, Leon N Cooper, and John Robert Schrieffer. Theory of superconductivity. *Physical review*, 108(5):1175, 1957.

[7] C Bell, H Hwang, Z Erlich, Y Frenkel, Y Shperber, B Kalisky, J Drori, H Sato, M Hosoda, Y Xie, et al. Optical Study of Tetragonal Domains in $LaAlO_3/SrTiO_3$. *Journal of Superconductivity & Novel Magnetism*, 28(3), 2015.

[8] Feng Bi, Daniela F Bogorin, Cheng Cen, Chung Wung Bark, Jae-Wan Park, Chang-Beom Eom, and Jeremy Levy. "Water-cycle" mechanism for writing and erasing nanostructures at the LaAlO 3/SrTiO 3 interface. *Applied Physics Letters*, 97(17):173110, 2010.

[9] Feng Bi, Mengchen Huang, Hyungwoo Lee, Chang-Beom Eom, Patrick Irvin, and Jeremy Levy. $LaAlO_3$ thickness window for electronically controlled magnetism at $LaAlO_3/SrTiO_3$ heterointerfaces. *Applied Physics Letters*, 107(8):082402, 2015.

[10] Feng Bi, Mengchen Huang, Sangwoo Ryu, Hyungwoo Lee, Chung-Wung Bark, Chang-Beom Eom, Patrick Irvin, and Jeremy Levy. Room-temperature electronically-controlled ferromagnetism at the $LaAlO_3/SrTiO_3$ interface. *Nature communications*, 5(1):1–7, 2014.

[11] Gerd Binnig, Calvin F Quate, and Ch Gerber. Atomic force microscope. *Physical review letters*, 56(9):930, 1986.

[12] Daniela F Bogorin, Chung Wung Bark, Ho Won Jang, Cheng Cen, Chad M Folkman, Chang-Beom Eom, and Jeremy Levy. Nanoscale rectification at the $LaAlO_3/SrTiO_3$ interface. *Applied Physics Letters*, 97(1):013102, 2010.

[13] II Boiko, P Vasilopoulos, and Yu M Sirenko. Coulomb coupling between two-dimensional and three-dimensional electron-gas layers: Influence on electrical transport. *Physical Review B*, 45(23):13538, 1992.

[14] Megan Briggeman, Hyungwoo Lee, Jung-Woo Lee, Kitae Eom, François Damanet, Elliott Mansfield, Jianan Li, Mengchen Huang, Andrew J Daley, Chang-Beom Eom, et al. One-dimensional Kronig-Penney superlattices at the $LaAlO_3/SrTiO_3$ interface. *arXiv preprint arXiv:1912.07164*, 2019.

[15] Megan Briggeman, Jianan Li, Mengchen Huang, Hyungwoo Lee, Jung-Woo Lee, Kitae Eom, Chang-Beom Eom, Patrick Irvin, and Jeremy Levy. Engineered spin-orbit interactions in $LaAlO_3/SrTiO_3$-based 1D serpentine electron waveguides. *Science Advances*, 6(48):eaba6337, 2020.

[16] Megan Briggeman, Michelle Tomczyk, Binbin Tian, Hyungwoo Lee, Jung-Woo Lee, Yuchi He, Anthony Tylan-Tyler, Mengchen Huang, Chang-Beom Eom, David Pekker, et al. Pascal conductance series in ballistic one-dimensional $LaAlO_3/SrTiO_3$ channels. *Science*, 367(6479):769–772, 2020.

[17] Alexander Brinkman, Mark Huijben, M Van Zalk, J Huijben, U Zeitler, JC Maan, Wilfred Gerard van der Wiel, GJHM Rijnders, David HA Blank, and H Hilgenkamp. Magnetic effects at the interface between non-magnetic oxides. *Nature materials*, 6(7):493, 2007.

[18] Keith A Brown, Shu He, Daniel J Eichelsdoerfer, Mengchen Huang, Ishan Levy, Hyungwoo Lee, Sangwoo Ryu, Patrick Irvin, Jose Mendez-Arroyo, Chang-Beom Eom, Mirkin Chad A., and Levy Jeremy. Giant conductivity switching of LaAlO 3/SrTiO 3 heterointerfaces governed by surface protonation. *Nature communications*, 7:10681, 2016.

[19] A Buckley, Jean-Pierre Rivera, and Ekhard KH Salje. Twin structures in tetragonal SrTiO 3: The ferroelastic phase transition and the formation of needle domains. *Journal of applied physics*, 86(3):1653–1656, 1999.

[20] AD Caviglia, M Gabay, Stefano Gariglio, Nicolas Reyren, Claudia Cancellieri, and J-M Triscone. Tunable Rashba spin-orbit interaction at oxide interfaces. *Physical review letters*, 104(12):126803, 2010.

[21] AD Caviglia, Stefano Gariglio, Nicolas Reyren, Didier Jaccard, T Schneider, M Gabay, S Thiel, G Hammerl, Jochen Mannhart, and J-M Triscone. Electric field control of the LaAlO 3/SrTiO 3 interface ground state. *Nature*, 456(7222):624, 2008.

[22] Cheng Cen, S Thiel, G Hammerl, CW Schneider, KE Andersen, CS Hellberg,

J Mannhart, and J Levy. Nanoscale control of an interfacial metal–insulator transition at room temperature. *Nature materials*, 7(4):298, 2008.

[23] Cheng Cen, Stefan Thiel, Jochen Mannhart, and Jeremy Levy. Oxide nanoelectronics on demand. *Science*, 323(5917):1026–1030, 2009.

[24] Young Jun Chang, Guru Khalsa, Luca Moreschini, Andrew L Walter, Aaron Bostwick, Karsten Horn, AH MacDonald, and Eli Rotenberg. Uniaxial strain induced band splitting in semiconducting $SrTiO_3$. *Physical Review B*, 87(11):115212, 2013.

[25] Lu Chen, Jianan Li, Yuhe Tang, Yun-Yi Pai, Yunzhong Chen, Nini Pryds, Patrick Irvin, and Jeremy Levy. Extreme reconfigurable nanoelectronics at the cazro3/srtio3 interface. *Advanced Materials*, 30(33):1801794, 2018.

[26] Guanglei Cheng, Anil Annadi, Shicheng Lu, Hyungwoo Lee, Jung-Woo Lee, Mengchen Huang, Chang-Beom Eom, Patrick Irvin, and Jeremy Levy. Shubnikov–de Haas–like Quantum Oscillations in Artificial One-Dimensional $LaAlO_3/SrTiO_3$ Electron Channels. *Physical review letters*, 120(7):076801, 2018.

[27] Guanglei Cheng, Pablo F Siles, Feng Bi, Cheng Cen, Daniela F Bogorin, Chung Wung Bark, Chad M Folkman, Jae-Wan Park, Chang-Beom Eom, Gilberto Medeiros-Ribeiro, et al. Sketched oxide single-electron transistor. *Nature Nanotechnology*, 6(6):343, 2011.

[28] Guanglei Cheng, Michelle Tomczyk, Shicheng Lu, Joshua P Veazey, Mengchen Huang, Patrick Irvin, Sangwoo Ryu, Hyungwoo Lee, Chang-Beom Eom, C Stephen Hellberg, and Jeremy Levy. Electron pairing without superconductivity. *Nature*, 521(7551):196, 2015.

[29] Guanglei Cheng, Michelle Tomczyk, Alexandre B Tacla, Hyungwoo Lee, Shicheng Lu, Josh P Veazey, Mengchen Huang, Patrick Irvin, Sangwoo Ryu, Chang-Beom Eom, Andrew Daley, David Pekker, and Jeremy Levy. Tunable electron-electron interactions in $LaAlO_3/SrTiO_3$ nanostructures. *Physical Review X*, 6(4):041042, 2016.

[30] Guanglei Cheng, Joshua P Veazey, Patrick Irvin, Cheng Cen, Daniela F Bogorin, Feng Bi, Mengchen Huang, Shicheng Lu, Chung-Wung Bark, Sangwoo Ryu, et al. Anomalous transport in sketched nanostructures at the $LaAlO_3/SrTiO_3$ interface. *Physical Review X*, 3(1):011021, 2013.

[31] Melvin Cutler and Nevill Francis Mott. Observation of Anderson localization in an electron gas. *Physical Review*, 181(3):1336, 1969.

[32] P Debray, P Vasilopoulos, O Raichev, R Perrin, M Rahman, and WC Mitchel. Experimental observation of Coulomb drag in parallel ballistic quantum wires. *Physica E: Low-dimensional Systems and Nanostructures*, 6(1-4):694–697, 2000.

[33] P Debray, V Zverev, O Raichev, R Klesse, P Vasilopoulos, and RS Newrock. Experi-

mental studies of Coulomb drag between ballistic quantum wires. *Journal of Physics: Condensed Matter*, 13(14):3389, 2001.

[34] Jan Dec, Wolfgang Kleemann, and Mitsuru Itoh. Electric-field-induced ferroelastic single domaining of Sr $\mathrm{Ti}^{1}8\mathrm{O}_3$. *Applied physics letters*, 85(22):5328–5330, 2004.

[35] R Dingle, HL Störmer, AC Gossard, and W Wiegmann. Electron mobilities in modulation-doped semiconductor heterojunction superlattices. *Applied Physics Letters*, 33(7):665–667, 1978.

[36] AP Dmitriev, IV Gornyi, and DG Polyakov. Coulomb drag between ballistic quantum wires. *Physical Review B*, 86(24):245402, 2012.

[37] Ji-Min Duan and Sungkit Yip. Supercurrent drag via the Coulomb interaction. *Physical review letters*, 70(23):3647, 1993.

[38] AS Dzurak, CG Smith, L Martin-Moreno, M Pepper, DA Ritchie, GAC Jones, and DG Hasko. Thermopower of a one-dimensional ballistic constriction in the non-linear regime. *Journal of Physics: Condensed Matter*, 5(43):8055, 1993.

[39] DM Eagles. Possible pairing without superconductivity at low carrier concentrations in bulk and thin-film superconducting semiconductors. *Physical Review*, 186(2):456, 1969.

[40] JP Eisenstein. New transport phenomena in coupled quantum wells. *Superlattices and microstructures*, 12(1):107–114, 1992.

[41] Fedwa El-Mellouhi, Edward N Brothers, Melissa J Lucero, and Gustavo E Scuseria. Modeling of the cubic and antiferrodistortive phases of SrTiO_3 with screened hybrid density functional theory. *Physical Review B*, 84(11):115122, 2011.

[42] Gregory A Fiete, Karyn Le Hur, and Leon Balents. Coulomb drag between two spin-incoherent Luttinger liquids. *Physical Review B*, 73(16):165104, 2006.

[43] Karsten Flensberg. Coulomb drag of Luttinger liquids and quantum Hall edges. *Physical review letters*, 81(1):184, 1998.

[44] Thomas Fuchs, Rochus Klesse, and Ady Stern. Coulomb drag between quantum wires with different electron densities. *Physical Review B*, 71(4):045321, 2005.

[45] N Giordano. Evidence for macroscopic quantum tunneling in one-dimensional superconductors. *Physical review letters*, 61(18):2137, 1988.

[46] N Giordano and JD Monnier. Cross-talk effects in superconductor-insulator-normal-metal trilayers. *Physical Review B*, 50(13):9363, 1994.

[47] Nicholas J Goble, Richard Akrobetu, Hicham Zaid, Sukrit Sucharitakul, Marie-Hélène

Berger, Alp Sehirlioglu, and Xuan PA Gao. Anisotropic electrical resistance in mesoscopic $LaAlO_3/SrTiO_3$ devices with individual domain walls. *Scientific reports*, 7(1):1–9, 2017.

[48] RV Gorbachev, AK Geim, MI Katsnelson, KS Novoselov, T Tudorovskiy, IV Grigorieva, AH MacDonald, SV Morozov, K Watanabe, T Taniguchi, et al. Strong Coulomb drag and broken symmetry in double-layer graphene. *Nature Physics*, 8(12):896–901, 2012.

[49] Lev P Gor'kov. Phonon mechanism in the most dilute superconductor n-type $SrTiO_3$. *Proceedings of the National Academy of Sciences*, 113(17):4646–4651, 2016.

[50] TJ Gramila, JP Eisenstein, AH MacDonald, LN Pfeiffer, and KW West. Mutual friction between parallel two-dimensional electron systems. *Physical review letters*, 66(9):1216, 1991.

[51] TJ Gramila, JP Eisenstein, AH MacDonald, LN Pfeiffer, and KW West. Electron-electron scattering between parallel two-dimensional electron gases. *Surface science*, 263(1-3):446–450, 1992.

[52] TJ Gramila, JP Eisenstein, AH MacDonald, LN Pfeiffer, and KW West. Evidence for virtual-phonon exchange in semiconductor heterostructures. *Physical Review B*, 47(19):12957, 1993.

[53] TJ Gramila, JP Eisenstein, AH MacDonald, LN Pfeiffer, and KW West. Measuring electron—electron scattering rates through mutual friction. *Physica B: Condensed Matter*, 197(1-4):442–448, 1994.

[54] Qing Guo. *Reconfigurable graphene complex oxide nanostructures.* PhD thesis, University of Pittsburgh, 2020.

[55] VL Gurevich, VB Pevzner, and EW Fenton. Coulomb drag in the ballistic electron transport regime. *Journal of Physics: Condensed Matter*, 10(11):2551, 1998.

[56] JH Haeni, P Irvin, W Chang, Reinhard Uecker, P Reiche, YL Li, S Choudhury, W Tian, ME Hawley, B Craigo, et al. Room-temperature ferroelectricity in strained $SrTiO_3$. *Nature*, 430(7001):758–761, 2004.

[57] FDM Haldane. Effective harmonic-fluid approach to low-energy properties of one-dimensional quantum fluids. *Physical Review Letters*, 47(25):1840, 1981.

[58] E Heifets, E Kotomin, and VA Trepakov. Calculations for antiferrodistortive phase of $SrTiO_3$ perovskite: hybrid density functional study. *Journal of Physics: Condensed Matter*, 18(20):4845, 2006.

[59] Joachim Hemberger, Peter Lunkenheimer, R Viana, R Böhmer, and Alois Loidl. Electric-field-dependent dielectric constant and nonlinear susceptibility in $SrTiO_3$.

Physical Review B, 52(18):13159, 1995.

[60] NPR Hill, JT Nicholls, EH Linfield, M Pepper, DA Ritchie, GAC Jones, Ben Yu-Kuang Hu, and Karsten Flensberg. Correlation effects on the coupled plasmon modes of a double quantum well. *Physical review letters*, 78(11):2204, 1997.

[61] Maayan Honig, Joseph A Sulpizio, Jonathan Drori, Arjun Joshua, Eli Zeldov, and Shahal Ilani. Local electrostatic imaging of striped domain order in $LaAlO_3/SrTiO_3$. *Nature materials*, 12(12):1112, 2013.

[62] RA Höpfel and J Shah. Electron-hole drag in semiconductors. *Solid-State Electronics*, 31(3-4):643–648, 1988.

[63] Ralph A Höpfel, Jagdeep Shah, Peter A Wolff, and Arthur C Gossard. Negative absolute mobility of minority electrons in GaAs quantum wells. *Physical review letters*, 56(25):2736, 1986.

[64] Mengchen Huang, Feng Bi, Sangwoo Ryu, Chang-Beom Eom, Patrick Irvin, and Jeremy Levy. Direct imaging of $LaAlO_3/SrTiO_3$ nanostructures using piezoresponse force microscopy. *APL Materials*, 1(5):052110, 2013.

[65] Xiaokang Huang, Greg Bazàn, and Gary H Bernstein. Observation of supercurrent drag between normal metal and superconducting films. *Physical review letters*, 74(20):4051, 1995.

[66] Patrick Irvin, Yanjun Ma, Daniela F Bogorin, Cheng Cen, Chung Wung Bark, Chad M Folkman, Chang-Beom Eom, and Jeremy Levy. Rewritable nanoscale oxide photodetector. *Nature Photonics*, 4(12):849, 2010.

[67] Patrick Irvin, Joshua P Veazey, Guanglei Cheng, Shicheng Lu, Chung-Wung Bark, Sangwoo Ryu, Chang-Beom Eom, and Jeremy Levy. Anomalous high mobility in $LaAlO_3/SrTiO_3$ nanowires. *Nano letters*, 13(2):364–368, 2013.

[68] Antti-Pekka Jauho and Henrik Smith. Coulomb drag between parallel two-dimensional electron systems. *Physical Review B*, 47(8):4420, 1993.

[69] Y Jompol, CJB Ford, JP Griffiths, I Farrer, GAC Jones, D Anderson, DA Ritchie, TW Silk, and AJ Schofield. Probing spin-charge separation in a Tomonaga-Luttinger liquid. *Science*, 325(5940):597–601, 2009.

[70] M Jonson and GD Mahan. Mott's formula for the thermopower and the Wiedemann-Franz law. *Physical Review B*, 21(10):4223, 1980.

[71] Alexey Kalabukhov, Robert Gunnarsson, Johan Börjesson, Eva Olsson, Tord Claeson, and Dag Winkler. Effect of oxygen vacancies in the $SrTiO_3$ substrate on the electrical properties of the $LaAlO_3/SrTiO_3$ interface. *Physical Review B*, 75(12):121404, 2007.

[72] Beena Kalisky, Eric M Spanton, Hilary Noad, John R Kirtley, Katja C Nowack, Christopher Bell, Hiroki K Sato, Masayuki Hosoda, Yanwu Xie, Yasuyuki Hikita, et al. Locally enhanced conductivity due to the tetragonal domain structure in $LaAlO_3/SrTiO_3$ heterointerfaces. *Nature materials*, 12(12):1091, 2013.

[73] Alex Kamenev and Yuval Oreg. Coulomb drag in normal metals and superconductors: Diagrammatic approach. *Physical Review B*, 52(10):7516, 1995.

[74] AJ Keller, Jong-Soo Lim, David Sánchez, Rosa López, S Amasha, JA Katine, Hadas Shtrikman, and D Goldhaber-Gordon. Cotunneling drag effect in Coulomb-coupled quantum dots. *Physical review letters*, 117(6):066602, 2016.

[75] Seyoung Kim, Insun Jo, Junghyo Nah, Z Yao, SK Banerjee, and E Tutuc. Coulomb drag of massless fermions in graphene. *Physical Review B*, 83(16):161401, 2011.

[76] Seyoung Kim and Emanuel Tutuc. Coulomb drag and magnetotransport in graphene double layers. *Solid State Communications*, 152(15):1283–1288, 2012.

[77] Younghyun Kim, Roman M Lutchyn, and Chetan Nayak. Origin and transport signatures of spin-orbit interactions in one-and two-dimensional $SrTiO_3$-based heterostructures. *Physical Review B*, 87(24):245121, 2013.

[78] Rochus Klesse and Ady Stern. Coulomb drag between quantum wires. *Physical Review B*, 62(24):16912, 2000.

[79] CS Koonce, Marvin L Cohen, JF Schooley, WR Hosler, and ER Pfeiffer. Superconducting transition temperatures of semiconducting $SrTiO_3$. *Physical Review*, 163(2):380, 1967.

[80] B Laikhtman and PM Solomon. Mutual drag of two-and three-dimensional electron gases in heterostuctures. *Physical Review B*, 41(14):9921, 1990.

[81] D Laroche, G Gervais, MP Lilly, and JL Reno. Positive and negative Coulomb drag in vertically integrated one-dimensional quantum wires. *Nature nanotechnology*, 6(12):793–797, 2011.

[82] D Laroche, G Gervais, MP Lilly, and JL Reno. 1D-1D Coulomb drag signature of a Luttinger liquid. *Science*, 343(6171):631–634, 2014.

[83] Chun Ning Lau, N Markovic, M Bockrath, A Bezryadin, and M Tinkham. Quantum phase slips in superconducting nanowires. *Physical review letters*, 87(21):217003, 2001.

[84] Kayoung Lee, Jiamin Xue, David C Dillen, Kenji Watanabe, Takashi Taniguchi, and Emanuel Tutuc. Giant frictional drag in double bilayer graphene heterostructures. *Physical review letters*, 117(4):046803, 2016.

[85] Alex Levchenko and Alex Kamenev. Coulomb drag in quantum circuits. *Physical*

review letters, 101(21):216806, 2008.

[86] Akash Levy, Feng Bi, Mengchen Huang, Shicheng Lu, Michelle Tomczyk, Guanglei Cheng, Patrick Irvin, and Jeremy Levy. Writing and low-temperature characterization of oxide nanostructures. *JoVE (Journal of Visualized Experiments)*, (89):e51886, 2014.

[87] JIA Li, T Taniguchi, K Watanabe, J Hone, A Levchenko, and CR Dean. Negative Coulomb drag in double bilayer graphene. *Physical review letters*, 117(4):046802, 2016.

[88] JIA Li, T Taniguchi, K Watanabe, J Hone, A Levchenko, and CR Dean. Negative Coulomb drag in double bilayer graphene. *Physical review letters*, 117(4):046802, 2016.

[89] Jianan Li, Qing Guo, Lu Chen, Shan Hao, Yang Hu, Jen-Feng Hsu, Hyungwoo Lee, Jung-Woo Lee, Chang-Beom Eom, Brian D'Urso, et al. Reconfigurable edge-state engineering in graphene using $\mathrm{LaAlO_3/SrTiO_3}$ nanostructures. *Applied Physics Letters*, 114(12):123103, 2019.

[90] Xiao Lin, Zengwei Zhu, Benoît Fauqué, and Kamran Behnia. Fermi surface of the most dilute superconductor. *Physical Review X*, 3(2):021002, 2013.

[91] Xiaomeng Liu, Zeyu Hao, Kenji Watanabe, Takashi Taniguchi, Bertrand I Halperin, and Philip Kim. Interlayer fractional quantum Hall effect in a coupled graphene double layer. *Nature Physics*, 15(9):893–897, 2019.

[92] Xiaomeng Liu, Lei Wang, Kin Chung Fong, Yuanda Gao, Patrick Maher, Kenji Watanabe, Takashi Taniguchi, James Hone, Cory Dean, and Philip Kim. Frictional Magneto-Coulomb Drag in Graphene Double-Layer Heterostructures. *Physical Review Letters*, 119(5):056802, 2017.

[93] Xiaomeng Liu, Kenji Watanabe, Takashi Taniguchi, Bertrand I Halperin, and Philip Kim. Quantum Hall drag of exciton condensate in graphene. *Nature Physics*, 13(8):746–750, 2017.

[94] Gerald Lucovsky. Long Range Cooperative and Local Jahn-Teller Effects in Nanocrystalline Transition Metal Thin Films. In *The Jahn-Teller Effect*, pages 767–808. Springer, 2009.

[95] JM Luttinger. An exactly soluble model of a many-fermion system. *Journal of mathematical physics*, 4(9):1154–1162, 1963.

[96] HJ Harsan Ma, S Scharinger, SW Zeng, D Kohlberger, M Lange, A Stöhr, X Renshaw Wang, T Venkatesan, R Kleiner, JF Scott, et al. Local Electrical Imaging of Tetragonal Domains and Field-Induced Ferroelectric Twin Walls in Conducting $\mathrm{SrTiO_3}$. *Physical review letters*, 116(25):257601, 2016.

[97] GD Mahan. The low-temperature seebeck coefficient in insulators. *Journal of Electronic Materials*, 44(1):431–434, 2015.

[98] GD Mahan. The seebeck coefficient of insulators: electrochemical potential. *Journal of Electronic Materials*, 45(3):1257–1259, 2016.

[99] M Marques, LK Teles, V Anjos, LMR Scolfaro, JR Leite, VN Freire, GA Farias, and EF da Silva Jr. Full-relativistic calculations of the $SrTiO_3$ carrier effective masses and complex dielectric function. *Applied physics letters*, 82(18):3074–3076, 2003.

[100] K Alex Müller and H Burkard. SrTi O 3: An intrinsic quantum paraelectric below 4 K. *Physical Review B*, 19(7):3593, 1979.

[101] Naoyuki Nakagawa, Harold Y Hwang, and David A Muller. Why some interfaces cannot be sharp. *Nature materials*, 5(3):204–209, 2006.

[102] BN Narozhny and IL Aleiner. Mesoscopic fluctuations of the coulomb drag. *Physical review letters*, 84(23):5383, 2000.

[103] BN Narozhny, IL Aleiner, and Ady Stern. Mesoscopic Fluctuations of the Coulomb Drag at ν= 1/2. *Physical Review Letters*, 86(16):3610, 2001.

[104] BN Narozhny and A Levchenko. Coulomb drag. *Reviews of Modern Physics*, 88(2):025003, 2016.

[105] Yuli V Nazarov and DV Averin. Current drag in capacitively coupled Luttinger constrictions. *Physical review letters*, 81(3):653, 1998.

[106] Aditi Nethwewala, Hyungwoo Lee, Megan Briggeman, Yuhe Tang, Jianan Li, Jungwoo Lee, Chang-Beom Eom, Patrick Richard Irvin, and Jeremy Levy. Inhomogeneous energy landscape in LaAlO3/SrTiO3 nanostructures. *Nanoscale Horizons*, 4:1194–1201, 2019.

[107] Thach DN Ngo, Jung-Won Chang, Kyujoon Lee, Seungju Han, Joon Sung Lee, Young Heon Kim, Myung-Hwa Jung, Yong-Joo Doh, Mahn-Soo Choi, Jonghyun Song, et al. Polarity-tunable magnetic tunnel junctions based on ferromagnetism at oxide heterointerfaces. *Nature communications*, 6(1):1–6, 2015.

[108] Hilary Noad, Eric M Spanton, Katja C Nowack, Hisashi Inoue, Minu Kim, Tyler A Merz, Christopher Bell, Yasuyuki Hikita, Ruqing Xu, Wenjun Liu, et al. Variation in superconducting transition temperature due to tetragonal domains in two-dimensionally doped SrTiO 3. *Physical Review B*, 94(17):174516, 2016.

[109] H Noh, S Zelakiewicz, XG Feng, TJ Gramila, LN Pfeiffer, and KW West. Many-body correlations probed by plasmon-enhanced drag measurements in double-quantum-well structures. *Physical Review B*, 58(19):12621, 1998.

[110] H Noh, S Zelakiewicz, TJ Gramila, LN Pfeiffer, and KW West. Phonon-mediated drag in double-layer two-dimensional electron systems. *Physical Review B*, 59(20):13114, 1999.

[111] A Ohtomo and HY Hwang. A high-mobility electron gas at the LaAlO 3/SrTiO 3 heterointerface. *Nature*, 427(6973):423, 2004.

[112] Yun-Yi Pai, Hyungwoo Lee, Jung-Woo Lee, Anil Annadi, Guanglei Cheng, Shicheng Lu, Michelle Tomczyk, Mengchen Huang, Chang-Beom Eom, Patrick Irvin, et al. One-Dimensional Nature of Superconductivity at the $LaAlO_3/SrTiO_3$ Interface. *Physical review letters*, 120(14):147001, 2018.

[113] Yun-Yi Pai, Anthony Tylan-Tyler, Patrick Irvin, and Jeremy Levy. $LaAlO_3/SrTiO_3$: a tale of two magnetisms. *arXiv preprint arXiv:1610.00789*, 2016.

[114] Pier Paolo Aurino, Alexey Kalabukhov, Nikolina Tuzla, Eva Olsson, Tord Claeson, and Dag Winkler. Nano-patterning of the electron gas at the $LaAlO_3/SrTiO_3$ interface using low-energy ion beam irradiation. *Applied Physics Letters*, 102(20):201610, 2013.

[115] JW Park, DF Bogorin, C Cen, DA Felker, Y Zhang, CT Nelson, CW Bark, CM Folkman, XQ Pan, MS Rzchowski, et al. Creation of a two-dimensional electron gas at an oxide interface on silicon. *Nature communications*, 1(1):1–7, 2010.

[116] MB Pogrebinskii. Mutual drag of carriers in a semiconductor-insulator-semiconductor system. *Soviet Physics-Semiconductors*, 11(4):372–376, 1977.

[117] LA Ponomarenko, AK Geim, AA Zhukov, R Jalil, SV Morozov, KS Novoselov, IV Grigorieva, EH Hill, VV Cheianov, VI Fal'Ko, et al. Tunable metal–insulator transition in double-layer graphene heterostructures. *Nature Physics*, 7(12):958–961, 2011.

[118] VV Ponomarenko and DV Averin. Coulomb drag between one-dimensional conductors. *Physical Review Letters*, 85(23):4928, 2000.

[119] AS Price, AK Savchenko, BN Narozhny, G Allison, and DA Ritchie. Giant fluctuations of Coulomb drag in a bilayer system. *Science*, 316(5821):99–102, 2007.

[120] CR Proetto. Thermopower oscillations of a quantum-point contact. *Physical review B*, 44(16):9096, 1991.

[121] M Pustilnik, EG Mishchenko, LI Glazman, and AV Andreev. Coulomb drag by small momentum transfer between quantum wires. *Physical review letters*, 91(12):126805, 2003.

[122] Oleg Raichev and Panagiotis Vasilopoulos. Coulomb drag between parallel ballistic quantum wires. *Physical Review B*, 61(11):7511, 2000.

[123] D Rakhmilevitch, M Ben Shalom, M Eshkol, A Tsukernik, A Palevski, and Y Dagan. Phase coherent transport in $SrTiO_3/LaAlO_3$ interfaces. *Physical Review B*, 82(23):235119, 2010.

[124] Nicolas Reyren, S Thiel, AD Caviglia, L Fitting Kourkoutis, German Hammerl, Christoph Richter, CW Schneider, Thilo Kopp, A-S Rüetschi, Didier Jaccard, Marc Gabay, David A Muller, J-M Triscone, and Jochen Mannhart. Superconducting interfaces between insulating oxides. *Science*, 317(5842):1196–1199, 2007.

[125] C Richter, H Boschker, W Dietsche, E Fillis-Tsirakis, R Jany, F Loder, LF Kourkoutis, DA Muller, JR Kirtley, CW Schneider, et al. Interface superconductor with gap behaviour like a high-temperature superconductor. *Nature*, 502(7472):528, 2013.

[126] Guus JHM Rijnders, Gertjan Koster, Dave HA Blank, and Horst Rogalla. In situ monitoring during pulsed laser deposition of complex oxides using reflection high energy electron diffraction under high oxygen pressure. *Applied physics letters*, 70(14):1888–1890, 1997.

[127] H Rubel, EH Linfield, DA Ritchie, KM Brown, M Pepper, and GAC Jones. Study of the carrier density dependence of the frictional drag between closely spaced two-dimensional electron gases. *Semiconductor science and technology*, 10(9):1229, 1995.

[128] D Rytz, UT Höchli, and H Bilz. Dielectric susceptibility in quantum ferroelectrics. *Physical Review B*, 22(1):359, 1980.

[129] T Sakudo and H Unoki. Dielectric Properties of SrTi O 3 at Low Temperatures. *Physical review letters*, 26(14):851, 1971.

[130] M Salluzzo, JC Cezar, NB Brookes, V Bisogni, GM De Luca, Christoph Richter, Stefan Thiel, Jochen Mannhart, M Huijben, A Brinkman, et al. Orbital reconstruction and the two-dimensional electron gas at the $LaAlO_3/SrTiO_3$ interface. *Physical review letters*, 102(16):166804, 2009.

[131] M Salluzzo, Stefano Gariglio, Daniela Stornaiuolo, V Sessi, S Rusponi, C Piamonteze, GM De Luca, M Minola, D Marré, A Gadaleta, et al. Origin of interface magnetism in $BiMnO_3/SrTiO_3$ and $LaAlO_3/SrTiO_3$ heterostructures. *Physical review letters*, 111(8):087204, 2013.

[132] Christof W Schneider, Stefan Thiel, German Hammerl, Christoph Richter, and Jochen Mannhart. Microlithography of electron gases formed at interfaces in oxide heterostructures. *Applied physics letters*, 89(12):122101, 2006.

[133] JF Schooley, WR Hosler, and Marvin L Cohen. Superconductivity in Semiconducting $SrTiO_3$. *Physical Review Letters*, 12(17):474, 1964.

[134] JF Scott, EKH Salje, and MA Carpenter. Domain wall damping and elastic softening in $SrTiO_3$: Evidence for polar twin walls. *Physical Review Letters*, 109(18):187601, 2012.

[135] M Ben Shalom, M Sachs, D Rakhmilevitch, A Palevski, and Y Dagan. Tuning spin-orbit coupling and superconductivity at the $SrTiO_3/LaAlO_3$ interface: a magneto-

transport study. *Physical review letters*, 104(12):126802, 2010.

[136] Efrat Shimshoni. Role of vortices in the mutual coupling of superconducting and normal-metal films. *Physical Review B*, 51(14):9415, 1995.

[137] Koun Shirai and Kazunori Yamanaka. Mechanism behind the high thermoelectric power factor of $SrTiO_3$ by calculating the transport coefficients. *Journal of Applied Physics*, 113(5):053705, 2013.

[138] U Sivan, PM Solomon, and H Shtrikman. Coupled electron-hole transport. *Physical review letters*, 68(8):1196, 1992.

[139] PM Solomon and B Laikhtman. Mutual drag of 2D and 3D electron gases in heterostructures. *Superlattices and Microstructures*, 10(1):89–94, 1991.

[140] PM Solomon, PJ Price, DJ Frank, and DC La Tulipe. New phenomena in coupled transport between 2D and 3D electron-gas layers. *Physical review letters*, 63(22):2508, 1989.

[141] Justin CW Song, Dmitry A Abanin, and Leonid S Levitov. Coulomb drag mechanisms in graphene. *Nano letters*, 13(8):3631–3637, 2013.

[142] Justin CW Song and Leonid S Levitov. Energy-driven drag at charge neutrality in graphene. *Physical review letters*, 109(23):236602, 2012.

[143] Justin CW Song and Leonid S Levitov. Hall drag and magnetodrag in graphene. *Physical Review Letters*, 111(12):126601, 2013.

[144] Sam W Stanwyck, P Gallagher, JR Williams, and David Goldhaber-Gordon. Universal conductance fluctuations in electrolyte-gated $SrTiO_3$ nanostructures. *Applied Physics Letters*, 103(21):213504, 2013.

[145] Daniela Stornaiuolo, Stefano Gariglio, NJG Couto, Alexandre Fête, AD Caviglia, Gabriel Seyfarth, Didier Jaccard, AF Morpurgo, and J-M Triscone. In-plane electronic confinement in superconducting $LaAlO_3/SrTiO_3$ nanostructures. *Applied Physics Letters*, 101(22):222601, 2012.

[146] Joseph A Sulpizio, Shahal Ilani, Patrick Irvin, and Jeremy Levy. Nanoscale phenomena in oxide heterostructures. *Annual Review of Materials Research*, 44:117–149, 2014.

[147] Yuhe Tang, Jung-Woo Lee, Anthony Tylan-Tyler, Hyungwoo Lee, Michelle Tomczyk, Mengchen Huang, Chang-Beom Eom, Patrick Irvin, and Jeremy Levy. Frictional drag between superconducting $LaAlO_3/SrTiO_3$ nanowires. *Semiconductor Science and Technology*, 35(9):09LT01, 2020.

[148] Yuhe Tang, Anthony Tylan-Tyler, Hyungwoo Lee, Jung-Woo Lee, Michelle Tomczyk,

Mengchen Huang, Chang-Beom Eom, Patrick Irvin, and Jeremy Levy. Long-Range Non-Coulombic Electron-Electron Interactions between $LaAlO_3/SrTiO_3$ Nanowires. *Advanced Materials Interfaces*, page 1900301, 2019.

[149] Stefan Thiel, German Hammerl, A Schmehl, CW Schneider, and Jochen Mannhart. Tunable quasi-two-dimensional electron gases in oxide heterostructures. *Science*, 313(5795):1942–1945, 2006.

[150] M Tinkham, JU Free, CN Lau, and N Markovic. Hysteretic I-V curves of superconducting nanowires. *Physical Review B*, 68(13):134515, 2003.

[151] M Titov, RV Gorbachev, BN Narozhny, T Tudorovskiy, M Schütt, PM Ostrovsky, IV Gornyi, AD Mirlin, MI Katsnelson, KS Novoselov, et al. Giant magnetodrag in graphene at charge neutrality. *Physical review letters*, 111(16):166601, 2013.

[152] Sin-itiro Tomonaga. Remarks on Bloch's method of sound waves applied to many-fermion problems. *Progress of Theoretical Physics*, 5(4):544–569, 1950.

[153] HC Tso, P Vasilopoulos, and FM Peeters. Direct Coulomb and phonon-mediated coupling between spatially separated electron gases. *Physical review letters*, 68(16):2516, 1992.

[154] HC Tso, P Vasilopoulos, and PM Peeters. Coupled electron-hole transport: generalized random-phase approximation and density functional theory. *Surface science*, 305(1-3):400–404, 1994.

[155] Hiromoto Uwe and Tunetaro Sakudo. Stress-induced ferroelectricity and soft phonon modes in SrTi O_3. *Physical Review B*, 13(1):271, 1976.

[156] K Van Benthem, C Elsässer, and RH French. Bulk electronic structure of $SrTiO_3$: Experiment and theory. *Journal of applied physics*, 90(12):6156–6164, 2001.

[157] Joshua P Veazey, Guanglei Cheng, Patrick Irvin, Cheng Cen, Daniela F Bogorin, Feng Bi, Mengchen Huang, Chung-Wung Bark, Sangwoo Ryu, Kwang-Hwan Cho, et al. Oxide-based platform for reconfigurable superconducting nanoelectronics. *Nanotechnology*, 24(37):375201, 2013.

[158] JP Veazey, G Cheng, S Lu, M Tomczyk, F Bi, M Huang, S Ryu, CW Bark, KH Cho, CB Eom, et al. Nonlocal current-voltage characteristics of gated superconducting sketched oxide nanostructures. *EPL (Europhysics Letters)*, 103(5):57001, 2013.

[159] V Vonk, Mark Huijben, KJI Driessen, P Tinnemans, Alexander Brinkman, Sybolt Harkema, and H Graafsma. Interface structure of $SrTiO_3/LaAlO_3$ at elevated temperatures studied in situ by synchrotron x rays. *Physical Review B*, 75(23):235417, 2007.

[160] PR Willmott and JR Huber. Pulsed laser vaporization and deposition. *Reviews of*

Modern Physics, 72(1):315, 2000.

[161] PR Willmott, SA Pauli, R Herger, CM Schlepütz, D Martoccia, BD Patterson, B Delley, R Clarke, D Kumah, C Cionca, et al. Structural basis for the conducting interface between $LaAlO_3$ and $SrTiO_3$. *Physical Review Letters*, 99(15):155502, 2007.

[162] M Yamamoto, M Stopa, Y Tokura, Y Hirayama, and S Tarucha. Negative Coulomb drag in a one-dimensional wire. *Science*, 313(5784):204–207, 2006.

[163] Dengyu Yang, Shan Hao, Jun Chen, Qing Guo, Muqing Yu, Yang Hu, Kitae Eom, Jung-Woo Lee, Chang-Beom Eom, Patrick Irvin, et al. Nanoscale control of $LaAlO_3/SrTiO_3$ metal–insulator transition using ultra-low-voltage electron-beam lithography. *Applied Physics Letters*, 117(25):253103, 2020.

[164] P Zubko, G Catalan, A Buckley, PRL Welche, and JF Scott. Strain-gradient-induced polarization in $SrTiO_3$ single crystals. *Physical Review Letters*, 99(16):167601, 2007.